Trabajo Fin de Máster
"Máster Universitario en Microelectrónica: Diseño y Aplicaciones de Sistemas Micro/Nanométricos"

Characterization set-up and conditioning circuits for nanogenerators based on kinetic energy harvesters

Author: Jaime del Moral Jalón

Thesis directors: Francisco Javier Aparicio Rebollo,

Ali Ghaffarinejad,

Antonio José Gines Artenga

6th September, 2021

SHORT INTRODUCTION AND STRUCTURE OF THE MASTER THESIS

The development of the Internet of Things (IoT) technology is supporting an increasing demand for wireless but interconnected systems. The main bottleneck for the development of wireless, portable and standalone devices is related to the energy supply unit and the different issues associated with batteries (ecologic impact, lifetime…). Therefore, there is a growing interest and demand for the development of energy transducers or scavengers in the form of nanogenerators. Such energy scavengers are conceived to harvest environmental energy (mechanical stimulus and deformations, heat fluctuations, and others) which is used to power up small and portable devices.

The optimal implementation of nanogenerator devices into functional systems requires an intermediate conditioning circuit devoted to adapt to the system output signal and impedance. Such conditioning circuits play a critical role as they are required for the suitable feed of the power management unit and impedance matching. Therefore, the is a growing interest in this topic within the nanogenerators field.

The Nanotechnology on Surfaces and Plasma (ICMS CSIC-US), where this work has been developed, has recently contributed to the field with the development of new nanostructured materials for nanogenerator devices [1]. The group is now addressing the fabrication of advanced devices. Thus, additional efforts are being made to improve the characterization capabilities and the knowledge on the conditioning circuits required for the suitable integration with the devices currently in development. In this context, the aim of this work is the development of **experimental and simulations tools and capabilities for the characterization and optimization of kinetic energy harvesters**, being specially focused on Triboelectric nanogenerators (TENGs). This involves both the fabrication of a **new characterization platform** and the implementation of **conditioning circuits to optimize the energy harvesting process**.

In this context, the **activities that I have developed during this Master Thesis** project include:

- The development and validation of a characterization platform and an experimental procedure for the characterization of TENG systems.
- Fabrication of standard Mode I TENG devices.
- The implementation and experimental analysis of different conditioning circuits.
- Identification and analysis of the main figures of merits.
- The development of the simulation tools to model the response of TENG devices and conditioning circuits.

- Validation of experimental and simulation results.

According to these objectives and the developed work. The present **Master Thesis** has the following **structure:**

- Chapter 1 presents the objectives of this work.
- Chapter 2 describes the followed work plan and the used methodology.
- Chapter 3 makes an introduction to energy harvesters and develops the theoretical foundation of TENGs operation. It also introduces the concept of conditioning circuits for energy harvesting and describes the systems more commonly used in the literature. Finally, the chapter states the equations that describe the operation of the conditioning circuits used in the present Master Thesis [2], [3].
- Chapter 4 deals with the development of the characterization platform. This same chapter assesses the performance of the characterization set-up after several optimization processes [4],[5].
- Chapter 5 addresses the implementation and characterization of two different types of conditioning circuits to interface TENG systems [6], [7].
- Chapter 6 shows the model used to simulate single TENGs. The chapter extends this development to the simulation of the conditioning circuits used in the previous chapter. Finally, this chapter critically analyses and compares experimental and simulation results. [8].
- Chapter 7 presents the conclusions of the work.

Key References:

[1]   A. N. Filippin *et al.*, "Nano Energy 3D core-multishell piezoelectric nanogenerators," *Nano Energy*, vol. 58, no. January, pp. 476–483, 2019, doi: 10.1016/j.nanoen.2019.01.047.

[2]   A. Ghaffarinejad and J. Y. Hasani, "Modeling of triboelectric charge accumulation dynamics at the metal – insulator interface for variable capacitive structures : application to triboelectric nanogenerators," *Appl. Phys. A*, vol. 0, no. 0, p. 0, 2019, doi: 10.1007/s00339-019-2495-y.

[3]   C. Fang *et al.*, "Overview of Power Management for Triboelectric Nanogenerators," *Adv. Intell. Syst.*, vol. 2, no. 2, p. 1900129, 2020, doi: 10.1002/aisy.201900129.

[4] S. Lu *et al.*, "Regulating the high-voltage and high-impedance characteristics of triboelectric nanogenerator toward practical self-powered sensors," *Nano Energy*, vol. 87, no. May, p. 106137, 2021, doi: 10.1016/j.nanoen.2021.106137.

[5] Z. Wang *et al.*, "Two voltages in contact-separation triboelectric nanogenerator: From asymmetry to symmetry for maximum output," *Nano Energy*, vol. 69, no. January, p. 104452, Mar. 2020, doi: 10.1016/j.nanoen.2020.104452.

[6] A. Ghaffarinejad, J. Yavand, D. Galayko, and P. Basset, "Nano Energy Superior performance of half-wave to full-wave rectifier as a power conditioning circuit for triboelectric nanogenerators : Application to contact-separation and sliding mode TENG," *Nano Energy*, vol. 66, no. September, p. 104137, 2019, doi: 10.1016/j.nanoen.2019.104137.

[7] H. Zhang, D. Galayko, and P. Basset, "A self-sustained energy storage system with an electrostatic automatic switch and a buck converter for triboelectric nanogenerators," *J. Phys. Conf. Ser.*, vol. 1407, no. 1, pp. 8–12, 2019, doi: 10.1088/1742-6596/1407/1/012016.

[8] A. Gha *et al.*, "Nano Energy Full paper A conditioning circuit with exponential enhancement of output energy for triboelectric nanogenerator," vol. 51, no. May, pp. 173–184, 2018, doi: 10.1016/j.nanoen.2018.06.034.

1. OBJECTIVES

The present Master Thesis aims at the development of a characterization platform for the analysis of Triboelectric Nanogenerators (TENGs) It also addresses the simulation and experimental analysis of different conditioning circuits devised to optimize the energy harvesting process. These developments are adapted to Mode I TENG architectures such as those currently in development o in the Nanotechnology on Surfaces and Plasma group. Thus, the main objectives of this work are the following.

1. Design and assembly of a characterization platform. This platform is prepared to meet the requirements to excite and measure the electric response of Mode I TENG devices.

2. Verification of the developed platform and characterization methodology. The developed platform is tested by using (contact separation mode) TENG devices. These experiments are used to validate the suitability of the developed set-up.

3. Development and verification of conditioning circuits. Different approaches for conditioning circuits are studied and experimentally implemented. Circuit analyses are also performed on them, and the main figures of merit are analyzed.

4. Development of the simulations tools to model the response of TENG devices and conditioning circuits. In addition, simulation tools are used to develop the analysis of such circuits and TENG properties.

2. METHODOLOGY AND WORK PLAN

The present chapter shows the methodology followed during the master thesis project. This is illustrated in Figure 2.1 which shows the different phases of the project.
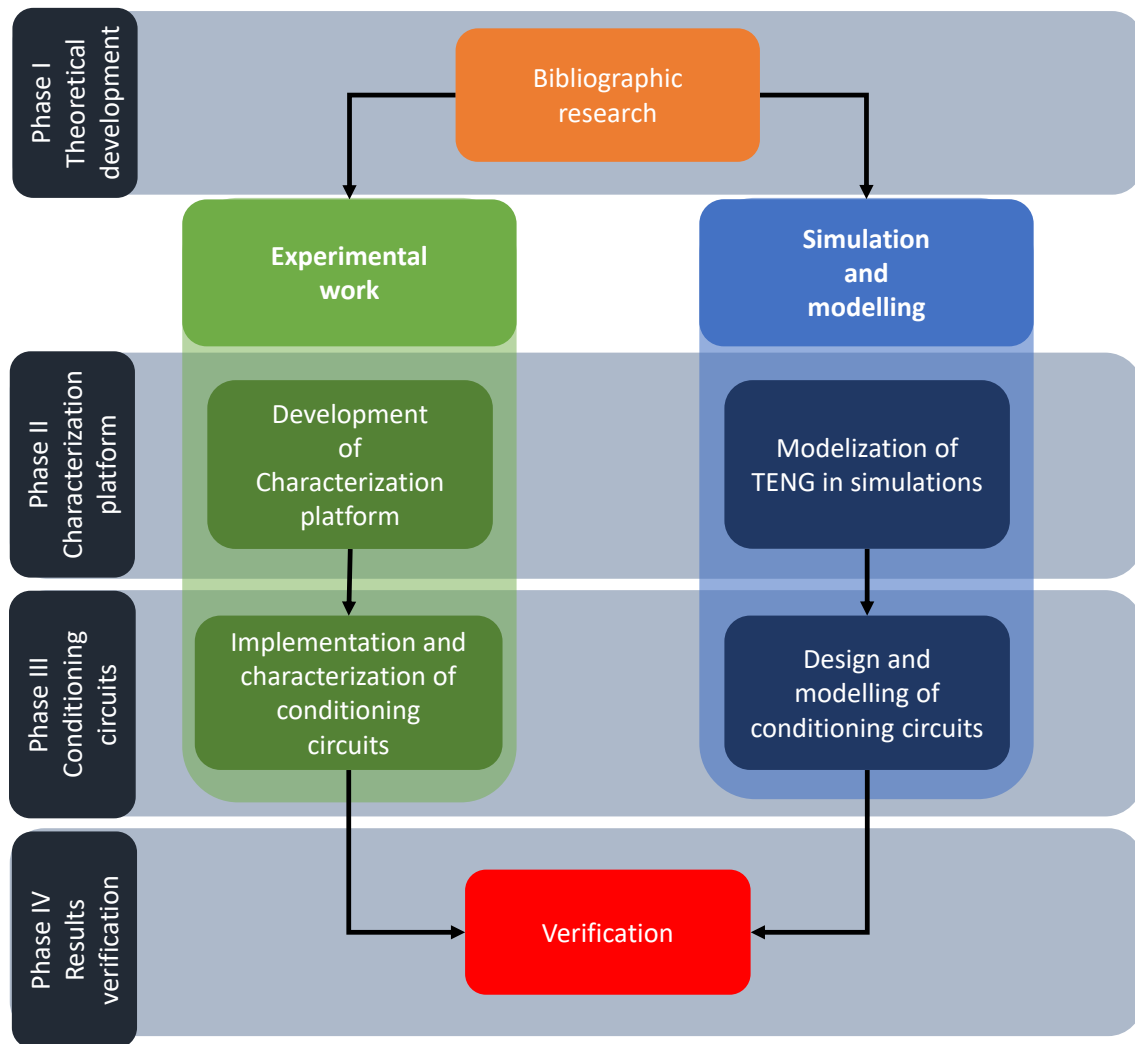
Figure 2.1 Work plan followed in this master thesis.

- **Phase I.** This initial phase is devoted to acquire the necessary knowledge about the topic. Thus, bibliographic research has been conducted about the state of the art of TENG nanogenerators and TENG conditioning circuits.
- **Phase II.** This phase settles the two main parallel paths that this work follows. The experimental branch (green in the figure) deals with the development and verification of the characterization platform for TENG devices. The simulation branch (blue branch in

the figure), addresses the development of the simulation tools to model the TENGs and conditioning circuits.

- ***Phase III.*** The next stage in the experimental path is the implementation and characterization of different conditioning circuits devised to optimize the energy harvesting process in TENG devices. In parallel, these systems (TENG + conditioning circuit) were simulated thanks to the capabilities acquired in the previous phase.

- ***Phase IV.*** This is the last phase where both paths converge, the verification stage. Experimental and simulation are compared with each other and with the literature.

As indicated in the figure the present Master Thesis project involves both experimental and simulation studies. Both approaches have been simultaneously developed during the project (green path and blue path in Figure 2.1). Nevertheless, for sake of simplicity, in the present document, **experimental and simulation results are presented in different chapters**. This decision has been made for sake of clarity, in order to avoid the confusion between experimental and simulation results. This decision is also supported by the fact that also included the development of the characterization and validation of the characterization platform. The final simulation chapter also addresses the comparison with experimental results

3. TRIBOELECTRIC NANOGENERATORS: FUNDAMENTALS AND THEORETICAL BACKGROUND

3.1 Energy Consideration in wireless devices and IoT applications.

Recent technical innovation has led to the information era where devices have presented an exponential growth in number and variety. The development of microelectronics science in the last decade has led to the so-called Internet of Things (IoT). The minimization of size and power requirements in electronics devices allows the use of them in a wide range of applications. Nowadays, it is highly common that a single user has several small and interconnected wireless devices leading to IoT. This tendency is far to reach its complete potential. However, this new generation of devices finds new problems in terms of power supply, [9] since most of them work in a permanent stand-by state. However, batteries are the current solution for these applications, but they have different issues related to the high ecological impact and production cost.

In this scenario, one possible solution for the power supply issue is based on the so denominated nanogenerators, also called energy harvesters or scavengers. These systems are devised to transform environmental energy, in the form of temperature gradients and fluctuations [10], mechanical stimulus [11], and others, into usable electric energy. There are multiple environmental sources of energy that a nanogenerator can exploit: mechanical or vibrational energy from natural sources or industrial machines, kinetic energy in water drops, mechanical waves, gradients of temperature between the device and its surroundings, microwaves radiation, etc. Due to the low power demand of most of these new devices, scavengers can meet their power necessities, making them independent from the power grid. Furthermore, scavengers can work as sensors. This means that wireless sensor networks (WSN) can be implemented by using these systems.

The arise of nanogenerators technology means a huge advance in the field of portable and standalone devices. Not only because the power supply is no longer a problem, but also due to the miniaturization enhanced associated with this technology in comparison to conventional batteries. Due to the lastest advances in material physics, especially in terms of surface engineering, nanogenerators sizes can be highly adaptable. This leads to the fabrication of nanogenerators of some centimetres which are used, for example as rectennas in reference [12] to the scale of millimetres used in implantable devices as reported in reference [13]. Therefore,

nanogenerators can work as wireless, power-independent sensors with high flexibility in terms of shape and size.

There are several good examples of the high prospect of the nanogenerators field. For instance, reference [14] proposes a nanogenerator that powers several devices using biomechanical energy extracted from human motion. In addition, reference [15] discusses the potential applications of nanogenerators working as sensors for health monitoring. Another example worthy to be mentioned is reference [16]. There, a magneto-mechano-electric nanogenerator (MME) is presented to convert low-frequency stray magnetic fields into useable electric energy. As the last example, reference [17] shows a Thermo-Electric Nanogenerator (TEGs) that make use of the heat dissipated in smartphones to recharge the battery.

3.2 General insight into types of energy harvesters.

Nanogenerators can harvest energy from different types of environmental sources.[18], which determines the following classification.

3.2.1 Thermoelectric scavengers

Thermoelectric scavengers, also known as Thermoelectric Generators (TEGs), extract electric energy from a temperature gradient thanks to the Seebeck effect. The harvesting process is based on the current generated by the action of two bound metals exposed to a temperature gradient [19]. In this system, the current is generated difference between the electronic potentials of both metals. The temperature difference between the extremes of the two metals causes a migration of the charge carriers from one material to the other in other to minimize their energy.
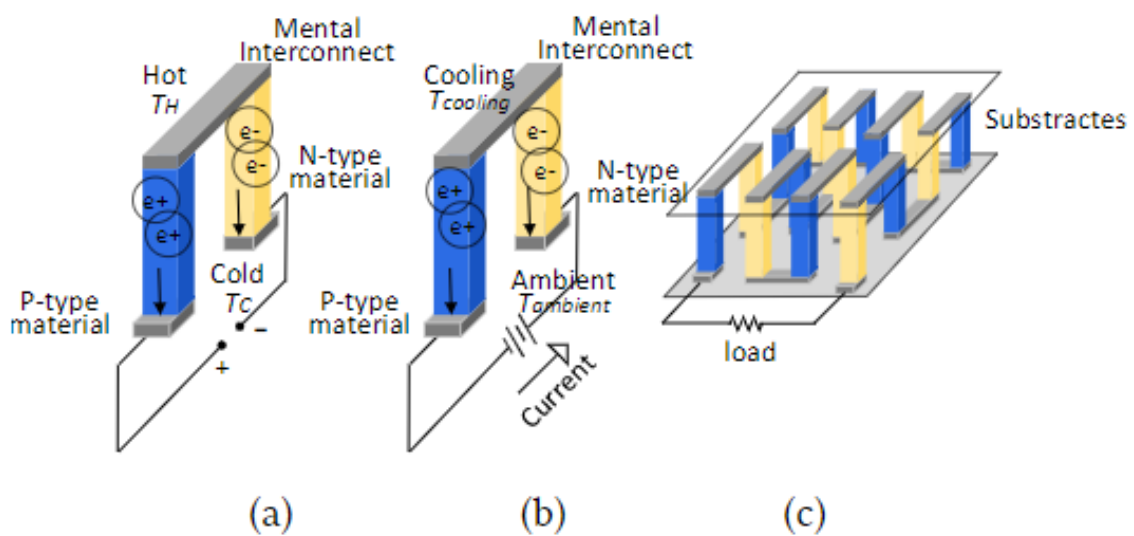
Figure 3.1. *Sketches of TEGs and TECs. a) shows the sketch of a single TEG. b) presents the sketch of a TEC. c) an array of TEGs connected in parallel is shown* [17].

5

The Seebeck effect does not take place only in metals but in most conductors and semiconductors. In Figure 3.1 a) a TEG is shown. This consists of an n-type material bound to a p-type material using metals to create de contacts. Moreover, a set of TEGs can be connected in parallel to increase the power output. This kind of scavenger is getting popular as a recycler of the energy wasted by the Joule effect in modern devices experiencing high power dissipation [20].

3.2.2 Pyroelectric scavengers

The pyroelectric effect is one of the best ways to harvest energy from thermal sources. Instead of temperature gradients, pyroelectric energy harvesters (PyEHs) [21] use energy from temperature fluctuations [22]. This effect is significative intense in ferroelectric materials like Pb(Zn, Nb)O_3PbTiO$_3$, and PVDF-TrFE between others, as it is described in [23]. First, researchers showed that the pyroelectric devices were less efficient than Thermoelectric scavengers. However, current developments in nanotechnology have allowed the fabrication of pyroelectric films with a pyroelectric response four times more intense than in bulk.

3.2.3 RF Energy harvesting

Radio-Frequency (RF) energy harvesters extract power from the radiofrequency radiation that is found in the environment. Using LC circuits, these scavengers can translate the potency carried by the incoming radiation [24] to energy stored in a capacitor. Because the RF energy density in the environment is considerably low comparing with power in RF circuits, most of these Rectennas work using Harvest-Store-Use (HSU) architecture, also known as switching techniques described in detail in [25]. In an architecture HSU, the capture of the incoming energy and its transmission into the capacitors is performed in two different time steps.
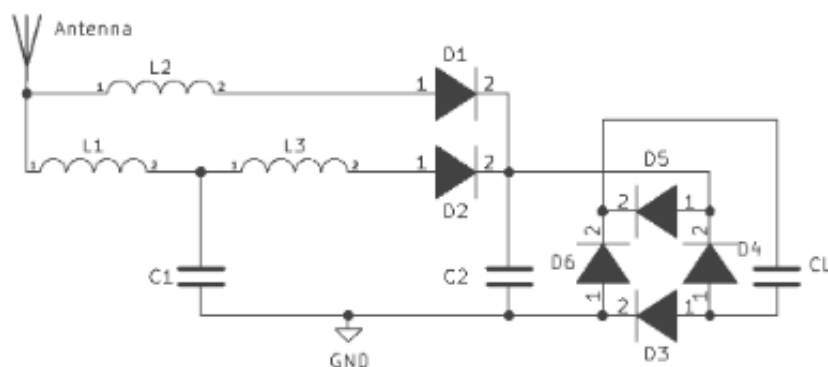

Figure 3.2. *Circuit for an* RF energy harvester. *It is formed by a first bridgeless converter followed by a diode bridge working as a full-wave rectifier.* [26]

Figure 3.2 shows the circuit model used in reference [26] In this model, a bridgeless converter is formed by the inductors L1, L2 and L3, the capacitors C1 and C2 and the diodes D1 and D2. The bridgeless converter is used to implement the switching technique, where the polarization of the diodes dictates when the circuit is capturing the incoming energy (reverse biased) and when it is transmitted to the next stage of the circuit (forward-biased). Then, the signal is conducted to a diode bridge, being rectifying to DC and then stored in CL [26].

3.2.4 Kinetic energy harvesters

Kinetic energy scavengers transform mechanical environmental energy into electric energy. One of the most promising scavengers in this group is those based on electrostatic induction [27]. Within this group, we can identify Triboelectric Nanogenerators (TENGs) [28] and Piezoelectric Nanogenerators (PENGs) [29], based on the triboelectric effect and piezoelectric effect respectively[30].
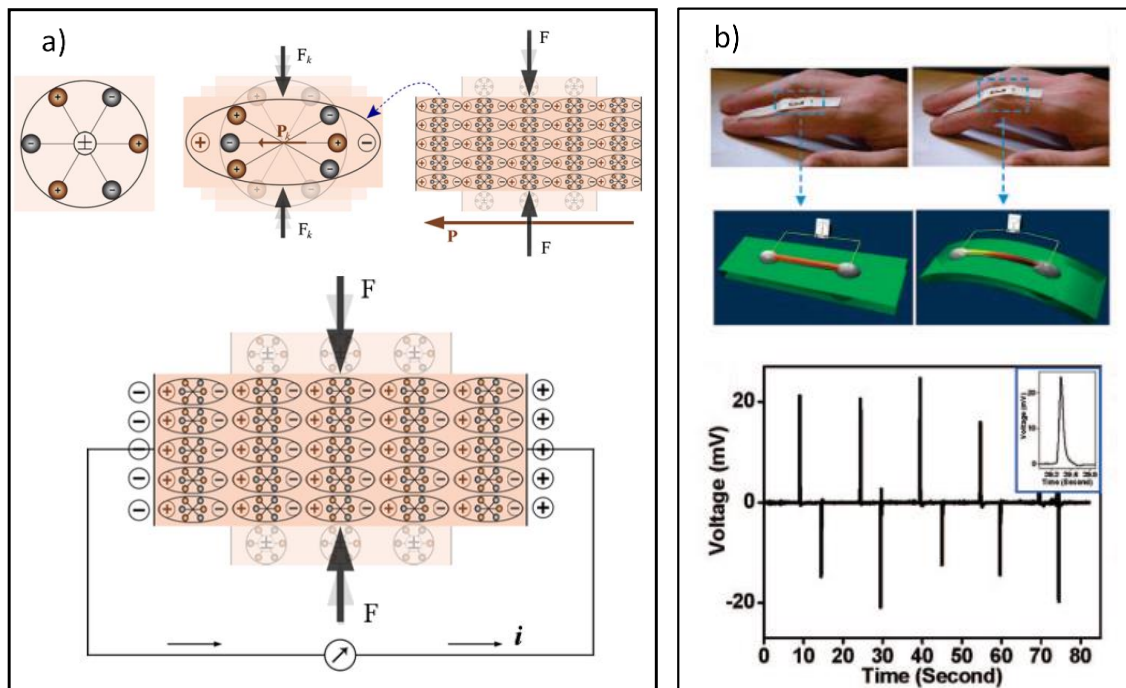
***Figure 3.3**. PENG operation. Image a) gives a visual explanation of the piezoelectric phenomenon* [31]. *Image b) is an example of a nanowire PENG used in* [32]*.*

Since this master Thesis focus on TENGs, they are deeply explained below in section 3.3. Therefore, the current just briefly introduces PENGs for completeness. The physical principle of PENGs is described in Figure 3.3. a) for a non-ferroelectric material. In the beginning, in the

absence of any mechanical perturbation, the natural structure of the piezoelectric material does not show any dipolar moment since the centre of negative and positive charge distribution coincides. When the system is subjected to a mechanical deformation the crystalline net is distorted. In the case of non-centrosymmetric crystalline structures, this produces charge displacement leading to the development of surface potential. When the extremes of charged surfaces are contacted through a metal a flow of free charges is generated to compensate for the induced surface potential. On the other hand, Image b) is an example of a PENG based on a Single Wire Generator (SWG) which consists of a nanowire of ZnO placed on a flexible substrate [32].

In the state-of-the-art of nanogenerators, PENGs have historically occupied a prominent position. On the other hand, TENGs are relatively new but increasing their relevance on the field. TENGs function description is shown in further sections in more detail due to its relevance for this Master Thesis.

3.2.5 Hybrid nanogenerators

Singel source scavengers normally produce low magnitude energies (micro energies). To cope with this limitation hybrid nanogenerators, able to harvest energy from more than one type of source, are currently in development. Such hybrid systems combine different energy harvesters, an approach that leads to a significant increase in the power output. There are some particular combinations of nanogenerators that are of interest. For instance, TENGs and PENGs combinations have been reported in the literature types of energy as the best way to enhance high-efficiency mechanical nanogenerators. For example in [33], such hybrids are used in health monitoring.

Other researchers have tried to combine nanogenerators that can use more than one source of energy. An example of this is reference [34] where an electromagnetic-triboelectric hybrid has been designed in order to capture mechanical energy on a keyboard.

3.3 The Triboelectric Nanogenerator

In this section, the operation of triboelectric scavengers is discussed in detail, since Triboelectric nanogenerators have special relevance in this work. Although the developed characterization set-up is in theory functional for any mechanical nanogenerator, it has been mainly designed tested for TENGs.

3.3.1 The triboelectric effect

As it was already set, TENGs are nanogenerators based on mechanical energy which use electrostatic induction as a working principle. In contrast with PENGS, in the case of TENGs, the surface potential is induced by the triboelectric effect.

The triboelectric effect consists of two different processes. First, the tribology effect produces surface free charges due to friction. Afterward, the generated free electrons are preferentially transferred to one of the involved surfaces (the denominated triboelectric layer) by contact electrification. In the latter process, the difference of electronegativity between the two surfaces is the driving force for an effective charge transfer. Because of this process, two charged surfaces of different sing are created.

Most of the authors use the term "triboelectric material" to identify those surfaces able to gain and store a high density of electrons. But actually, the intensity of the triboelectric effect does not exclusively depend on the characteristics of this single layer, but the triboelectric pair formed by the electron-donor and the electron-acceptor layers. This is so because the contrast between the electronegativity of these two surfaces determines the intensity of the charge transfer process [35]. The variety of triboelectric pairs is very wide. One of the most common kinds of pairs for TENGs is dielectric-metal pairs. In these systems, the free electrons gained during contact electrification are trapped in the dielectric side, creating a lasting charge distribution. This stable surface charge trapped on the dielectric surface is the cornerstone to produce electrostatic induction, as it is discussed in the following sections [36]. For the sake of simplicity, the dielectric electron-acceptor material is normally denominated the "triboelectric layer".

3.3.2 TENGs configurations

The triboelectric effect allows multiples approaches in other to extract power. there is not a unique architecture for TENGs, existing different possible operating modes. However, the basic principle of all of them is always the same. The movement of an electrode is in the presence of a triboelectric charged surface, breaks the electrostatic equilibrium, leading to charge transfer. A concise description of the most popular TENG configurations can be found in [37] and [38]:

● **Vertical contact-separation mode (Mode I):** This is the most common TENG configuration [39], [40]. It consists of two electrodes, one of them coated with a dielectric material with a triboelectric surface, commonly on the bottom electrode (cf. Figure 3.4). When the electrodes enter in contact, a charge transfer occurs, and a lasting surface charge is generated on the triboelectric layer. Then, the top electrode is gradually removed and a gap between electrodes is created, which forms a capacitor. The gradual movement of the top electrode modifies the

capacitance between electrodes. This variable capacitor, in the presence of the surface charge of the triboelectric layer, causes a variable voltage inside the device. This voltage variation in turn generates a flow of free charge between electrodes through the external load. This cycle periodically reproduced is the cause ofthe generation of a stable AC signal.
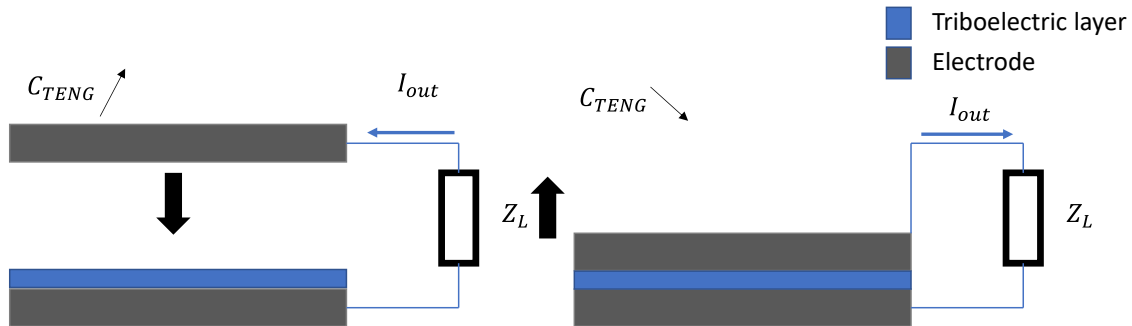
Figure 3.4*. Vertical contact-separation TENG diagram.*

- **Contact sliding mode (Mode II):** It is considerably similar to the vertical mode. The mean difference is the direction of the movement of the top electrode. In the contact sliding mode, the top electrode moves parallel to the layer, always in contact with it. Then, shear stress arises between both surfaces, which generates a triboelectric charge over the dielectric layer. Since the overlapping area between the bottom and the top electrodes constantly changes, the capacitance of the resulting periodically changes. This induces a current through the load as a consequence of the generated free charges. Contact sliding mode and contact vertical mode are based on the same variable capacitance principle. An example of this operation mode can be found in [41].
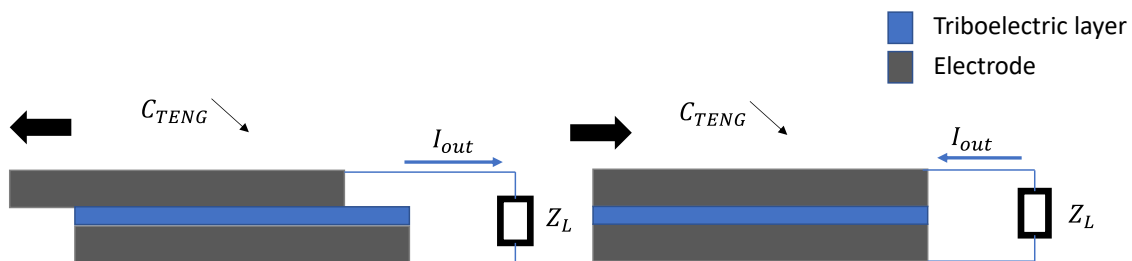
Figure 3.5*. Contact sliding mode TENG diagram.*

- **Single-electrode mode (Mode III):** The single-electrode mode was one of the very first discovered modes. It consists of just a triboelectric layer and a single electrode, which is connected to a load. When the triboelectric layer gets in touch with the electrode, a density charge is formed over the dielectric triboelectric layer. An opposite charge density develops in the electrode, restoring electrostatic equilibrium. Then, the separation of the triboelectric layer from

the electrode disturbs such equilibrium, removing the generated free charge from the electrode by driving it to the load. This mode usually generates less power than other architectures.
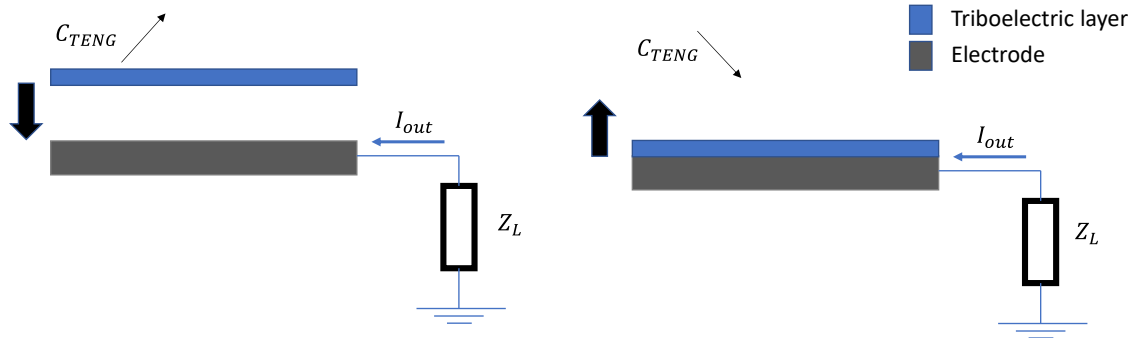

Figure 3.6. Single electrode mode TENG diagram.

- **Freestanding triboelectric-layer mode (Mode IV):** In this mode, two parallel electrodes are placed with a fixed position, while a triboelectric layer slides over both of them. The move of the triboelectric layer produces shear stress between the layer and the electrodes, producing a surface charge over the dielectric layer. As the triboelectric layer goes from one electrode to the other, the induced charge on the electrode surfaces varies with the change of the overlapping area between the layer and each electrode. In this way, when this overlapping surface is reduced for one of the electrodes, it starts to transfers charge to the other electrode, restoring electrostatic equilibrium. Therefore, a current is induced due to the movement of the layer. This mode is very extended among the literature [42], [43].
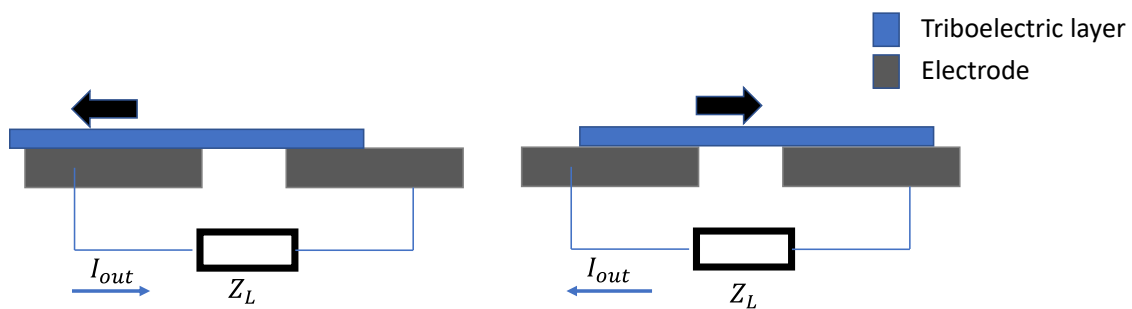
Figure 3.7. Freestanding triboelectric-layer mode TENG diagram.

3.3.3 TENGs operation principles in vertical contact-separation mode

To understand the function of a TENG, this development is based on the configuration shown in Figure 3.8. This description is strongly inspired by references [2], [8]. For this study, the triboelectric material is PFA (Perfluoroalkoxy alkane), but this description is of course general for every triboelectric material.

11

Let us consider a dielectric-triboelectric layer made of PFA attached through a dielectric adhesive tape onto a metallic electrode (bottom electrode). The thickness of this PFA layer is d_{PFA} and its dielectric constant is ε_{PFA}. Between the metallic constant and the PFA layer, there is tape working as an isolator, with a thickness d_{tape}, and a dielectric constant ε_{tape}. On the top side, a metallic electrode (top electrode) move periodically in the vertical direction and contact the PFA layer at its lowest point of the cycle. In this scheme d_{var} is the variable distance between the top electrode and the PFA layer. The top and bottom electrodes are connected to a load, Z_L.

When the top electrode contacts PFA, by triboelectric effect, the PFA surface acquires a negative charge density. The total charge over the PFA layer is Q_{TE}. Consequently, a positive charge density develops over the top electrode, Q_{var}, and bottom electrode, Q_{die}, due to electrostatic induction. The distance between the top electrode to the PFA layer determines the charge density in the metallic electrodes.

Some considerations may be done in order to simplify the calculus. It is assumed that the contact between the top electrode and PFA is completely homogeneous. Hence, the generated density charge is homogeneous among PFA extensions. In addition, border capacitances are neglected.

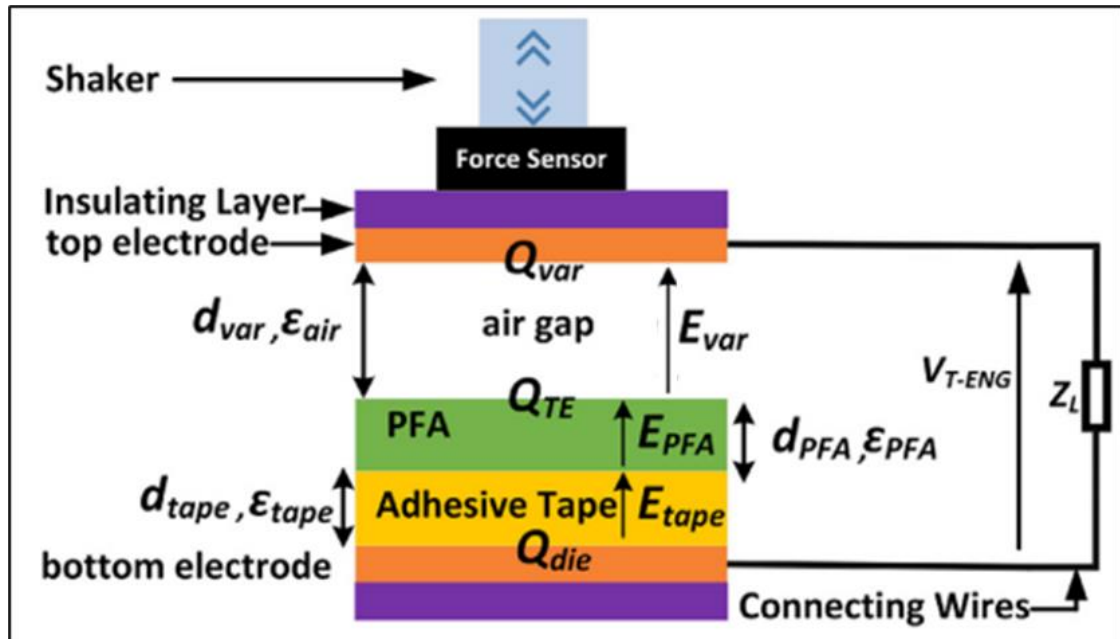**Figure 3.8**. *Sketch of a TENG which uses PFA as a triboelectric layer.* [8]

In addition, charge leakage on the PFA surface is also neglected. Although the PFA has strong dielectric properties, some charge flow to the bottom electrode, discharging the PFA surface. This neglection is then legit if it is considered that the tapping rate of the top electrode is high enough to compensate for the charge losses.

Furthermore, the charge on the PFA surface cannot grow forever. There is a certain point where an additional amount of charge is no longer sustainable due to electrostatic repulsion. In this situation, the saturation point is achieved. This point is indeed the consider steady state of the device. The charge density on the triboelectric layer, σ_{TE}, can be express in terms of the time using a dynamic charge model [2],:

$$\sigma_{TE} = \sigma_{TE}(0) + \Delta\sigma_{TE}(t) = A + Be^{-\frac{t}{\tau}} \tag{3.1}$$

Where the constants A and B are determined by the initial and saturation values of the charge density:

$$A + B = \sigma_{TE}(0) \; ; \; A = \sigma_{TE}|_{saturation} \tag{3.2}$$

Where $\sigma_{TE}|_{saturation}$ is the charge density on the PFA when it reaches the saturation state. Henceforth, σ_{TE} is referred to its value in the steady-state to detail how it works. Then, it is assumed that $\sigma_{TE} = \sigma_{TE}|_{saturation}$ after a transition time. As any electrostatic induced device, its function can be described using the Gauss law of the Maxwell Equations:

$$\nabla \cdot \mathbf{D} = \rho \tag{3.3}$$

In which $\mathbf{D}$ is the electric displacement vector and ρ is the free charge density present in the system.

The system can be understood as the classic problem of a planar capacitor where a dielectric has been placed in the middle, with the only distinction that there is a surface charge distribution at a certain height of the bottom electrode. Therefore, it is consistent to think that electric fields are constant in each region, being orthogonal to the surface of the electrodes. This permits the use of scalar description. Therefore, applying Gauss law it is possible to find the following relationships:

$$E_{var}(t) - \varepsilon_{PFA}E_{PFA} = \frac{\sigma_{TE}}{\varepsilon_0} \tag{3.4}$$

$$\varepsilon_{tape}E_{tape} = \varepsilon_{PFA}E_{PFA} \tag{3.5}$$

Where ε_0 is the vacuum electric permittivity, E_{var} is the electric field between the PFA layer and the top electrode and E_{PFA} is the electric field inside the PFA. The electric permittivity of the air has been taken as the vacuum electric permittivity, in other words, $\varepsilon_{air} = 1$. Because this is an isolated system, due to charge conservation and electrostatic equilibrium the following relationship should be satisfied (magnitudes defined above c.f. Figure 3.8 and in the figure description):

$$Q_{var} + Q_{TE} + Q_{die} = 0 \rightarrow Q_{die} = -(Q_{TE} + Q_{var}(t)) \tag{3.6}$$

Then, Q_{die} is defined by Q_{var} and Q_{TE}. The relationship between Q_{var} and Q_{die} with the electric field is also defined by the Gauss law in the following way:

$$\sigma_{var} = -\varepsilon_0 E_{var} \tag{3.7}$$

$$\sigma_{die} = -\varepsilon_0 \epsilon_{tape} E_{tape} \tag{3.8}$$

Being E_{tape} the electric field inside the tape. Integrating these electric fields, the output voltage of the whole device, V_{TENG} can be written as:

$$V = -\int_{\Gamma} \boldsymbol{E} \cdot \boldsymbol{d\Gamma}$$

$$V_{TENG}(t) = -d_{var}E_{var} - d_{PFA}E_{PFA} - d_{tape}E_{tape} \tag{3.9}$$

Taking into account expressions (3.4), (3.5), this can be rewritten as [2]:

$$V_{TENG}(t) = \frac{\sigma_{TE}}{\varepsilon_0}\left(\frac{d_{tape}}{\varepsilon_{tape}} + \frac{d_{PFA}}{\epsilon_{PFA}}\right) + \frac{\sigma_{var}(t)}{\varepsilon_0}\left(d_{var}(t) + \frac{d_{PFA}}{\varepsilon_{PFA}} + \frac{d_{tape}}{\varepsilon_{tape}}\right) \tag{3.10}$$

Being this the fundamental expression of such device. Therefore, by varying the distance between the PFA layer and the top electrode a voltage variation is achieved. If a load Z_L is connected to the device, the movement of the top electrode pumps charge into the load, recovering the equilibrium. Therefore, part of the mechanical energy of the top electrode is transmitted to the load as electric energy.

3.3.4 TENG lumped model

It can be seen in expression (3.10), that the output voltage can be divided into two arguments. The first one of these arguments is constant in time, since the distance between the PFA layer and the adhesive tape is fixed, being considered as a fixed capacitor. Furthermore, if the charge stored on the PFA is assumed to be constant, this fixed capacitor works as a voltage source. On the other hand, the second term is behaving like a variable capacitor since $d_{var}(t)$ depends on the movement of the top electrode, varying in the process the value of $\sigma_{var}(t)$. Therefore, the output voltage, $V_{out}(t)$ can be expressed a the sum of the voltage of a DC source, V_{offset} and the voltage across the variable capacitor, $V_{var}(t)$, which can be expressed as follows [2]:

$$V_{out}(t) = V_{offset} + V_{var} = \frac{Q_{TE}}{C_0} + \frac{Q_{var}(t)}{C_{var}(t)} \tag{3.11}$$

Where C_0 is the capacity of the fixed capacitor working as a DC voltage source, and $C_{var}(t)$ is the capacitance of the variable capacitor. This model is illustrated in Figure 3.9 a) which shows

both capacitors without making any assumption about the Q_{TE} time dependence. Once Q_{TE} is defined as a constant, this capacitor is assumed to behave like a DC source (Figure 3.9 b). In this model the involved capacitances can be written according to expression (3.10) in the following way [2]:

$$C_0 = \frac{S\varepsilon_0}{\frac{d_{tape}}{\varepsilon_{tape}} + \frac{d_{PFA}}{\varepsilon_{PFA}}} \qquad ; C_{var}(t) = \frac{S\varepsilon_0}{d_{var}(t) + \frac{d_{tape}}{\varepsilon_{tape}} + \frac{d_{PFA}}{\varepsilon_{PFA}}} \tag{3.12}$$

Being S the overlapping surface between the top electrode and the PFA layer.
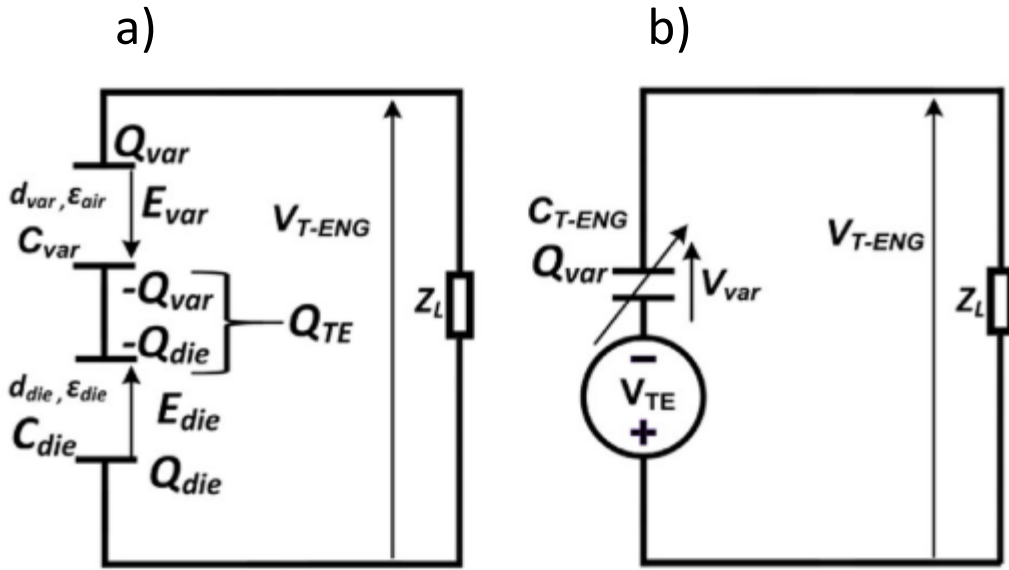

Figure 3.9. *TENGs electric model* [8]. *a) Two capacitors model b) TENG model for a constant Q_{TE}.*

3.3.5 Empirical expression for the variable capacity

This model is strongly inspired in reference [8]. Although expressions (3.11) and (3.12) can be used for experimental purpose, the truth is they are hard to use due to how difficult is to take a precise measurement of the magnitudes d_{PFA} and ε_{PFA}. In order to overcome this issue, we express the capacitance of the system in terms of the experimental measurements. Therefore, in this section, an expression for the variable capacitance is shown, only depending on the minimum and maximum total capacitance of the complete TENG, $C_{max,}$ and C_{min}. An initial consideration has to be made about how the electrode moves. In this model, the dumping introduced by the mechanical inertia of the top electrode is not considered. The starting point of such development is the expression (3.12) [8]:

$$C_{var}(t) = \frac{S\epsilon_0}{d_{var}(t) + \frac{d_{tape}}{\varepsilon_{tape}} + \frac{d_{PFA}}{\varepsilon_{PFA}}} = \frac{A}{1 + d'(t)} \tag{3.13}$$

The idea is to express A and $d'(t)$ in terms of C_{max} and C_{min}. Of course, this new $d'(t)$ is no longer the distance between plates. Therefore, assuming that at time 0, $d'(t)$ is also 0, the variable capacitor should find its maximum value:

$$C_{var}(t) = A = C_{var}|_{max} \tag{3.14}$$

The relationship between $C_{var}|_{max}$ and C_{max} is made by the equivalent capacitor formed by the fixed capacitor and the variable one:

$$C_{eq} = \frac{1}{\frac{1}{C_0} + \frac{1}{C_{var}}} \tag{3.15}$$

Looking at expression (3.13), the maximum value of the TENG capacity is reached when d_{var} reaches its minimum value. At this value, C_{var} matches with C_0. Then, the following approximation is made:

$$if \ d_{var}|_{min} \cong 0 \rightarrow \ A = \frac{S\epsilon_0}{\frac{d_{tape}}{\epsilon_{tape}} + \frac{d_{PFA}}{\epsilon_{PFA}}} = C_0 \rightarrow C_{eq} = \frac{C_0}{2} = C_{max} \tag{3.16}$$

And therefore, the maximum value of C_{var} is:

$$A = C_{var}|_{max} = 2C_{max} \tag{3.17}$$

In the case of the minimum capacitance that C_{var} can achieve, it is necessary to find out which is the maximum value for $d'(t)$. Rewriting expression (3.15):

$$C_{eq} = \frac{1}{\frac{\frac{d_{tape}}{\epsilon_{tape}} + \frac{d_{PFA}}{\epsilon_{PFA}}}{S\epsilon_0} + \frac{\frac{d_{tape}}{\epsilon_{tape}} + \frac{d_{PFA}}{\epsilon_{PFA}} + d_{var}(t)}{S\epsilon_0}} = \frac{S\epsilon_0}{2\left(\frac{d_{tape}}{\epsilon_{tape}} + \frac{d_{PFA}}{\epsilon_{PFA}}\right) + d_{var}(t)} \tag{3.18}$$

As explained before, there is an experimental limitation to measure the actual values of the relative dielectric constant and thickness of the tape and the PFA. However, since the value of interest is the capacitance when the distance between the PFA layer and top electrode is maximum, the following approximation can be made:

$$\left(\frac{d_{tape}}{\epsilon_{tape}} + \frac{d_{PFA}}{\epsilon_{PFA}}\right) \ll d_{var_{max}} \tag{3.19}$$

Since the thickness of the tape and the PFA are around 2 orders of magnitude smaller than the variable gap, and the dielectric constants of the tape and the PFA are higher than the de unit, this approximation is solid. Therefore, expression (3.18) can be written as:

$$C_{eq} \cong \frac{S\varepsilon_0}{\frac{d_{tape}}{\varepsilon_{tape}} + \frac{d_{PFA}}{\varepsilon_{PFA}} + d_{var}|_{max}} = C_{var}|_{min} = C_{min} \tag{3.20}$$

Then the value maximum value of *d'(t)* can be deduced using expressions (3.13) and (3.20):

$$C_{var}|_{min} = \frac{A}{1 + d'_{max}} \cong C_{min} \rightarrow d'_{max} = \frac{C_{max} - 2C_{min}}{2C_{min}} \tag{3.21}$$

At this point, is necessary to establish how *d'$_{var}$(t)* depends on time. In this study and harmonic displacement of the top electrode is assumed, which is the scenario experimentally studied in the next chapters. Thus, *d'$_{var}$(t)* behaves like a harmonic oscillator between 0 and *d'$_{var}$* according to the following expression:

$$d'_{var} = \frac{d'_{max}}{2}(1 + \cos(\omega t)) \tag{3.22}$$

Since no inertial consideration has been included, this model does not show any dumping. This is an important factor to consider in the comparison between simulations and experimental results, discussed in Chapter 6.

Including the constant *A* and the function, *d'$_{var}$* in expression (3.13), it can be written:

$$C_{var} = \frac{2C_{max}}{1 + \frac{2C_{max} - C_{min}}{2C_{min}}(1 + \cos(\omega t))} \tag{3.23}$$

However, this model has a flaw. It sets that the minimum capacitance of the TENG is only achieved when the cosine term is strictly 1. This is far from true since C_{min} is achieved at a certain critical distance between the triboelectric layer and the top electrode. This critical distance is considerably smaller than the maximum possible distance. Therefore, For distances bigger than such critical distance, *C$_{var}$ (t)*is always at C_{min}.

Since it is considerably difficult to measure experimentally this distance, expression (3.21) has been reformulated to achieve a more accurate model:

$$W(t) = \frac{2C_{max}}{1 + \frac{2C_{max} - C_{min}}{kC_{min}}(1 + \cos(\omega t))} \tag{3.24}$$

$$C_{var}(t) = \begin{cases} W(t) & if\ W(t) > C_{min} \\ C_{min} & if\ W(t) < C_{min} \end{cases} \tag{3.25}$$

Where $C_{var}(t)$ is only equal to $W(t)$ if its value is higher than C_{min}. In $W(t)$ expressions, a parameter k has been introduced to control in which fraction of the working period $C_{var}(t)$ remains at C_{min}. Therefore, k works as a tuning parameter in order to fit simulation with experimental results.

3.3.6 TENG electric properties

According to the literature, TENGs have some electric properties that need to be considered.

- **TENGs high voltage output.** The charge that triboelectric films can store is very variable, depending on the material. Usually, the voltage of the fixed capacitor can be in the order of hundreds of volts. This produces too strong voltage peaks to be handled by most electronic devices, being able to damage the employed equipment if the necessary precautions are not taken [44].

- **TENGs high internal impedance**. Most solid-solid TENGs tend to show very high internal impedances [45]. This is due to the capacitor structure TENGs have. Assuming that the internal impedance of the TENG can be understood as the internal impedance of an equivalent capacitor, then it is possible to write that [45]:

$$|Z_{TENG}| = \frac{1}{2\pi f C_{eq}} \tag{3.26}$$

Being f the working frequency and C_{eq} the equivalent capacitance. In the literature, it has been reported that the maximum and minimum capacitances of TENG devices are usually in the range of nF [45]. Then, assuming a low working frequency like 5 Hz, the internal impedance of the TENG is the following:

$$|Z_{TENG}| = \frac{1}{2\pi f C_{eq}} \sim \frac{1}{2\pi \cdot 5 \cdot 1 \cdot 10^{-9}} \cong 30 \ M\Omega$$

These impedances are too high for most electronic devices, making it impossible to read TENGs signal using only a conventional reading system [46], [4]. Therefore, to use TENGs in a practical way, its signal needs to receive the correct conditioning. This topic is discussed in the following section.

3.4 Conditioning circuits for TENG devices

This section aims to introduce conditioning circuits function. Since the experimental and simulation chapters of this work are focused on TENG devices, this section only considers such type of nanogenerator.

### 3.4.1 Generalities of conditioning and power management circuits.

TENG efficiencies in power conversion are considerably high. However, its high impedance makes it impossible to connect the device directly to a conventional power management circuit, due to mismatch issues [3]. Therefore, TENG's signal needs to be conditioned as illustrated in Figure 3.10
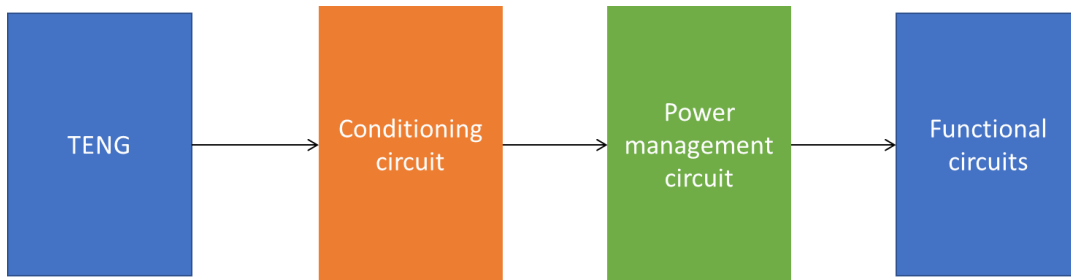
Figure 3.10. General architecture of a power supply based on TENG.

In order to make TENG signal useful for the power management circuit, an intermedial conditioning circuit has to adapt the signal of the TENG. Once its power is successfully transmitted to the power management circuit, this module powers up the rest of the functional circuits of the device of interest.

There are different architectures for the conditioning circuits. All of them are based on the same idea of accumulating the transmitted energy from the TENG into a capacitor [3]. This general mechanism is shown in Figure 3.11.
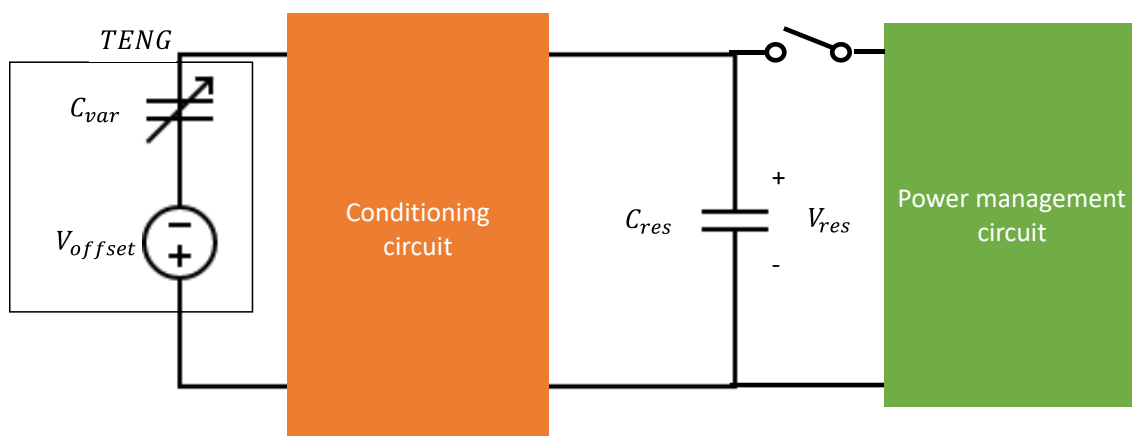
*Figure 3.11. The general approach of the conditioning circuits.*

The conditioning circuit accumulates the transmitted power into a reservoir capacitor named C_{res}. Then, at some point the capacitor is connected to the power management circuit, transmitting the accumulated energy. There is not a unique approach to transmit the stored energy in C_{res} to the power management system, but it usually needs some control circuit to decide when the reservoir capacitor is allowed to discharge. For example, a switch-based transmission using an LC-oscillator can be used [47].

This connection between the power management circuit and the reservoir capacitor should be done at the conditions of maximum power transmission from the TENG to the reservoir capacitor. Most of the conditioning circuits of interest have a property called auto-increasing [48]. Auto-increasing conditioning circuits sets a new work frame for the next TENG cycle, due to the charge accumulation produced by previous iterations. Therefore, for this kind of circuit, there is a voltage value of V_{res} that guarantees maximum power transmission to such capacitor. This voltage value is named the optimal voltage operation point. Therefore, power management control should discharge the reservoir capacitor only when this capacitor is about to overpass the optimal voltage point. Also, its discharge should not be too aggressive, to not drag the voltage capacitor out of the region of interest [6].

3.4.2. Types of conditioning circuits based on its Q-V diagrams

As it has been set, every conditioning circuit aims to accumulate energy from the TENG into a reservoir capacitor, which is discharged by the power management system. The optimal approach is to maintain in the reservoir capacitor a voltage that assure the maximum power transmission from the TENG to the capacitor. Thus, it is absolutely important to control how much power the TENG is injecting into the capacitor per cycle.
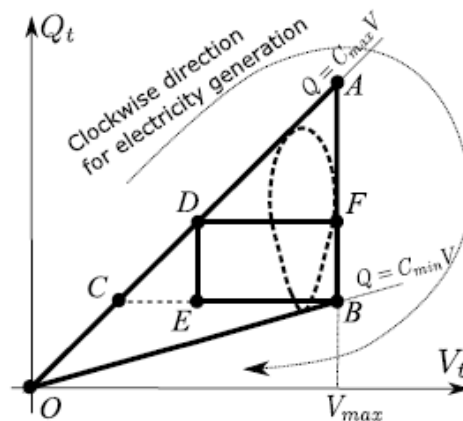
Figure 3.12*. Types of Q-V diagrams. Q_t and V_t are referred to the charge and voltage stored in the TENG. A tear-drop shape Q-V is plotted with dotted lines.* [49]

In order to calculate the output power per cycle, Q-V diagrams are useful tools. Figure 3.12 shows the possible three types of conditioning circuits based on their Q-V diagrams. For hence, the power a TENG can transmit in a single cycle to the reservoir capacitor is determined by the enclosed area in its Q-V diagram. Regarding the shape of their Q-V cycle, conditioning circuits can be classified in the following way:

- *Teardrop Q-V cycle conditioning circuits.* They are also named primitive conditioning circuits. An example of this kind of circuit can be seen in Figure 3.13 They are just based on an RC circuit connected directly to the TENG. For hence, they usually provide low power transmittance. Also, because no correction is applied, the voltage on the capacitor is on AC, which implies power losses since additional AC-DC converting is needed. They also are not auto-increasing, meaning that each iteration of the TENG cannot increase the power transmittance of the next one, since no charge is being accumulated. Also, the voltage transmitted to the capacitor in a cycle is of the same order of V_{offset}. This voltage is usually too high to be handle by microelectronic circuitry. Thus, these kinds of circuits are not very interesting for conditioning, and they are only used as a test method for TENG devices.
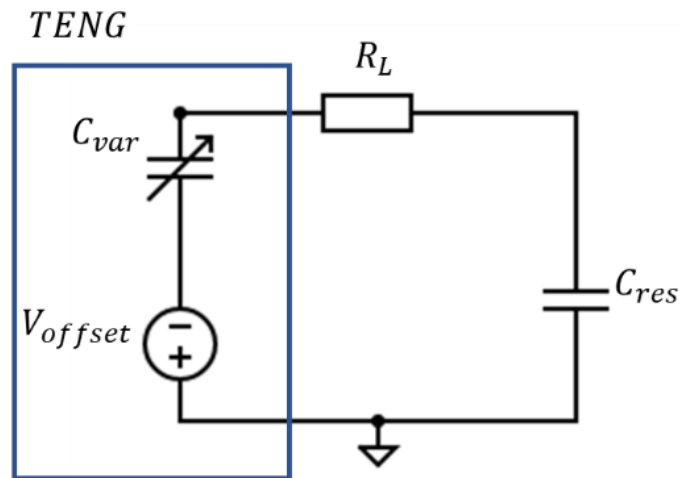

Figure 3.13. Circuit of a typical teardrop chape Q-V diagram.

- *Triangular Q-V cycle conditioning circuits*. An example of these kinds of circuits can be seen in Figure 3.14. These circuits are divided into two subgroups: the constant-voltage Q-V cycle, and the constant-charge Q-V cycle, depending on if there is a side of the triangle which is parallel to the charge axis or the voltage axis, respectively. In the Figure example, the presented circuit is a voltage-constant circuit. It is shown that triangular conditioning circuits are the theoretical optimal ones in terms of power transmission per cycle. In addition, most advanced triangular Q-V cycle circuits include rectification and show auto-increasing

properties. But they have two major flaws. First of all, they need a switch system to work, which implies external control. This is very restrictive since this control needs to be fed by the TENG, leading to important practical problems. Also, they usually need to work with high voltages to obtain high efficiencies. These voltage values usually are too high for conventional microelectronic power systems. Because of this, they are not usually used.
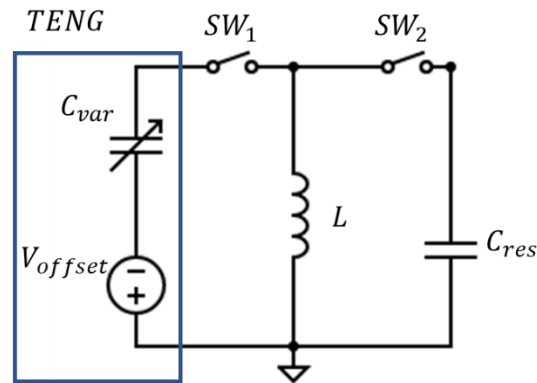
***Figure 3.14.** Example of a triangular Q-V cycle conditioning circuit.*

- ***Rectangular Q-V cycles conditioning circuits.*** On the TENG conditioning state-of-art, this group is preferred. Although they cannot match the maximum efficiencies of the triangular Q-V cycles, they allow us to work with lower voltages with reasonably good efficiencies. In addition, they can be set only with passive elements. Also, the use of diodes assures in most cases that the circuits show auto-increasing properties by charge accumulation in the reservoir capacitor. These are the reasons why they are the favorites ones in the field nowadays [37].

The used conditioning circuits in this study are rectangular Q-V cycles circuits. Indeed, the circuits used are the half-wave and full-wave conditioning circuits. They both work with the charge pump principle, being based in the classical half-wave and full-wave rectifier respectively. A detailed description of both circuits is be carried out in the following sections.

3.4.3 Function of half-wave conditioning circuit and the Charge pump principle

The half-wave conditioning circuit uses a rectangular Q-V diagram. Its diagram circuit is shown in Figure 3.15. Its operation is based on diodes correction. Diodes provide an accumulation voltage effect over the reservoir capacitor without the need for additional control circuitry. The explanation of the half-wave conditioning circuit function is used to explain how a charge pump-based conditioning circuit works. This is useful since once a circuit is shown to be charge pump-based, power calculations can be easily made using its Q-V cycle diagram.
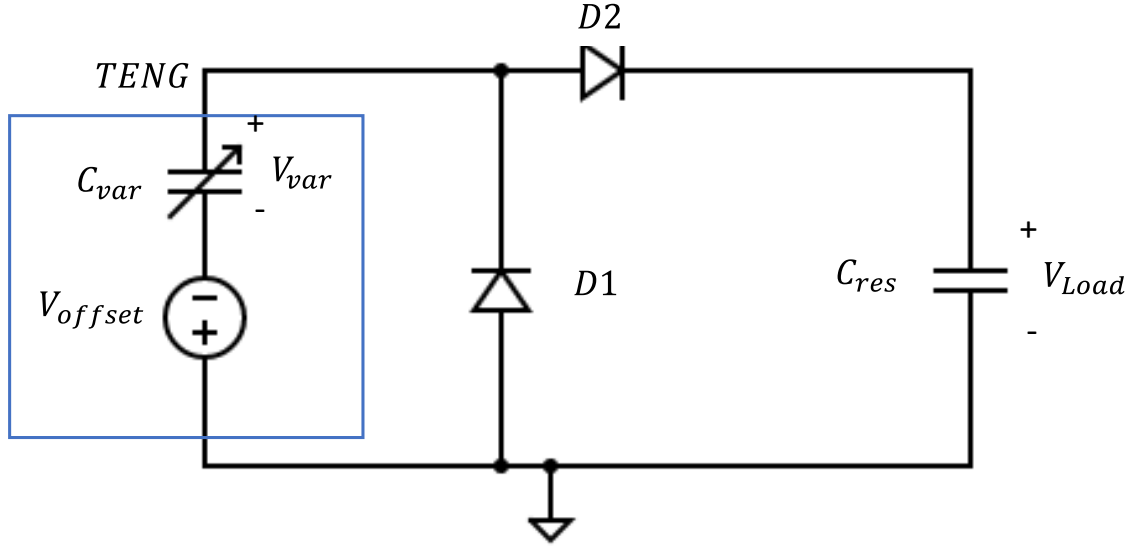
Figure 3.15. *Half-wave conditioning circuit for TENG devices.*

The half-wave operation is the following. Assuming from the point of start that C_{res} is in equilibrium with the TENG, both having an equal initial voltage V_0. TENG is initially at its lowest capacity, C_{min}. In this situation, all diodes are in their off state. Then, the top electrode of the TENG starts to get closer to the bottom plate, increasing the capacity of the TENG. Because in this situation TENG cannot transfer charge because diodes are still off, the voltage in the variable capacitor starts to decrease. This breaks the equilibrium state of diode D1. Assuming that the used diodes are perfect and neglecting their forward voltage threshold, D1 equilibrium is only be restored when [49]:

$$V_{var} = V_{offset} \tag{3.27}$$

This equilibrium is only achieved when the TENG achieves its maximum capacity. Then, the charge on the variable capacitor is:

$$Q_{max} = C_{max}V_{offset} \tag{3.28}$$

In this situation, the top electrode is touching the triboelectric layer. When the top electrode starts to go away from the triboelectric layer, the capacitance of the variable capacitor starts to decrease. Again, since both diodes are off, C_{var} cannot transfer charge, and its voltage increases. This perturbs the equilibrium condition of diode D2. When the voltage in the variable capacitor is high enough, D2 turns on, transferring charge from C_{var} to C_{res}. This continues until C_{var} reaches its maximum voltage in this cycle, which is:

$$V_{var}|_{max} = \frac{Q_{max}}{C_{min}} = \frac{C_{max}}{C_{min}}V_{offset} \tag{3.29}$$

23

Because C_{var} and C_{res} are now two capacitors in series (because D2 is on), its equilibrium condition is reached when both capacitors have the same charge. Therefore, a charge package, ΔQ, is transferred from C_{var} to C_{res}. Then, the equilibrium condition is the following ones [49]:

$$Q_{res}|_{new} = V_0 C_{res} + \Delta Q \tag{3.30}$$

$$Q_{var}|_{new} = C_{max} V_{offset} - \Delta Q \tag{3.31}$$

$$Q_{res}|_{new} = Q_{var}|_{new}$$

Therefore, the amount of charge transferred is:

$$\Delta Q = \frac{1}{2}\left(V_{offset} C_{max} - V_0 C_{res}\right) \tag{3.32}$$

Thus, the final voltages for both capacitors are:

$$V_{var}|_{new} = \frac{1}{C_{min}}\left(\frac{1}{2} V_{offset} C_{max} + V_0 C_{res}\right) \tag{3.33}$$

$$V_{res}|_{new} = \frac{1}{C_{res}}\left(\frac{1}{2} V_0 C_{res} + V_{offset} C_{max}\right) \tag{3.34}$$

And these are the initial values for the next cycle. This is, in general lines, the working principle of a charge pump. The V_{offset} charges the variable capacitor when it is at its maximum capacitance and then the variable capacitor pumps this charge into the reservoir capacitor when it achieves its minimum capacitance. Thus, more and more charge is accumulated into both capacitors until a saturation condition is achieved. This saturation condition arises when the voltage inside the variable capacitor is not high enough to pump charge through diode D2:

$$V_{var}|_{max} - V_{offset} = V_{res}|_{saturation}$$

$$V_{res}|_{saturation} = \frac{C_{max}}{C_{min}}\left(1 - V_{offset}\right) \tag{3.35}$$

At this point, the reservoir capacitor no longer receives charge from the TENG. Since voltages in both capacitors are growing after each cycle, this circuit has the auto-increasing property. Figure 3.16 shows this concept. The area inside a cycle grows from the initial state with further cycles. This increase of the output power in terms of the number of cycles stops at a certain point, where the TENG starts to find difficulties injecting additional charge into the reservoir capacitor. After this point of maximum power transmission, the area of the cycles decreases with further iterations. Therefore, the voltage operation points for V_{res} is achieved at this cycle with maximum area.
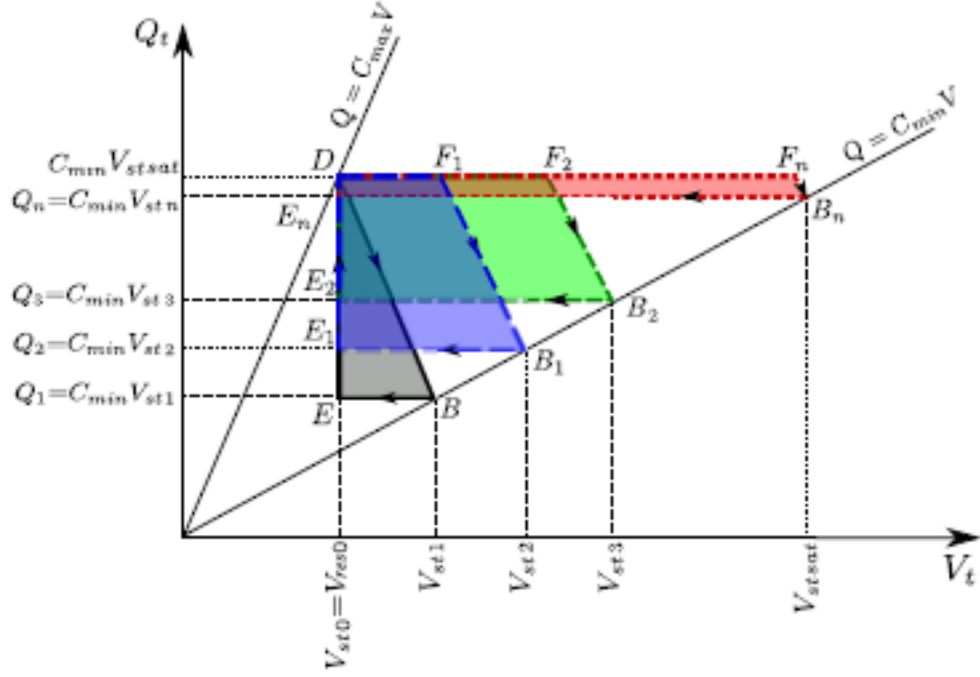
Figure 3.16. *Evolution of a charge pump conditioning circuit. V_t and Q_t corresponds with the used V_{var} and Q_{var} used in the description* [49].

The power of a cycle can be calculated by knowing the maximum voltage across the variable capacitor in such a cycle, and the maximum charge that it stores.

Therefore, the output power is calculated by calculating the area inside the Q-V cycle. Then, the additional energy injected in the reservoir capacitor by the n-cycle is:

$$\Delta W_n = (V_{var}|_{max} - V_{var}|_{min})(Q_{var}|_{max} - Q_{var}|_{min}) \qquad (3.36)$$

Being ΔW_n is the energy injected in the n-cycle. A more detailed development of these calculi can be found in [49], at its eleventh chapter. According to this reference, the energy transmitted in a cycle can be expressed as:

$$\Delta W_n = V_{offset} V_{res_n} \left[1 - \left(1 + \frac{V_{res_n}}{V_{offset}} \right) \frac{C_{min}}{C_{max}} \right] \qquad (3.37)$$

Where the condition, to have a positive increase of the energy is:

$$\frac{C_{max}}{C_{min}} > \frac{V_{res_n}}{V_{offset}} \qquad (3.38)$$

As expression (3.37) indicates that transmitted energy in a cycle has a quadratic dependence with V_{res_n}. Calculating its first derivative, it is possible to find the optimal operation point for V_{res} :

25

$$V_{res}|_{opt} = \frac{1}{2} V_{offset} \left(\frac{C_{max}}{C_{min}} - 1 \right) \qquad (3.39)$$

Being its maximum of injected energy in a cycle:

$$\Delta W_{max} = \frac{1}{4} V_{offset}^2 C_{min} \left(\frac{C_{max}}{C_{min}} - 1 \right)^2 \qquad (3.40)$$

Therefore, the maximum transmitted power depends directly on the ratio between the maximum and minimum capacitances and the value of V_{offset}.
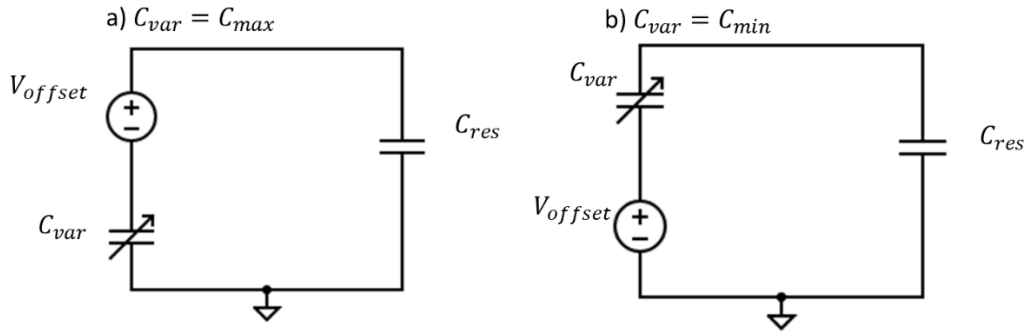
3.4.4 Full-wave conditioning

In this section, a qualitative explanation of the full-wave rectifier is given since its function is more complex than the case of the half-wave. In reference [49] to its eleventh chapter, by a series of circuit transformations, their authors show how this circuit can be changed into a typical charge pump conditioning circuit. For hence, they calculate its optimum voltage operation point and its maximum power transmission using its Q-V diagram. This explanation is certainly out of the main interest of this study. Therefore, only a qualitative explanation is provided. The circuit is shown in Figure 3.17.
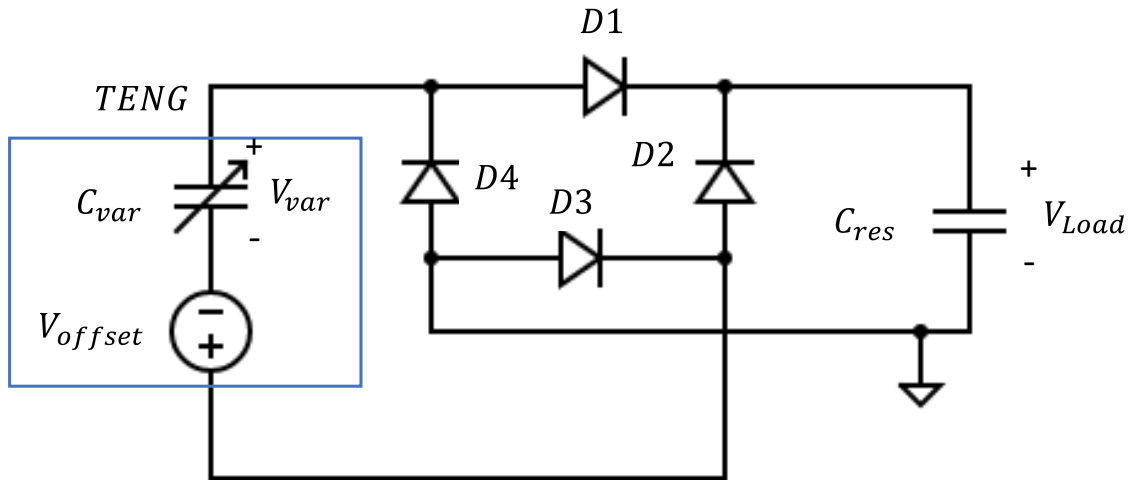
Figure 3.17. *Circuit diagram of the full-wave conditioning circuit.*

At first, there is an initial voltage in both capacitors. When the C_{var} starts to grow, the V_{var} decreases, disturbing the equilibrium. This makes diodes D2 and D4 switch on. Then, the equivalent circuit of this situation is shown in Figure 3.18 a).

26

Figure 3.18. Qualitative explanation of the connections in the full-wave conditioning depending on the capacity value of the TENG. a) equivalent circuit at the minimum value of C_{var}, b equivalent circuit at the minimum value of C_{var}.

In addition, when the TENG arrives at its minimum value of capacitance, diodes D1 and D3 switch on, turning to the situation described in Figure 3.18 b). Then, the TENG works as an AC voltage source, where its maximum amplitude is achieved when it arrives to C_{min} and its minimum value at C_{max}. In this way, the capacitor keeps the maximum voltage value that the TENG can provide to it, in the same way as a full-wave rectifier works.

The analysis made in reference [49] Chapter 11, reveals which is the maximum power and the optimal operation point for this circuit, using again the equations of the charge pump. Therefore, the energy added to the capacitor in a certain cycle is:

$$\Delta W_n = 2 V_{res_n}(C_{max} + C_{min}) \left[\frac{V_{offset}(C_{max} - C_{min})}{C_{max} + C_{min}} - V_{res_n} \right] \tag{3.41}$$

Calculating the first derivative of the expression, the optimal voltage operation point is:

$$V_{res}|_{opt} = \frac{1}{2} \frac{V_{offset}(C_{max} - C_{min})}{C_{max} - C_{min}} \tag{3.42}$$

At this operation point, the maximum energy per cycle is obtained:

$$\Delta W_{max} = \frac{1}{2} V_{offset}^2 C_{min} \left(\frac{C_{max}}{C_{min}} - 1 \right)^2 \frac{C_{min}}{C_{max} - C_{min}} \tag{3.43}$$

This kind of circuit is often used in the literature [50].

In order to compare half-wave and full-wave performance, The study carried out in reference [49], shows that half-wave conditioning provides higher power transmission in its optimal cycle than full-wave conditioning since:

$$\frac{\Delta W_{max}|_{HW}}{\Delta W_{max}|_{FW}} = \frac{1}{2}\left(\frac{C_{max}}{C_{min}} + 1\right) > 1 \qquad (3.44)$$

As trade-of, half-wave conditioning needs a slightly higher voltage operation point than full-wave. These results are tested in further sections of this chapter. Finally, Table 3.1 shows all the relevant expressions derived in this chapter.

Table 3.1. Compilations of important expressions.

Expression	Number
$C_{var} = \dfrac{2C_{max}}{1 + \dfrac{2C_{max} - C_{min}}{2C_{min}}(1 + \cos(\omega t))}$	(3.23)
$\|Z_{TENG}\| = \dfrac{1}{2\pi f C_{eq}}$	(3.26)
$V_{res}\|_{opt} = \dfrac{1}{2}V_{offset}\left(\dfrac{C_{max}}{C_{min}} - 1\right)$	(3.35)
$V_{res}\|_{opt} = \dfrac{1}{2}\dfrac{V_{offset}(C_{max} - C_{min})}{C_{max} - C_{min}}$	(3.42)

4. MEASUREMENT PLATFORM: DEVELOPMENT AND ASSESSMENT.

This section aims to show and assess the performance of the instrumental set-up developed for the characterization of TENGs nanogenerators. Note that the assembly, development, and settlement of this set-up is the first objective of the current Master Thesis project. Therefore, the present chapter should not be understood as a conventional experimental method section, but as the result of a continuous design and optimization process for the development and consolidation of a full characterization platform.

This set-up is adapted for the characterization of TENGs devices currently in development in the research group Nanotechnology on Surfaces and makes use of the instruments therein available. Thus, this chapter studies and assesses the performance and suitability of two modular platforms, that differ in the measurement instrument used to register the output voltage of the TENG devices. The first part of the chapter describes the general architecture and common features of both set-ups. Afterward, the present chapter analyses the performance of an initial set-up that makes use of the Keithley source measure unit (SMU) to analyze the signal generated by the TENG. Finally, a more cost-effective measurement approach that combines an oscilloscope and *ad hoc* signal-conditioning module is developed and analyzed in comparison with the original platform.

4.1 General description and common elements.

The common architecture of the developed and tested characterization set-up is described in Figure 4.1 whereas Figure 4.2 shows a picture of the system. This characterization platform consists of the following modules:

- *Electrodynamic shaker.* Mechanical excitation.
- *Signal generator* driving the mechanical shaker.
- *Force sensor.* Verification of the mechanical signal applied on the device under test.
- *The device under test* and holder.
- *Circuit board.* External load configuration and signal conditioning.
- *Measurement instrument.* Keithley source/electrometer or oscilloscope (see comments below).
- *Signal acquisition and processing systems.* PC unit and specific routines created for data collections and treatment.

The models and main characteristics of the instruments used in each module are presented in the next sections with a description of their function.

The following paragraphs describe very briefly the functions and operation of these modules.
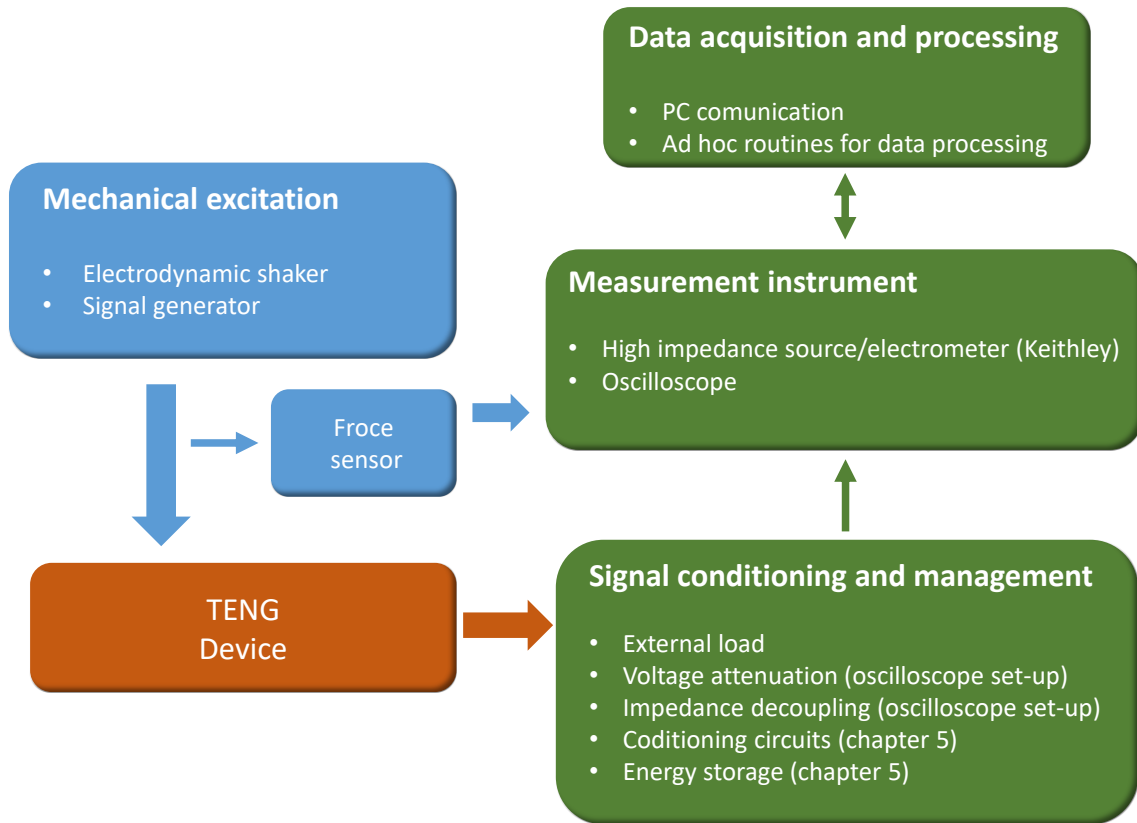
Figure 4.1. *The architecture of the developed characterization platform.*
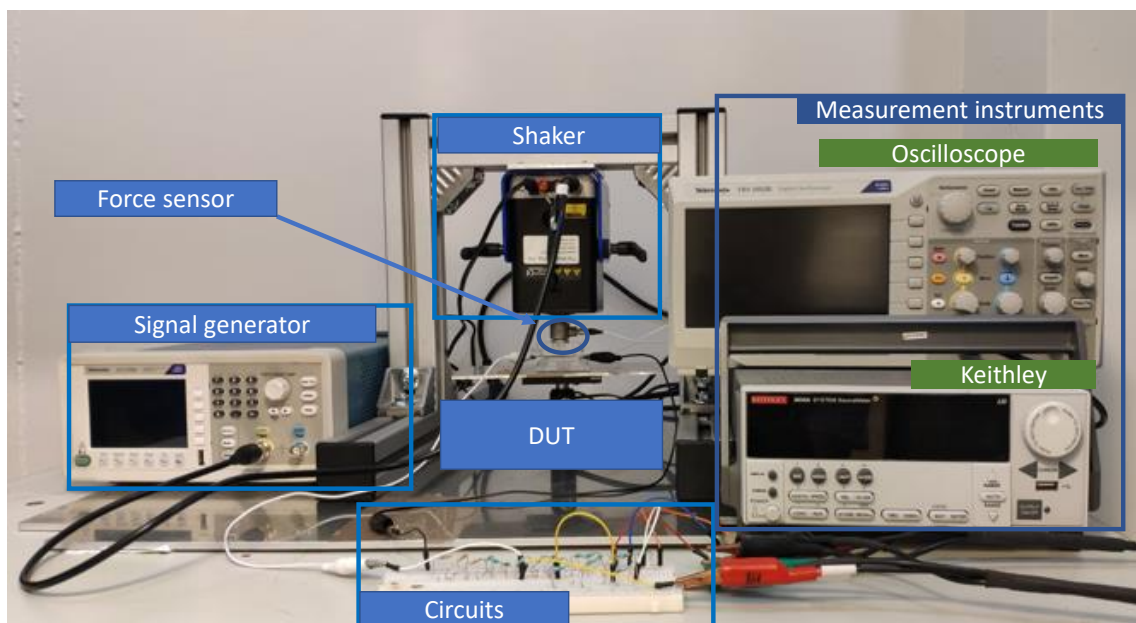
Figure 4.2. *Picture of the developed characterization platform.*

4.1.1 Electrodynamic shaker

The mechanical excitation is applied on the device under test by means of electromagnetic electrodynamic shaker or exciter, Model 2007 from Modal shop. This instrument makes use of a coil in combination with a magnetic rod to transduce an input electrical signal into a proportional force signal. Although the applied force is driven by the current flowing through the coil, the shaker is controlled by a voltage input thanks to the circuitry included in it. This provides a fixed relationship between the input voltage and the displacement and force output exerted by the shaker.

4.1.2 Signal generator

The input voltage signal controlling the shaker action is provided by a conventional voltage signal generator, model AFG1062 from Tektronix. For TENGs actuation, the common excitations are sinusoidal waves, instead of abrupt pulses signals. This is so because of two main reasons. The main one is related to the fact that instantaneous pulse interactions do not reflect the mechanical stimulus at which the TENGs are typically submitted in real scenarios. In addition, the shaker performance is better in the case of continuous waves than for abrupt pulse peaks. In this system, the frequency and amplitude of the sinusoidal voltage signal are adjusted to produce the required mechanical excitation. The latter is verified employing a force sensor interfaced with an oscilloscope.

4.1.3 Force sensor

The applied pressure is a key magnitude for mechanical nanogenerators operation. In the case of TENGs, this magnitude regulates the charge transfer between electrodes and therefore the surface charge induced at the triboelectric layer. Too low pressure entails poor charge transfer and therefore low performance; whereas high pressures may damage either the TENGs or the shaker itself. In the middle range, the charge transfer between electrodes is effective and a saturation regime, which depends on the triboelectric properties of the device, is reached. This is the desirable operation regime.

The relationship between the amplitude of the voltage input signal and the displacement and acceleration generated by the shaker in a load-free scenario is known. However, the actual pressure experienced by the TENG also depends on the distance between the natural position of the shaker to the bottom plate of the TENG, which is unknown. To control the actual pressure over the device, an integrated electronics piezoelectric sensor (IEPE model 1053V2 from Dytran Instrument, Inc.) is attached between the shaker and the triboelectric device. The IEPE force

sensor is powered by a current source power unit (Model 4110C from Dytran Instrument, Inc.) that also provides signal conditioning, DC offset. The latter usually interfaces with an oscilloscope to monitor the mechanical stimulus on the TENG.

4.1.4 Device under test

In order to evaluate the performance of the developed measurement platform, a reference TENG device is needed. Since this field is quite new, no reference samples are commercially available. Thus, a simple homemade device has been used as a reference. Reference samples should have a robust and an easy to reproduce architecture providing a reliable and intense triboelectric response. Otherwise, it is not possible to distinguish between problems related to the set-up from issues coming from the device. In this way, the used TENG device is based on the well-known triboelectric pair conformed by the polymer PFA (perfluoroalkoxy) and aluminium, top, and bottom electrode respectively. Besides the higher electron affinity in comparison with aluminium, PFA was selected due to the high capability to store the induced surface charge. The 50 μm thickness of this lamella is high enough to assure integrity when a standard force in the range between 1N and 3N is applied on the TENG. The architecture of the device under test is included in Figure 4.3. The bottom electrode consists of a lamella of PFA placed over an aluminium tape (bottom contact) whereas a single aluminium tape is used as the top electrode. Both electrodes are attached to plastic PMMA bases in order to guarantee mechanical stability. Note that for both electrodes the Al contacts are slightly shifted from each other to avoid possible contacts between them. The surface of the contact plate is 3x3 cm^2.
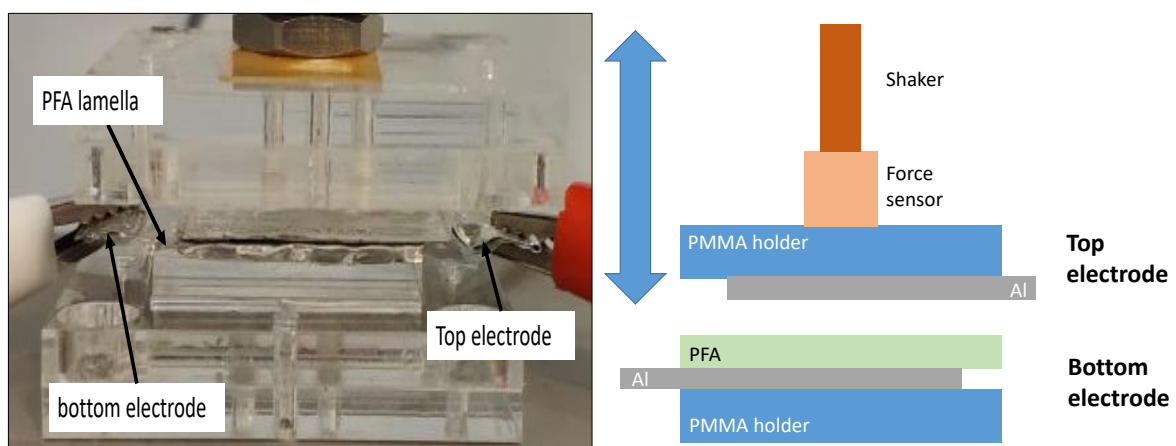
Figure 4.3. *Reference TENG sample used to study the performance of the set-up. a) Picture and b) schematic representation.*

4.1.4 Circuit breadboard

Once the mechanical stimulus is defined, the device´s electrodes are connected to a breadboard. In this board, the following operations can be defined depending on the test to perform and the used experimental set-up.

1. External load configuration (this chapter).
2. Voltage attenuation (this chapter, oscilloscope set-up section).
3. Impedance decoupling (this chapter, oscilloscope set-up section).
4. Conditioning circuits for efficient energy accumulation (Chapter 5).

4.1.5 Measurement instrument.

As it was discussed in the introduction section the output power in TENG devices strongly depends on the external load. Hence, one of the figures of merits usually analyzed for the characterization of TENG devices is the output-power vs load curve, which provides both the optimum load and the maximum output power of the device. One limitation for such analysis is related to the high internal impedance (Z_{TENG}) of TENG devices (10^6 to 10^9 Ohms), which in turn determines the load range for optimal operation. According to Jacobi's law [51], the nanogenerator power transfer is optimized when the external load equals the internal impedance of the source ($Z_{external} = Z_{TENG}$). However, for such high values, the actual external load of the TENG circuit can be easily distorted by the internal impedance of the measurement instrument.

When the instrument impedance is much lower than the set load the internal impedance of the measurement instrument is the one that determines the external load (see Figure 4.4) and therefore output power. Thus, the suitable characterization of TENGS devices under optimal load conditions (maximized output power) requires a high input-impedance reading instrument.

$$Z_{external} = Z_{set} \mathbin{//} Z_{instrument}$$

$$Z_{set} \gg Z_{instrument} \rightarrow Z_{external} \approx Z_{instrument}$$
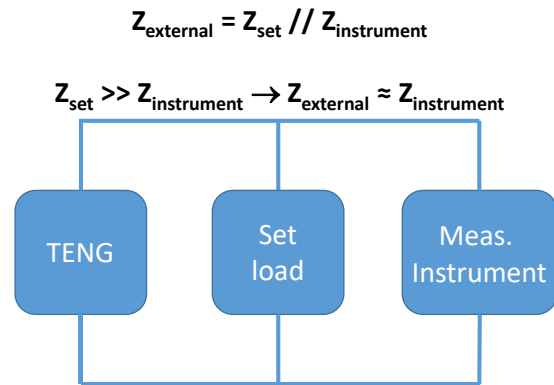
Figure 4.4. Basic measurement configuration.

Within the present master thesis, two different approaches to measure the out voltage of the TENGS are explored and comparatively assessed. The first one makes use of a high input impedance ($> 10^{14}\ \Omega$) source and electrometer, Keithley 2635A, to register the output voltage of the TENG. the second approach explores the advantages of replacing the Keithley 2635A with an inexpensive oscilloscope Tektronix TBS1052B (with an input impedance 1 MΩ) in combination with an impedance decoupling circuit. The following section discusses the mains characteristics

and limitations of both set-ups together with the performance during the characterization of the previously described test sample.

4.1.6 Signal acquisition and processing.

For the SMU-based set-up, communication with the PC unit is established utilizing a GPIB controller. For this project, a specific code (Test Script Builder) has been developed to set the acquisition parameters and data transfer to the PC.

In the case of the oscilloscope-based set-up, the communication between the instrument and the PC is made using a USB connection. A commercial software provided by Tektronix allows us to import the registered data from the oscilloscope and print it in a file. Hence, data can be easily processed using Origin Lab.

Data treatment and analysis are made with the software OriginLab. For such systematic tasks, specific templates and scripts have been designed in order to identify and process data automatically.

4.2 Source Measure Unit (Keithley) based set up.

4.2.1 Example of TENG characterization.

To assess the performance of the developed set-up for the characterization of TENG devices two basic tests have been conducted. The first one analyses the output voltage signal registered during TENG excitation, whereas the second test studies the background signal when no mechanical stimulus is applied. Both tests are conducted for different values of external load in order to assess its impact on the signal-to-noise ratio, as it is discussed before. A schematic of the circuit employed is shown in Figure 4.5, where R_{Load} is the applied resistance load, and V_{TENG} is the voltage across this load.
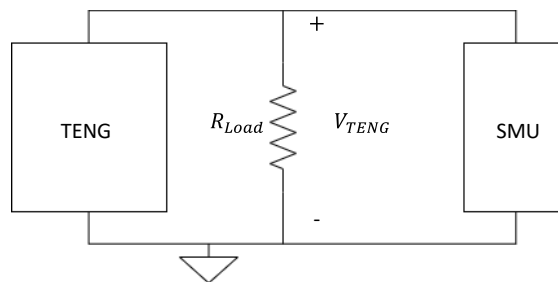
***Figure 4.5.*** *Diagram of the experimental TENG characterization circuit used in SMU-based set-up.*
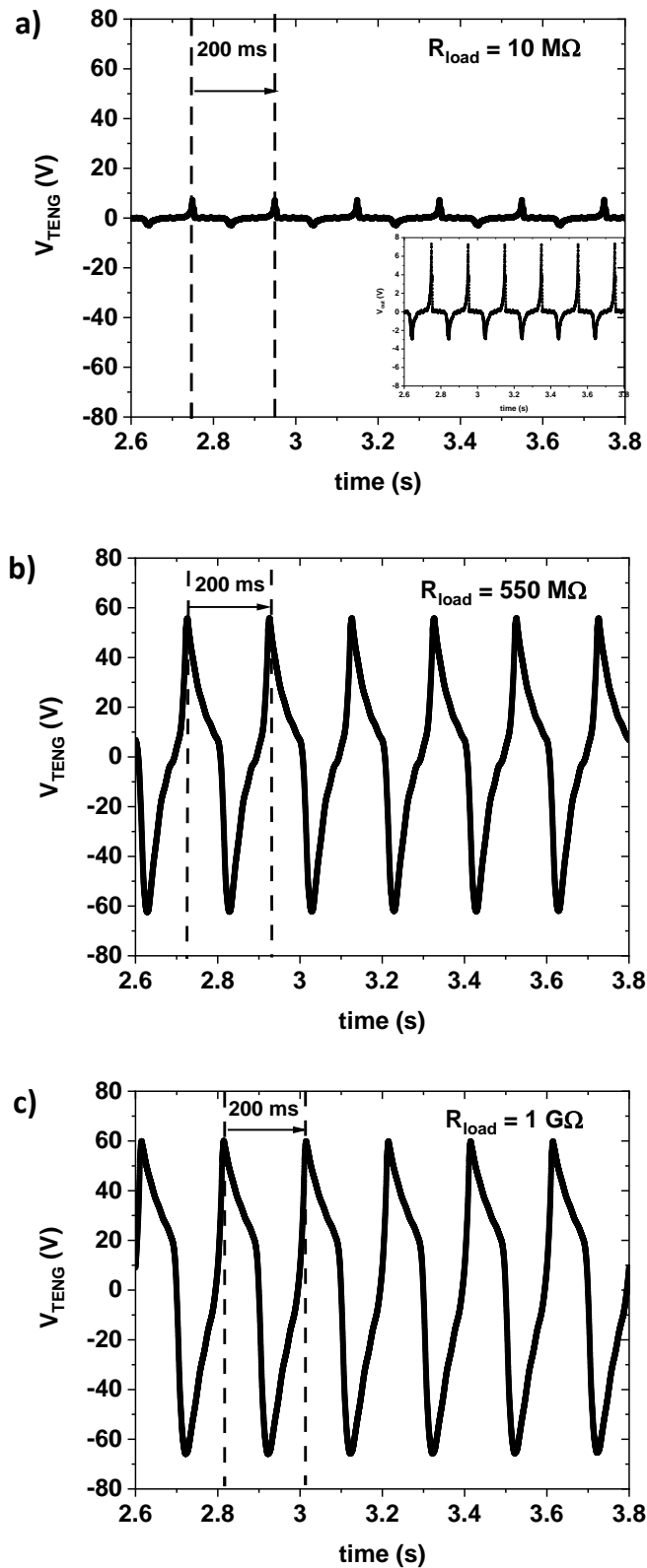
Figure 4.6. *SMU (Keithley) based set-up (c.f Figure 4.5). TENG output voltage signal registered for different R$_{load}$ as indicated in the figure. The inset in a) shows the shape of the V signal on an enlarged scale. TENG signal was excited with a sinusoidal stimulus of 5 Hz and 2N. SMU time resolution was set to 100 μs.*

Figure 4.6 shows the $V_{TENG}(t)$ signal acquired during normal TENG operation for three representative external loads that range from 10^7 to 10^9 Ω. These curves were registered for a mechanical stimulus of 5 Hz and 2 N of amplitude. The V_{TENG} (t) output describes a periodic signal that matches the frequency of the mechanical excitation. This supports the fact that the nanogenerator harvests and transduces the periodic mechanical stimulus into a usable electrical signal. Besides, the shape of the recorded V_{TENG} signal resembles those reported in the literature for other Mode I TENG devices [4], [52], [5]. In Figure 4.6 we can also recognize a slightly asymmetric profile characteristic of TENG devices. This profile changes with the used load as reported for other TENGS systems [45]. The good agreement of the registered curves with i) the theoretical behaviour and experimental results experimentally reported in the literature, as well as with ii) our owns simulations (see Chapter 6) confirms the suitable performance of the developed characterization set-up.
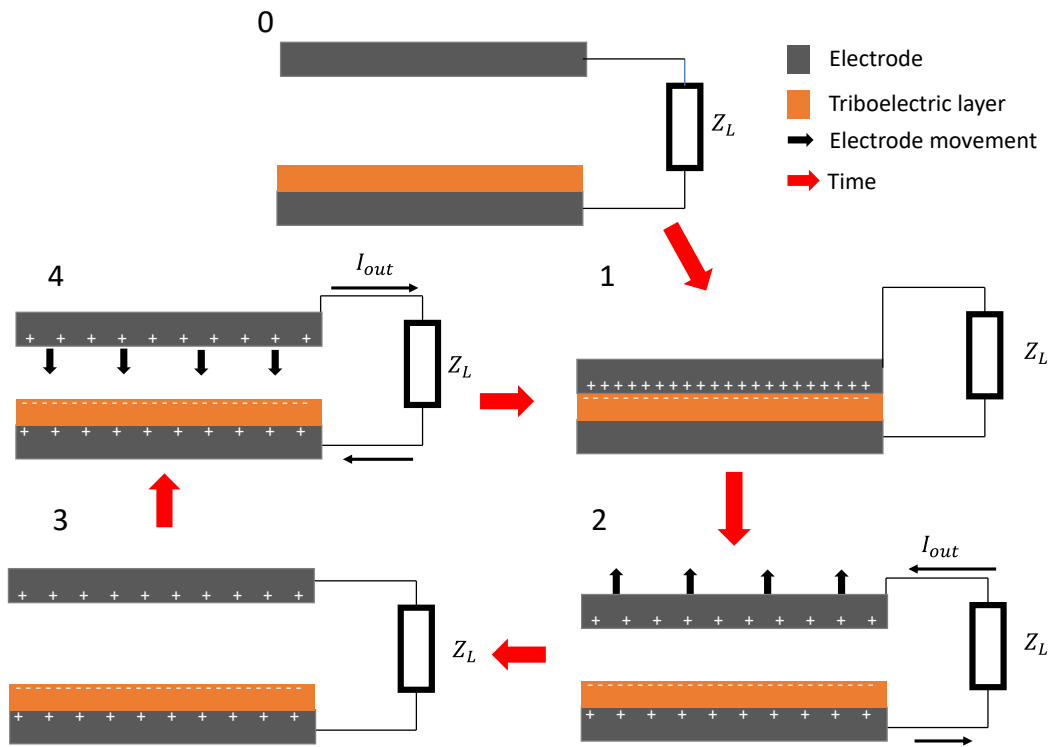
Figure 4.7. *Working mechanism of Mode I TENGs.*

The observed periodic and almost symmetric pattern observed in Figure 4.6 can be rationalized in accordance with the operation principle of Mode I TENG (see section 3.3.2). As it is indicated in Figure 4.7, due to the initial first contact a relatively high density of triboelectric charges accumulate on the surface of the dielectric layer. This local charge is compensated by the positive charge gained by the top electrode. However, when the contact breaks and the gap

between the electrodes increases the negative charges on the surface of the triboelectric layers need to be compensated. This generates a flow of electrons towards the top electrode that induces a positive charge density at the interface between the dielectric layer and the bottom metal electrodes. The flow of current, in turn, leads to a drop of potential through the external load. Once the gap between electrodes reaches the maximum values, the top electrode starts to approach the bottom electrode. This reverses the flow of current, now from the top electrode to the bottom electrode, to keep the electrostatic neutral state, until the initial condition is reached.

4.2.2 Noise characterization.

Our preliminary test (not included here) showed a significant distortion of the generated TENG signal. This was related to environmental electromagnetic noise exiting in our lab. This is a critical issue in the case of high impedance components, either the external load of the TENG devices itself [53], [54]. This issue was mitigated to a high extended thanks to suitable wiring, good ground definition, and the incorporation of ground planes both under the device and the breadboard. Nevertheless, a low voltage 50 Hz noise associated with the electrical grid is still detected. To illustrate this point Figure 4.8 gathers a noise study carried out for different loads. For this analysis, the TENG device was connected to the characterization set-up but (Figure 4.1 and Figure 4.5) no mechanical stress was applied on the DUT. Under these conditions, the TENG just acts as a capacitor as the gap between TENG electrodes remains constant (see section 3.3.3). In this set of graphs, it is very clear that the background signal is dominated by a characteristic AC noise at 50 Hz. In this optimized set-up the noise level reaches a maximum value of 0.6 V in the case of the higher load of 1 GΩ. Note that this AC noise can be easily eliminated by increasing the integration time during the measurement, *i.e.* the number of power line cycles (NPLC Keithley option). However, this dramatically affects the time resolution and compromises the detection and suitable resolution of narrow peaks such as those in Figure 4.6 a) with an FWHM ≈ 7 ms. On the other hand, for our standard sample, the output voltage in the case of a high impedance circuit reaches 60 V. This is approximately two orders of magnitude higher than the worst noise signal in Figure 4.8, registered using a time resolution of 0.1 ms. Thus, this level of noise is acceptable for the basic characterization of this kind of TENG device. Nevertheless, this is a point to improve in further developments.
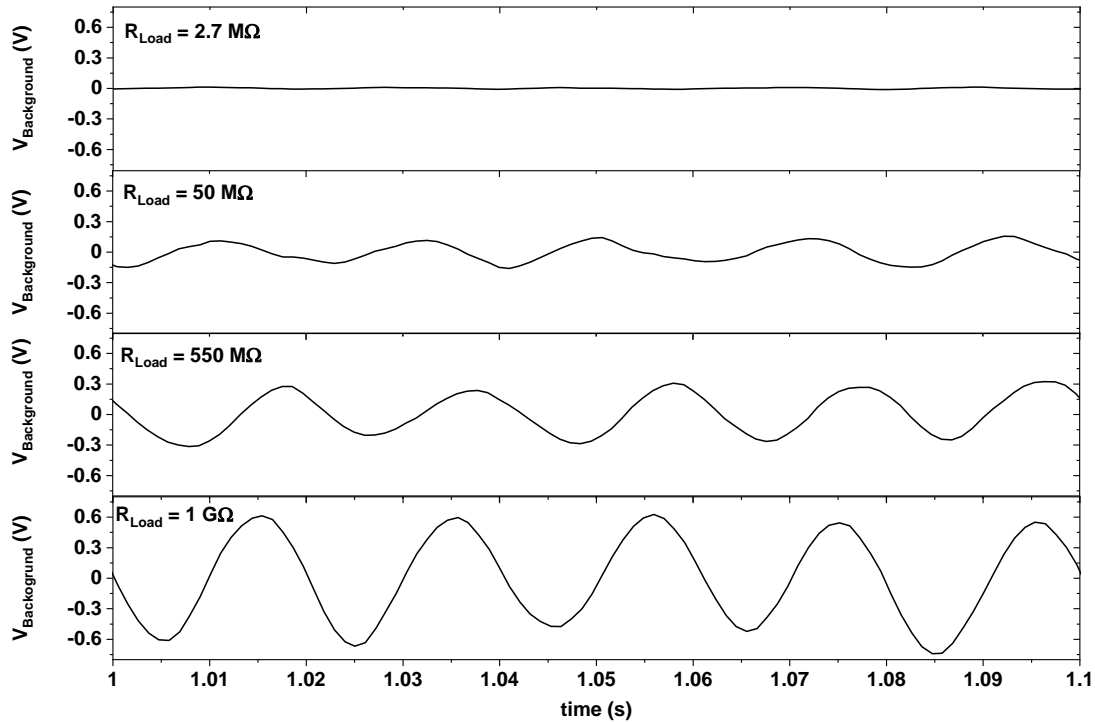
Figure 4.8. *SMU-based set-up (cf. Figure 4.5). Noise study for different loads as indicated in the figure. Integration time was set to 100 μs. The tests were conducted for a TENG device without mechanical stimulus and for different loads as it is indicated in the figure.*

4.2.3 Other considerations.

The data presented above show the suitable performance of the SMU (Keithley) based set-up for the basic characterization of TENG devices. However, there is a practical consideration to take into account when assessing the suitability of this set-up.

First of all, the used SMU instrument does not provide a real-time view of the signal generated by the DUT. Instead, V(t) curves are recorded and stored in the internal buffers for a given period of time, and afterwards transferred to the PC for plotting. The lack of real-time monitoring is a time-consuming and inconvenient disadvantage in the case of optimization and other verification processes such as sample alignment, initial surface charging, signal conditioning, or noise suppression. Besides, it could be a source of mistakes for inexperienced users.

In addition, the used 2635 model has a single measurement channel. Thus, in the case of our characterization platform, an additional instrument is used to simultaneously monitor the force signal.

4.3 Oscilloscope-based set-up.

The used Keithley source-meter provides a high input impedance. This is a critical requirement for this kind of test in which a high external load is required to maximize the $V_{TENG}(t)$ signal (more details in section 4.1.5). However, the used SMU instrument has some practical limitations and inconveniences, as was discussed at the end of the previous section. Another critical point is related to the high price of this kind of high impedance instrument. Thus, the current section analyses a different approach based on inexpensive oscilloscopes interfaced with a signal conditioning unit for impedance decoupling and signal attenuation. The selection of this kind of measurement instrument is supported by the following advantages
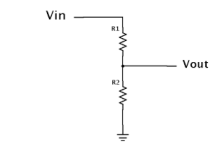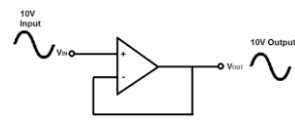
1. Cost efficiency.
2. Real-time monitoring.
3. Simultaneous two-channel operation (one channel for the TENG signal, and one for force sensor monitoring).
4. Friendly acquisition parameters configuration even for inexperienced users (students).
5. Straight USB communication to PC.

4.3.1 Limitations and implemented solutions.

Despite the advantages listed above, the available TBS1052B oscilloscope has some limitations for the characterization of TENG devices. They are related to:

- The high output voltage of the TENGS devices.
- The high value of the optimal load is used to maximize the output power of the system.
- Noise management.

In particular, the open-circuit voltage of conventional Mode I TENG devices is typically in the range of several tens to a few hundred volts. This rage is much higher than the upper limit of our instrument (20 V). On the other hand, as it was discussed in section 4.1.5, the identification of the optimum load that maximizes the output power requires an instrument with an input impedance, much higher than the internal impedance of the nanogenerator. However internal impedance of TENG devices typically ranges from 10^6 to 10^9 Ω whereas the input impedance of our oscilloscope is 10^6 Ω (10^7 Ω when the system is equipped with a TPP0054 Voltage Probe). These and issues can be solved thanks to suitable signal conditioning and data treatment. Figure 4.9 illustrates the different approaches implemented during the optimization process of the characterization platform to cope with these limitations.

Principal problems	Solution
High TENG output voltage	**Signal attenuation** Voltage divider
Oscilloscope input impedance < **Optimal external load**	**Impedance decoupling** Voltage follower

Figure 4.9. *Oscilloscope-based set-up. Limitations and implemented solutions.*

4.3.2 Signal conditioning.

The first issue to address is the high output voltage of TENGs. This normally overpasses the operational limit of both i) the used oscilloscope and ii) other elements of the conditioning circuit described in this section (e.g. the buffer voltage discussed before). To cope with this situation, we take advantage of the external load used to optimize the power transfer. As indicated in Figure 4.10 the external load is split into two resistors which forms a voltage divider. In this way, just a fraction of the output voltage is transferred to the rest of the circuit through node 1. The actual out voltage of the TENG and all the data presented in this document are calculated considering the voltage in node 1 and the attenuation factor $R_2/(R1+R2)$.

The second problem to address is the impedance mismatch between the TENG source and the oscilloscope. To solve this issue a voltage buffer, an operational amplifier (op-amp 445) with negative feedback, is implemented into the system to decouple the impedance of the oscilloscope from the rest of the circuit. This model of op-amp has been chosen due to its high reliability and its low noise susceptibility. This approach allows us to reproduce the TENG output voltage of the positive node 1 into the input probe of the oscilloscope without disturbing the actual load of the TENG circuit.

In this system, the buffer is powered through an AC/DC converter of $\Delta V = 39$ V. The ground level within this range is defined by the top voltage divider (resistors $R_+ = R_-$). In this way that the linear range of the op-amp is defined within the range $V_{SS} = -19.5$ V to $V_{DD} = 19.5$ V. Due to the simplicity of the proposed impedance-decoupling approach no previous simulation was conducted in this stage. Instead, the system configuration was experimentally optimized as is indicated below.

At this it is important to remark this signal condition approach herein discussed is specifically devised for the characterisation of high impedance TENG using the oscilloscope based set-up. The current chapter exclusively focused on the characterization of single TENGs. Thus the combined voltage-divider and follower based approach (Figure 4.10) is only used to allow the characterization of loaded TENG systems with low impedance systems, such as the used oscilloscope. This section should not be confused with the conditioning circuits discussed in Chapter 5, which are devoted to improve the power transmission to power management units.
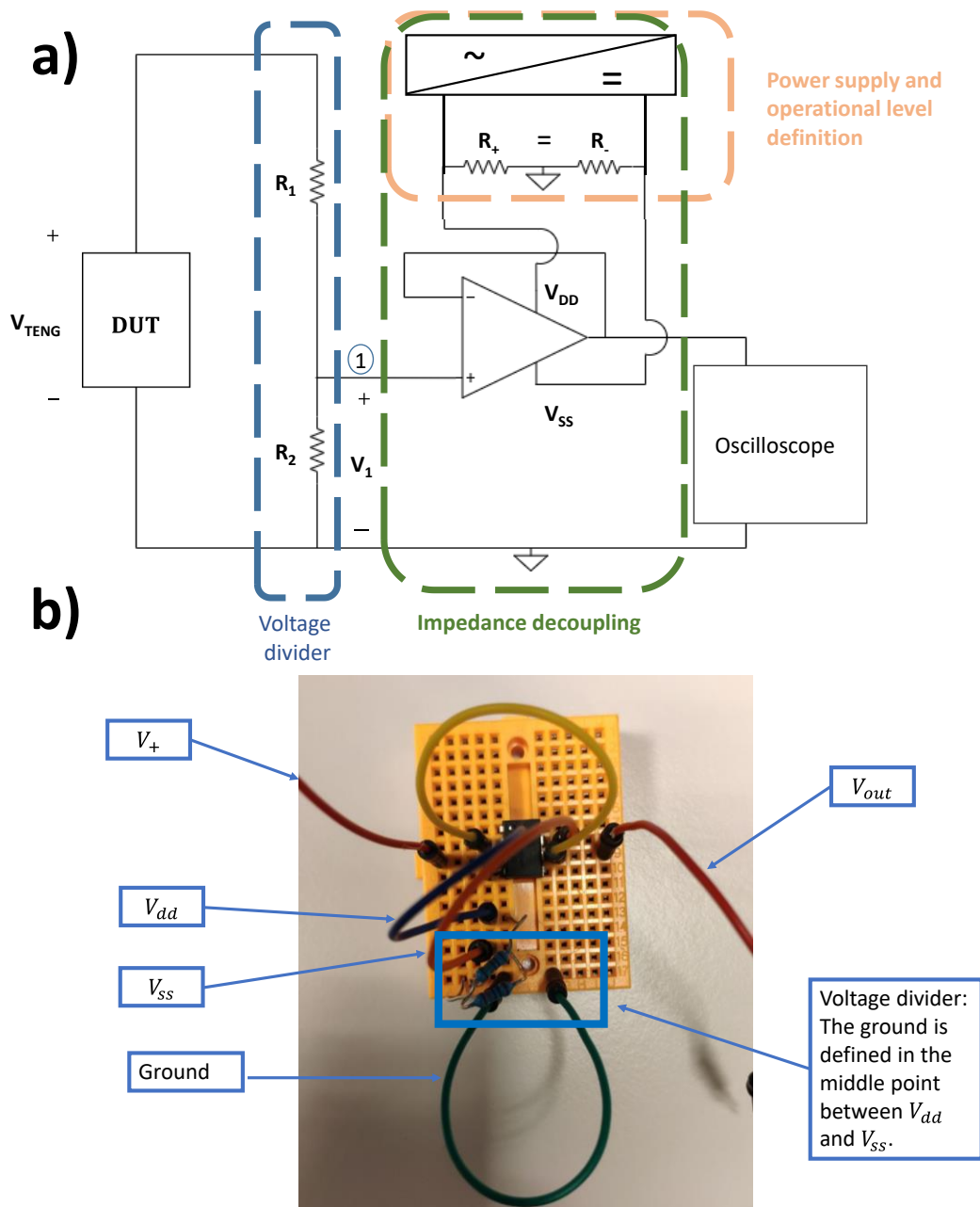

Figure 4.10. *Oscilloscope-based set-up. a) Schematic and b) picture of the signal conditioning protoboard.*

4.3.3 Signal noise reduction.

As it was indicated before, an op-amp-based voltage follower is used to decouple the low input impedance of the oscilloscope from the TENG circuit. To do so the power supply of the op-amp is stated at the widest allowed voltage since it determines the linear region of the amplifier (from -19.5 V to 19.5 V in this case). Such high voltages require using high-value resistors to define the ground of the power supply circuit. Otherwise, a high current would flow through resistors R_+ and R_- in Figure 4.10 leading to undesirable overheating. However, the higher is the resistance of these resistors the higher is the noise coupled into the system. This becomes an important issue as the AC/DC converter acts as an additional source of noise. Therefore, the value $R_+ = R_-$ must be very carefully selected to maintain the electrical noise low level without compromising the thermal integrity. Due to the simplicity of the circuit, experimental optimization was preferred over simulation. This optimization step is illustrated in Figure 4.11.
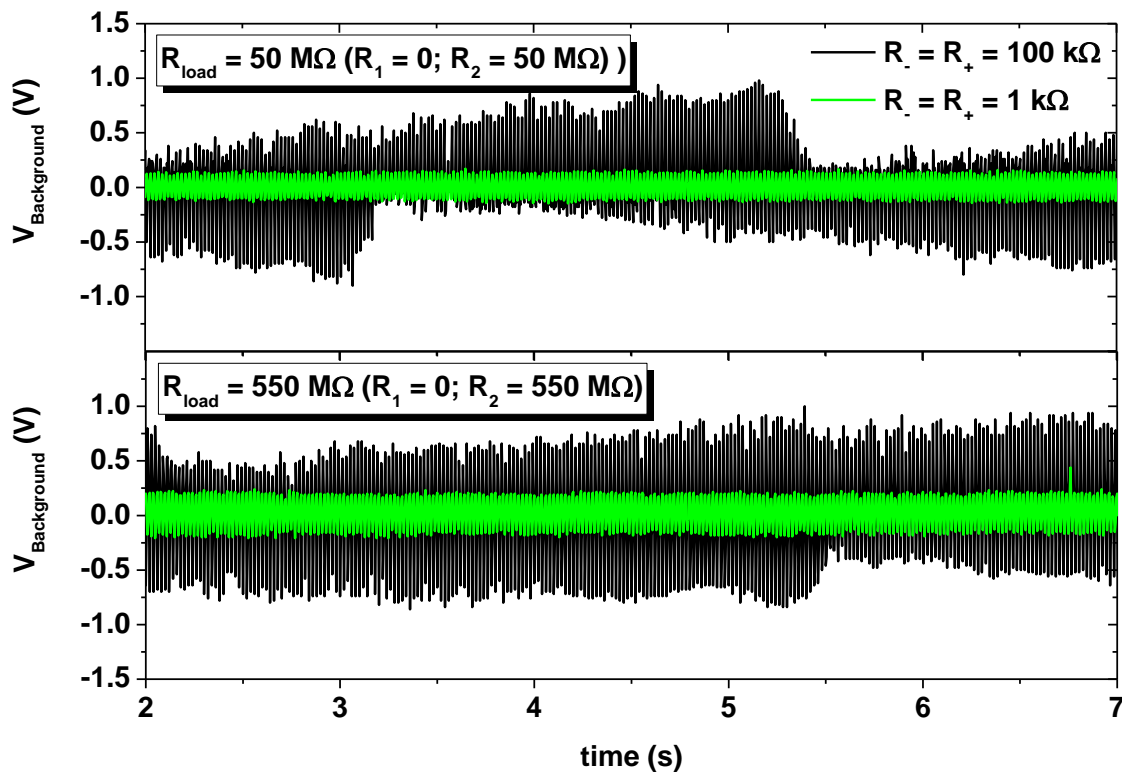
Figures 4.11. *Oscilloscope set-up (c.f. Figure 4.10). Noise study. Output background signal registered for different values of the resistors used for ground definition at the op-amp power supply ($R_- = R_+$ in Figure 4.10). Black curves: high resistance ($R_- = R_+ = 100\ k\Omega$). Green curves: medium resistance ($R_- = R_+ = 1\ k\Omega$). The tests were conducted for a TENG device without mechanical stimulus and for two values of load resistance as it is indicated in the figure.*

Figure 4.11 compares the noise level registered at the output of the signal conditioning circuit ($V_{oscilloscope}$ in Figure 4.10) when using 1 kΩ and 100 kΩ resistors for the definition of the ground level ($R_- = R_+$ in Figure 4.10). The selection of 1 kΩ resistors was supported by the fact that no anomalous heating or thermally associated instabilities were observed. These noise tests were conducted without signal attenuation ($R_1 = 0$), and for two values of the TENG loads (R_2) to compare the impact of these resistors. Comparison of the different background profiles clearly shows that resistors R_- and R_+ have a high impact on the noise. In fact, for $R_-=R_+= 100$kΩ the noise always describes a very unstable profile (black curves in Figure 4.11) that reach values > 1 V, whereas a very uniform background < 0.2 is observed when reducing R- and R+ to 1 kΩ. In addition Figure 4.12 also shows clearly the strong effect of these resistors on the quality of the signal registered with this set-up. In this test, the TENG device is excited with a 5 Hz signal. In the figure, we can recognize the V(t) curves reported in 4.6 for the SMU Keitherly-based set-up. In this figure the signal acquired for R- = R_+ = 1 KΩ described a clean profile that contrasts with the low quality of the R- = R_+ 100 kΩ signals. All this together with the lack of signs of thermal degradation supports the use of 1 kΩ resistors to define the linear range of the op-amp. Lower resistors were also tested but the reached temperature due to the Joule effect was not acceptable.
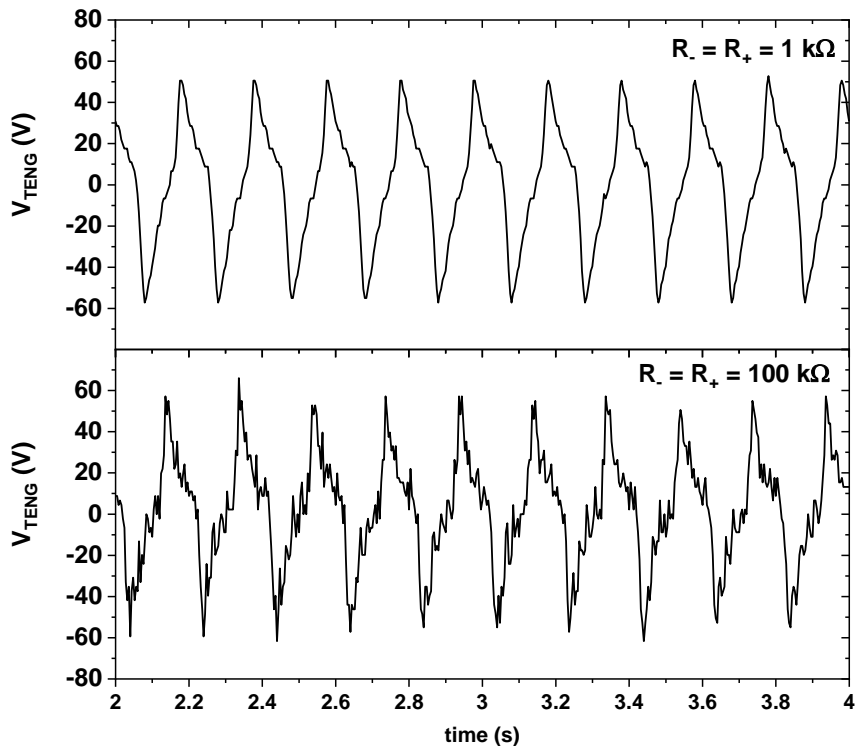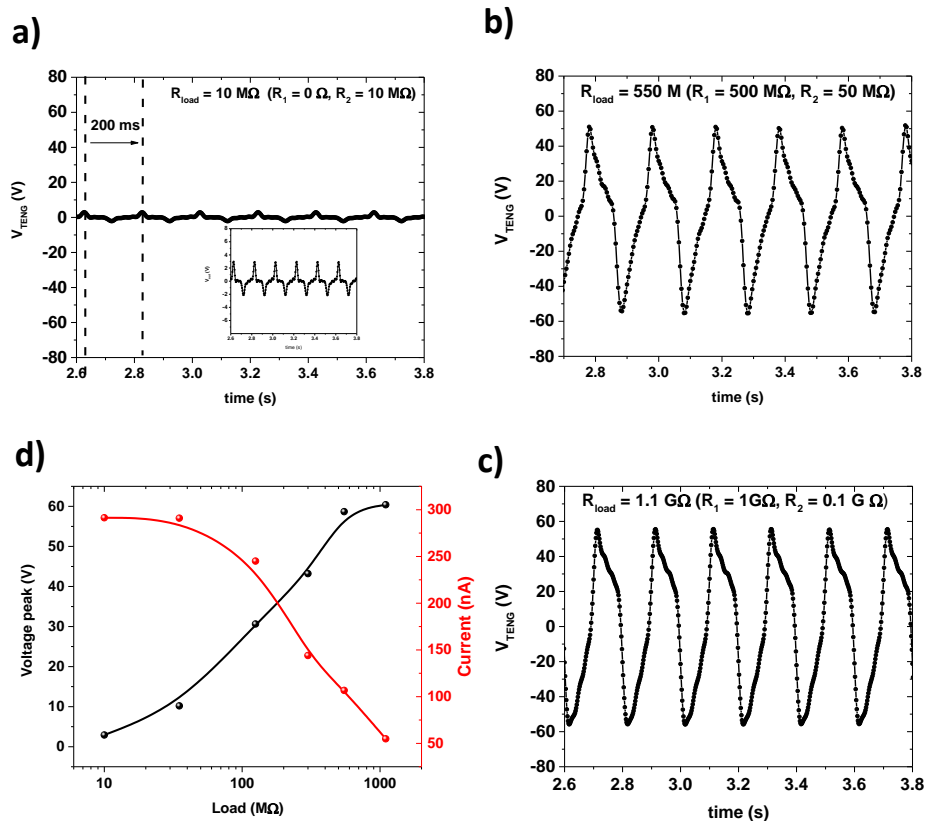

Figures 4.12. *Oscilloscope set-up (c.f. Figure 4.10). Noise study. Signal quality registered for different values of the resistors used for ground definition at the op-amp power supply ($R_- = R_+$ in Figure 4.10). Both graphs were acquired for a TEGN excited with a 5 Hz signal a load of 550 MΩ (R_1= 500 MΩ and R_2 = 50MΩ).*

4.3.4 TENG characterization.

After the optimization process described above this section shows the V(t) signal registered by oscilloscope-based set-up. For the shake of comparison with the SMU (Keithley) based platform, we performed the same tests as in section 4.2.1. Thus, Figure 4.13 a) to c) analyses the V(t) signal acquired during normal TENG operation for three representative external loads that range from 10^7 to 10^9 Ω. These curves were registered for the mechanical stimulus of 5 Hz and 2 N of amplitude. The generated signals are similar to those reported in Figure 4.6. They describe a periodic pattern with the periodicity of the mechanical excitation. In this figure, the shape of the V peak depicts the same evolution as in Figure 4.6. In fact, for each load, the $V_{TENG}(t)$ peaks resemble those reported in Figure 4.6. Nevertheless, $V_{TENG}(t)$ peaks in Figure 4.13 are slightly lower than the counterparts in Figure 4.6. Similar differences are observed when reproducing these same tests and they are tentatively ascribed to the initial surface charge and inhomogeneities at the surface morphology.

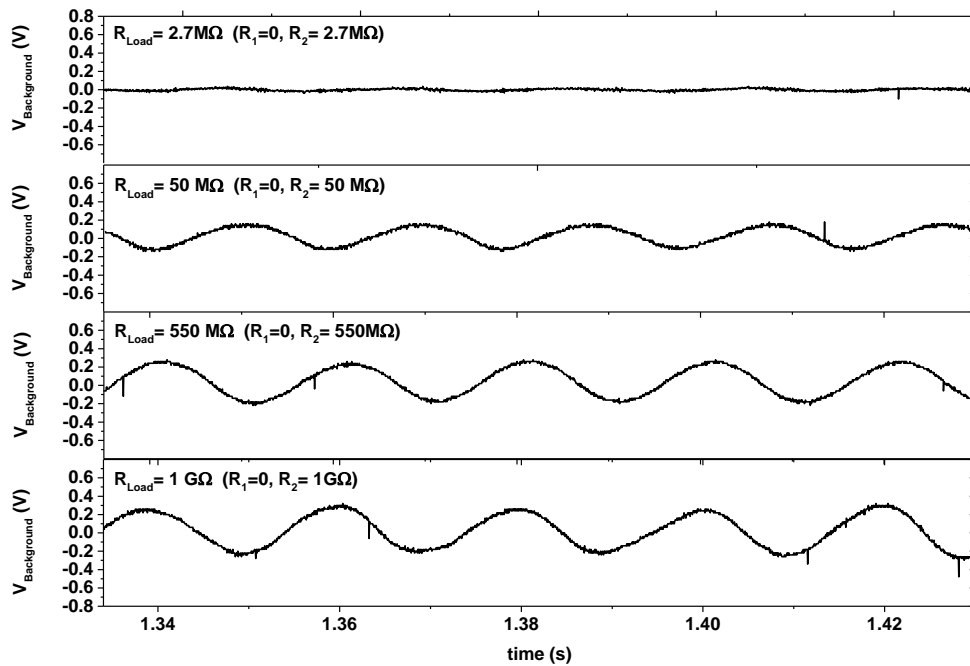***Figure 4.13.*** *Oscilloscope-based set-up (c.f. Figure 4.10). a) to c) TENG output voltage signal registered for different R_{load} as indicated in the figure. The inset in a) shows the shape of the V signal on an enlarged scale. TENG signal was excited with a sinusoidal stimulus of 5 Hz and 2N. d) Shows the V and I peak intensity as a function of the load. Current values were calculated from the output voltage and the used load.*

As it was discussed in section 4.2.1, the peak intensity increases with the load. This is better illustrated in figure 4.13 d), which shows the evolution of both V and I peak intensity as a function of the load. In these graphs, the current is calculated by dividing the output voltage by the load. The figure describes the typical behaviour reported for this kind of device [41], [52]. Thus, the generated voltage increases with the external load until a plateau is reached. The opposite trend is observed in the case of the generated current, which vanishes in the case of the highest loads. The good agreement of the registered curves with i) our experimental results acquired with the SMU based set-up, i) the behaviour reported in the literature, as well as ii) our owns simulations (see Chapter 6) confirms the suitable performance of the developed characterization set-up.

4.3.5 Comparative noise characterization.

A noise study has been performed in the same way as it has been made for the Keithley SMU set-up. Figure 4.14 shows the registered noises at different loads. As it was reported for the Keithley SMU-based set-up (4.7), the characteristic 50 Hz AC noise is observed. Both set-ups, oscilloscope (Figure 4.14) and SMU (Figure 4.8) show similar noise levels. However, the oscilloscope-based set-up presents a little bit stronger white noise than its counterpart. This increase in white noise is very weak, being completely neglectable. Therefore, oscilloscope-based set-up can provide the same quality levels as SMU based set-up, guarantying a high-quality SNR.

Figure 4.14. Oscilloscope-based set-up (c.f. Figure 4.10). Noise study for different loads as indicated in the figure. The time resolution is 40 μs. The tests were conducted for a TENG device without mechanical stimulus and for different loads as it is indicated in the figure.

In conclusion for this section, it has been proved that oscilloscope set-up provides a signal of the same quality as the more expensive and less convenient SMU based set-up. This is supported by the data provided in sections 4.3.4 and 4.3.5 and the discussion in section 4.2.3 and at the beginning of section 4.3, Therefore, the oscilloscope set-up is used for the rest of the master thesis project.

4.4 Study of TENG power transmission

Once the set-up performance has been defined (oscilloscope-based set-up), this section completes the characterization of the TENG response by analyzing the transmitted power as a function of the external load and frequency of the mechanical stimulus.

Figure 4.15 shows the output voltage signal generated by a stander TENG when excited at 5 Hz and 50 Hz for different representative loads. There, it can be seen that for the same load, higher frequencies lead to a more intense voltage response, which perfectly agrees with the expected behaviour as discussed in the simulation chapter. Knowing the voltage and the applied load, the instantaneous power is calculated using Ohm's law. From these data, the average power is calculated. Figure 4.16 shows the dependence between the transmitted average power and the external load for the two frequencies herein studied. At low values loads the average power increase with the load until the optimal load condition is reached ($Z_{opt} = Z_{TENG}$). After this point, an increase of the load leads to a decrease in the average power, vanishing for high enough loads. The data in this graph show how the average output power strongly depends on the excitation frequency. In fact, the maximum power average at 50 Hz is approximately one order of magnitude higher than the maximum power registered in the 5 Hz case. In addition, we can also recognize a shift of the optimal load to lower values when the excitation frequency is increased. As it is discussed in Chapter 3 (sections 3.3.4 to 3.3.6), TENG impedance can be modelled as a capacitor whose impedance is inversely proportional to the excitation frequency. Therefore, this displacement of the power maximum is explained by expression (3.26) which is used to approximate the internal impedance of Mode I TENG and the $Z_{Load} = Z_{TENG}$ condition. Table 4.1 shows the optimum load for the two analyzed frequencies. There we can see how increasing the excitation frequency by one of magnitude reduces the optimal load by a factor of 10, as expected in agreement with equation 4.1 and Jacobi's law.
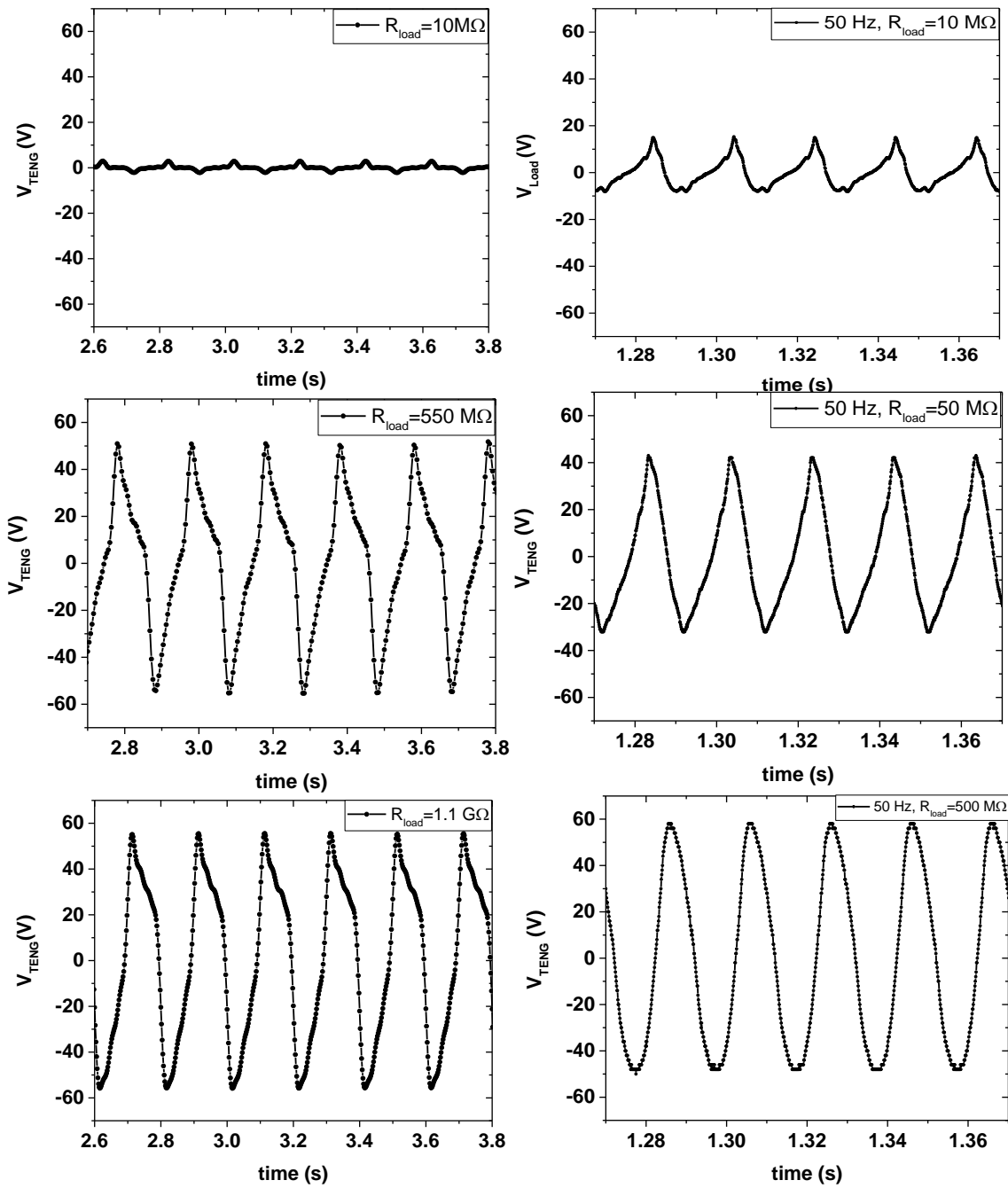
Figure 4.15. TENG output voltage excited at 5 Hz and 50 Hz for different loads. Oscilloscope based set-up (c.f Figure 4.10).
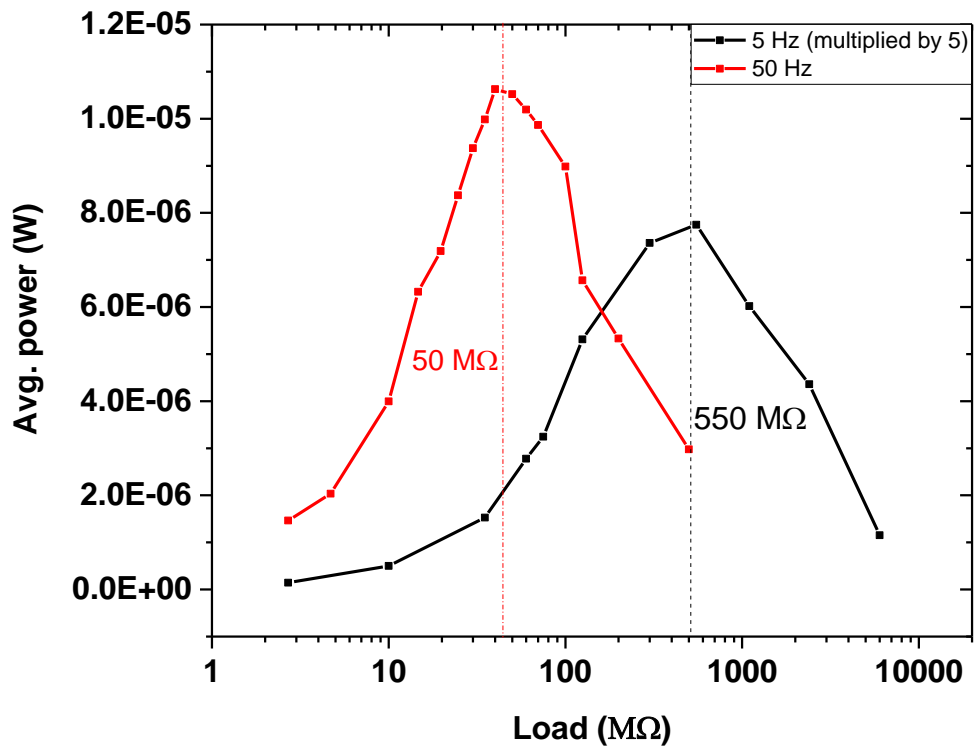
Figure 4.16. Average transmitted power vs load for two excitation frequencies. Oscilloscope based set-up (c.f Figure 4.10).

Table 4.1. Optimal load for the used excitation frequency. Data inferred from Figure 4.16.

Frequency (Hz)	Optimal load (MΩ)
5	550
50	50

5. CONDITIONING CIRCUITS RESULTS

This chapter discusses the implementation of two types of conditioning circuits for the suitable integration of TENGs devices into functional systems. First, the experimental methods are discussed. Afterwards, the performance of two types of conditioning circuits, half-wave and full-wave systems, are experimentally analysed. A detailed explanation work principle of both systems can be found in section 1.4.

5.1 General experimental method

The implemented conditioning units are half-wave and full-wave conditioning circuits. Both of them belong to the group of rectangular Q-V cycle conditioning circuits. A deeper insight into the working principle and fundamentals of these systems can be found in Chapter 1, section 1.4. The present section shows the experimental design for the full-wave and half-wave conditioning circuits. They both have been fabricated on the same board (Figure 5.1), where the full-wave circuit is on the left, while the half-wave circuit is placed on the right.
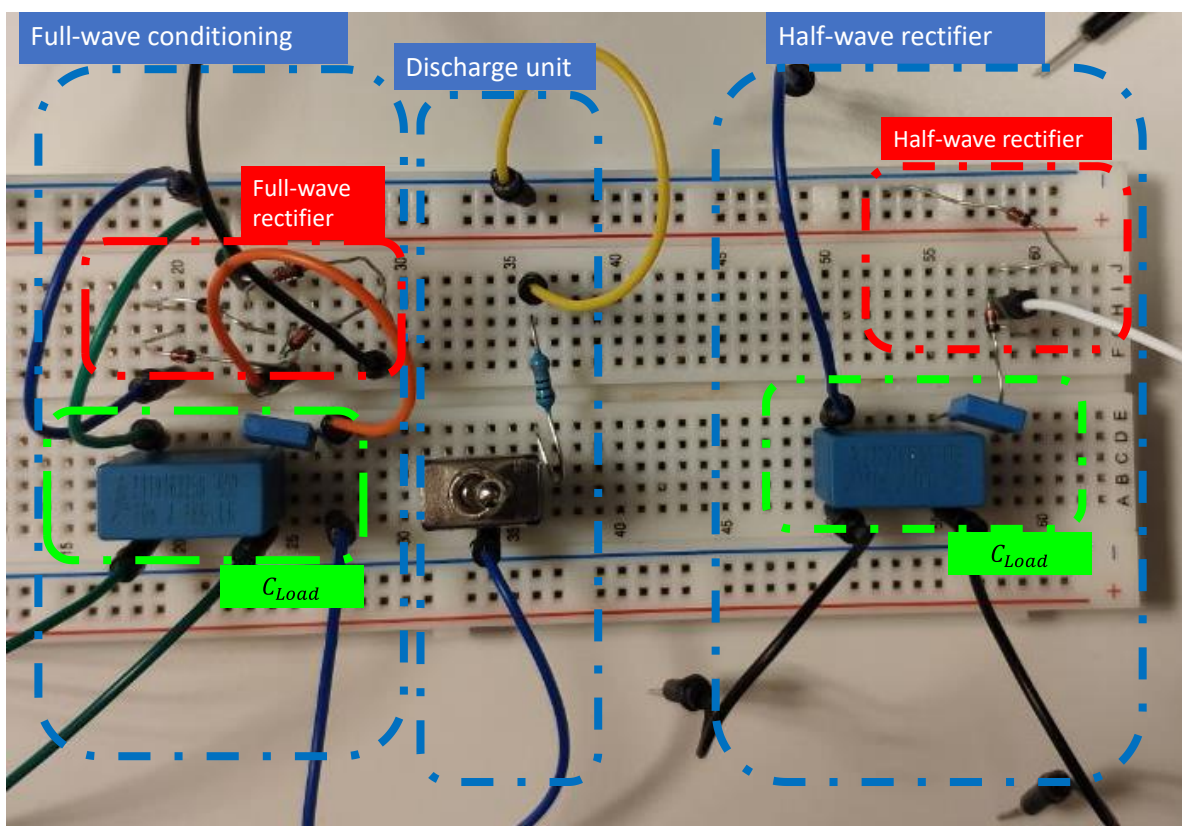
Figure 5.1. *Conditioning circuits. On the left of the board, the full-wave rectifier is placed. The half-wave rectifier is on the right, while in the middle of the board the discharge circuit is set.*

In this section, the experimental designed created for full-wave and half-wave conditioning circuits is discussed. These circuits are shown in In Figure 5.1. They both have been placed on the same board together with a discharge circuit. The next section discusses all these units.

5.1.1 The discharge circuits

According to Figure 5.1. A resistor connected to a switch has been placed in the middle of both circuits. Its function is to discharge the load capacitor of the circuit in use between measurements. The value of the used resistor is 100 KΩ.

5.1.2 Implementation of the voltage divider

The expected output voltages are in the order of tens of volts, being usually higher than the 20 V limitation of our oscilloscope. Therefore, both circuits use a voltage divider. As illustrated in Figure 5..1 the load capacitor is divided into two capacitors in series: C_{res} (little blue capacitor) and C_{med} (big blue capacitor). C_{med} is 10 nF, while C_{res} is 1 nF, forming an equivalent capacitor C_{load} of 0.9 nF. Then, the oscilloscope is set to read the voltage across C_{med}. Note that the voltage in C_{res} is always bigger than in C_{med} keeping the oscilloscope out of risk. Then, the total voltage across the equivalent C_{load} capacitor is the following.

$$V_{load} = \left(\frac{C_{med}}{C_{res}} + 1\right) V_{med} = 11 \cdot V_{med} \tag{5.1}$$

being V_{med} the voltage across C_{med} and V_{load} the voltage across the total load. These calculations are set in an Origin template, automatizing data treatment.

5.1.3 TENG sample and Diodes specifications

BAS45A low-leakage diodes (fabricated by Nexperia) are used in these circuits. They have a forward voltage of 0.6 V with a maximum reverse current of 1 nA.

The sample used is the same as the previous chapter. The top electrode is a sheet of aluminium with a PFA layer on it, while the bottom electrode is a single layer of aluminium. The used force is 2 N. The working frequencies of this study are 5 Hz and 50 Hz.

5.1.4 Measurement procedure

First, the discharge circuit is activated to discharge the voltage accumulated in the previous experiment. Then, after some seconds the discharge circuit is turned off. From this moment, the noise starts to charge the capacitors up to a saturation level. This voltage defines the background level of the experiment. When this value gets stable, the shaker is activated, and the device starts to pump charge into the load capacitor and the resulting V(t) curve is registered.
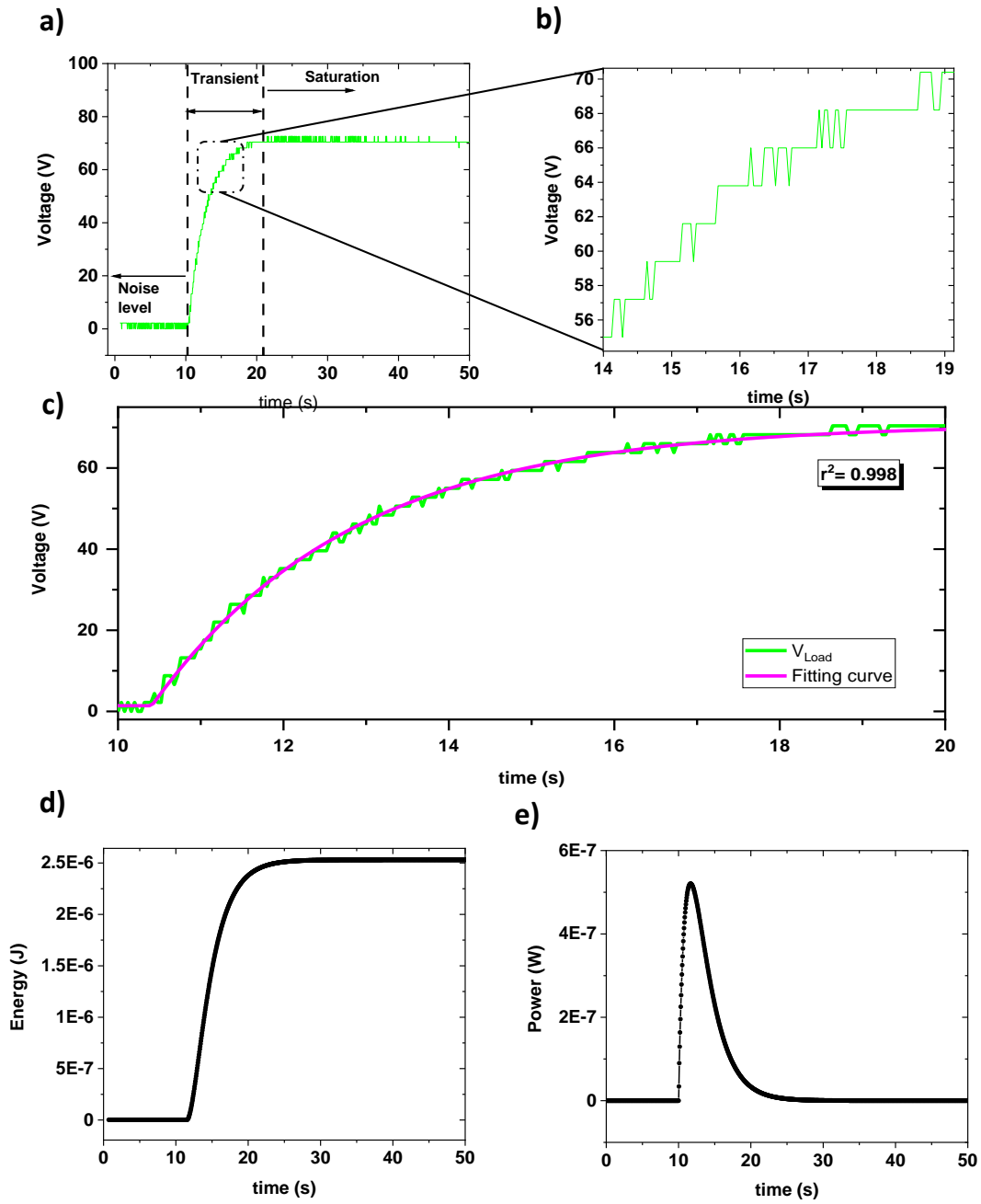
5.1.5 Data processing

First, the voltage measurements need to be corrected using expression 5.1. The resulting graph displays a charging curve such as the one in Figure 5.2 a) for a half-wave conditioning measurement, excited at 5 Hz. A closer look at the transient state reveals a step-like profile (Figure 5.2 b) which is ascribed to the discrete pulse of charge that feeds the capacitors. Unfortunately, this distorts the data-processing procedure used to approximate power, since this is based on the first derivative of the V signal. To solve this issue the generated V curves are fitted as follows. Considering the circuit architecture an RC type behaviour is expected. Hence, the following expression 5.2 is proposed for fitting.

$$V_{load}(t) = \begin{cases} V_{Load}(t = 0) & if \ t < t_0 \\ V_{Load}(t = 0) + V_{sat}\left(1 - e^{\frac{t-t_0}{\tau}}\right) & if \ t > t_0 \end{cases} \tag{5.2}$$

Where V_{load} is the voltage across the load capacitor, t_0 is the time when the shaker is activated, $V_{Load}(t=0) + V_{sat}$ is the voltage at which the circuit saturates and τ is the characteristic time constant of the system. The goodness of the proposed fitting scheme is illustrated in Figure 5.2 c), which compares the experimental data and the fitting function during the transient state. This is also supported by the r^2 value included in this figure and those reported in Table 5.1, Table 5.2, Table 5.4 and Table 5.5. Using the voltage fitting curve, the energy stored in the load is calculated as a function of time (Figure 5.2 d). Finally, the transmitted power (Figure 5.2 e) is calculated as the first derivative of the energy function.

Figure 5.2. *Data processing. a) Corrected voltage registered at C_{load}. b) Enlarged view showing the step-like shape of the registered curve. c) Fitting process. d) Energy curves calculated from the fitted function. e) Power curve calculated from the fitted curve. Used data corresponds to a half-wave conditioning circuit (Figure 5.3).*

5.2 Half-wave conditioning circuit

5.2.1 Half-wave circuit configuration

Figure 5.3 a) shows the experimental circuit with its circuit diagram. In half-wave, the minus node of the TENG and the minus node of the capacitor are connected to the ground, which attenuates the noise charge effect.
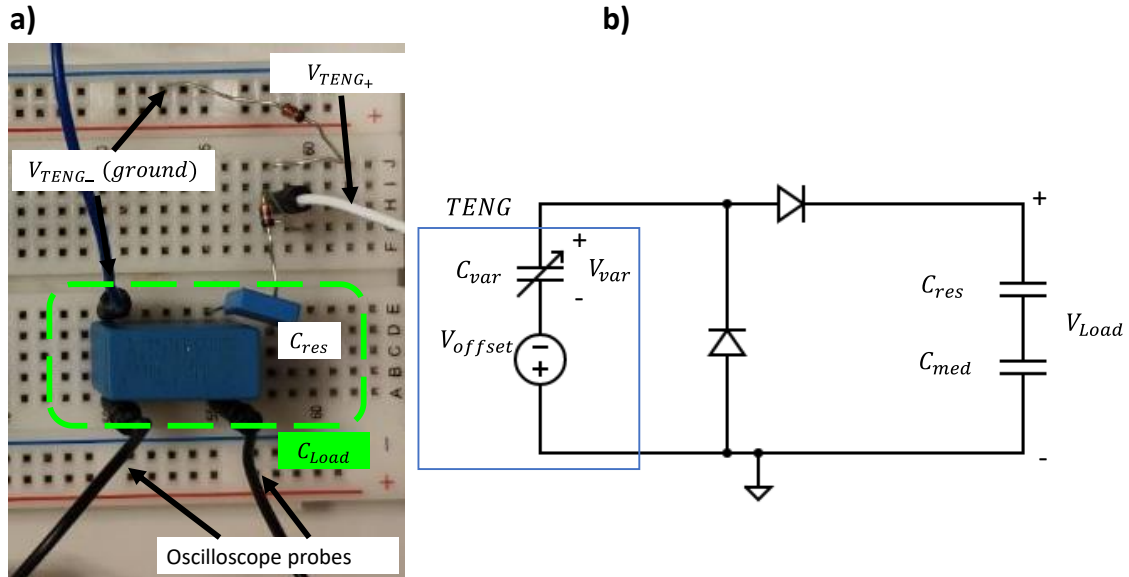
Figure 5.3. *Half-wave conditioning circuit. a) is a picture of the experimental circuit, b) shows the circuit diagram of the half-wave rectifier conditioning circuit is.*

5.2.2 Reproducibility test of half-wave voltage curves

To study the reproducibility of the system, Figure 5.4 shows several recorded voltage curves. They have been recorded working at 5 Hz and 50 Hz. These measurements have been taken at each frequency in the same conditions. The behaviour of this conditioning circuit is discussed in Chapter 3, section 3.4.3. It can be seen how due to the shaker excitation the nanogenerator gradually charges the load capacitor. In fact, a closer view of these curves (see Figure 5.2 b) discloses a step-like profile ascribed to the fast charge pulse during the on-state of the upper diode in Figure 5.3These plots also show their fitting curves, coloured in magenta. These fitting curves represent the general behaviour of each curve, filtering any AC perturbation. In the case of the 5 Hz curves, it can be seen that reproducibility is hard to achieve, as the voltage saturation changes between measurements, especially at 50 Hz. The reason for this is due to a strong dependence on TENG initial conditions, especially with the surface charge stored in the PFA. If this charge gets lower, then the saturation voltage is lower, as expression (3.35) indicates. On the other hand, the initial background is much more stable and limited to few volts
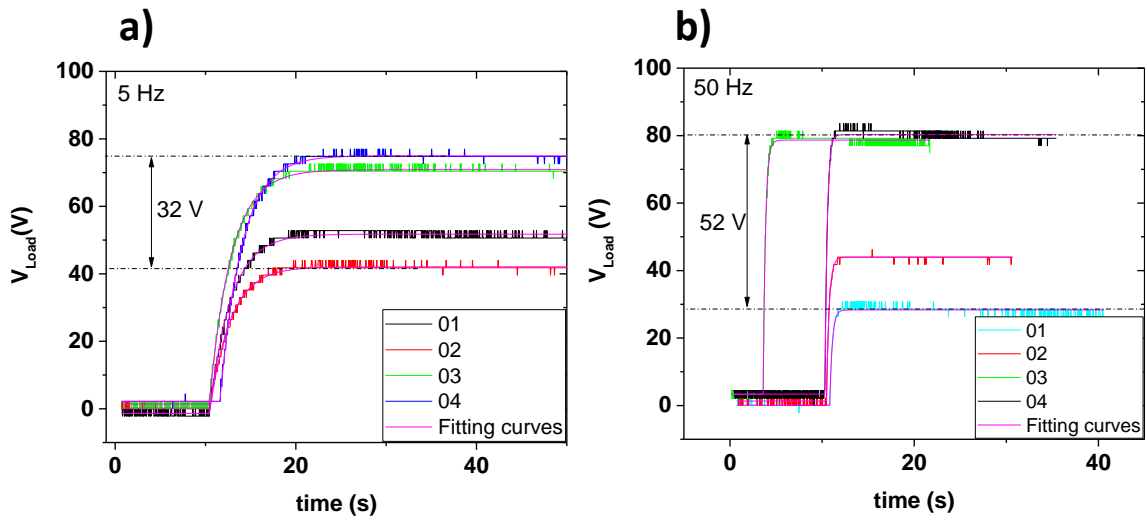
Figure 5.4. *Experimental voltage curves registered using half-wave conditioning circuit (Figure 5.3). The used excitation signal was a) 5 Hz and b) 50 Hz.*

Measurements at both frequencies show the same qualitative behaviour. The voltage increase per cycle is smaller as the voltage gets closer to the saturation value. This behaviour agrees with the theoretical discussion carried out in Chapter 1, section 1.4, and with the literature [2], [7].

Table 5.1 *Fitting parameters for the half-wave voltage curves at 5 Hz in Figure 5.4 a). The provided uncertainties are those associated with the fitting process.*

Curve	$\tau(s)$	$V_{sat}(s)$	r^2
01	2.36 ± 0.01	51.76 ± 0.1	0.997
02	2.311 ± 0.01	42.0 ± 0.1	0.998
03	2.44 ± 0.01	70.7 ± 0.1	0.998
04	2.430 ± 0.008	74.8 ± 0.1	0.999

Table 5.2 *Fitting parameters for the half-wave voltage curves at 5 Hz in Figure 5.4 a). The provided uncertainties are those associated with the fitting process.*

Curve	$\tau(s)$	$V_{sat}(s)$	r^2
01	0.26 ± 0.01	28.21 ± 0.1	0.994
02	0.285 ± 0.005	43.95 ± 0.1	0.998
03	0.248 ± 0.001	78.6 ± 0.1	0.998
04	0.244 ± 0.003	80.2 ± 0.1	0.998

Tables 5.1 and 5.2 show the fitting parameters for the voltage curves in Figure 5.4. Regression coefficients values support the goodness of the used fitting model. In addition, the characteristic time constants are consistent between curves of the same frequency. Increasing the excitation frequency in one order of magnitude, from 5 Hz to 50 Hz, leads to a similar reduction of the rise time (τ). Hereafter, the presented graphs for the half-wave circuit are calculated from measurements 04 in the case of both frequencies 5 Hz and 50 Hz series.

5.2.3 Half-wave output power analysis

The obtained power transmitted curves versus time at 5 Hz and 50 Hz are shown in Figure 5.5. The registered maximum powers are in the range of the micro-watt. There, the 5 Hz curve is multiplied by 5 to improve its visualization. Both curves show similar qualitative behaviours. Once the shaker is switched on, the transmitted power increases rapidly. After a given number of cycles, the output power reaches a maximum value. Then, it decreases as the capacitor load approaches the voltage saturation value. When this voltage value is reached, the transmitted power drops to zero.

In the figure, we identify a strong dependence on the working frequency. The power curve for a 50 Hz excitation displays a shaper profile with a maximum shifted to shorter times. This is so because of the higher number of cycles per unit of time, which leads to a faster charging process, as it is observed in the V (t) curves in Figure 5.4. Similarly, the maximum instantaneous transferred power at 50 Hz is considerably higher than in the 5 Hz case.
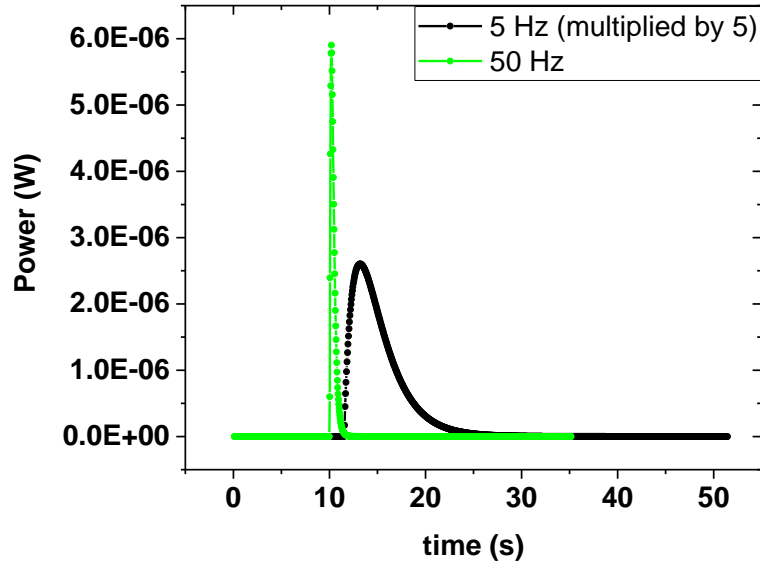
Figure 5.5 *Power transmitted versus time in half-wave conditioning at 5 Hz and 50 Hz.*

In order to identify the optimal voltage operation, Figure 5.6 shows the output power versus the voltage stored in the load capacitor. This point is the voltage across the load capacitor which provides the maximum power transmission. As it is discussed in section 1.4 this determines the optimal operation regime of the nanogenerator. Both frequencies show the same trends. A parabolic shape is defined in both curves, showing an optimal voltage that assures the maximum power transmitted. The 50 Hz curve is considerably sharper than the 5 Hz due to its higher maximum output power. Although the working frequencies are different, both curves seem to find similar values for the optimal voltage. This is reasonable, since the optimal voltage value is in principle independent from the frequency, as it indicates expression (3.39), being only defined by the voltage stored between the PFA layer and the bottom electrode, and TENG maximum and minimum capacities. Table 5.3 shows the maximum output power, P_{max}, optimal voltage point operation, $V_{optimal}$, and the number of cycles needed to reach this maximum N_{cycles}, for both frequencies.
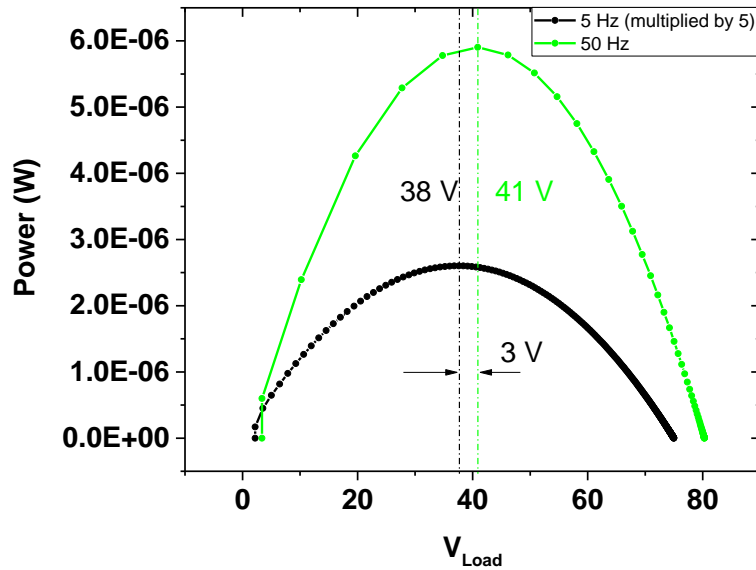
Figure 5.6 *Power transmitted versus the voltage stored in the load capacitor in half-wave conditioning at 5 Hz and 50 Hz.*

To improve this comparison, Table 5.2 shows the maximum output power, P_{max}, optimal voltage point operation, $V_{optimal}$, and the number of cycles needed to reach this maximum N_{cycles}, and the at both frequencies.

Table 5.3 *Characteristic magnitudes registered from the experimental half-wave output power transmission study at 5 Hz and 50 Hz.*

Frequency	$P_{max}(\mu W)$	$V_{optimal}\ (V)$	N_{cycles}
5 Hz	0.52	38	8
50 Hz	5.90	41	10

The maximum output power at 50 Hz is around 10 times higher than at 5 Hz. This magnitude seems to be directly related to the working frequency. On the other hand, the optimal voltage operation is achieved almost at the same values at both frequencies, being around 40 V. The number of cycles needed to achieve this maximum power is also very similar, being close to 9 cycles. Therefore, for half-wave conditioning, the maximum power transmitted has a strong dependence on the working frequency. On the other hand, the optimal voltage operation point and the cycles needed to achieve the maximum power seems to be independent of the frequency.

5.3 Full-wave rectifier

5.3.1 Full-wave circuit configuration

Figure 5.7 shows the experimental circuit used for this configuration. The capacitors and diodes used in this circuit are of the same model as those used for half-wave.
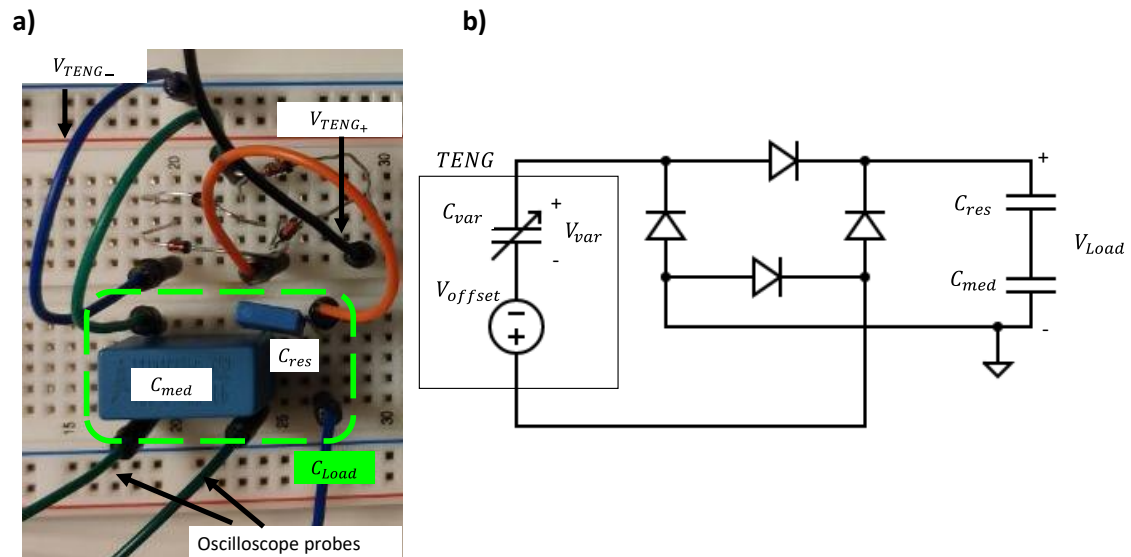
Figure 5.7. *Full-wave conditioning circuit. a) picture of the experimental circuit b) shows the circuit diagram of the half-wave rectifier conditioning circuit is.*

5.3.2 Reproducibility test of full-wave voltage curves

Reproducibility test results are presented in Figure 5.8. All the curves in each graph have been measured in the same conditions defined at the beginning of the chapter. The figure shows a lack of reproducibility, as it was observed for the half-wave circuits, which in this case also affects the initial values (background level). This behaviour has also been reported in reference [5].
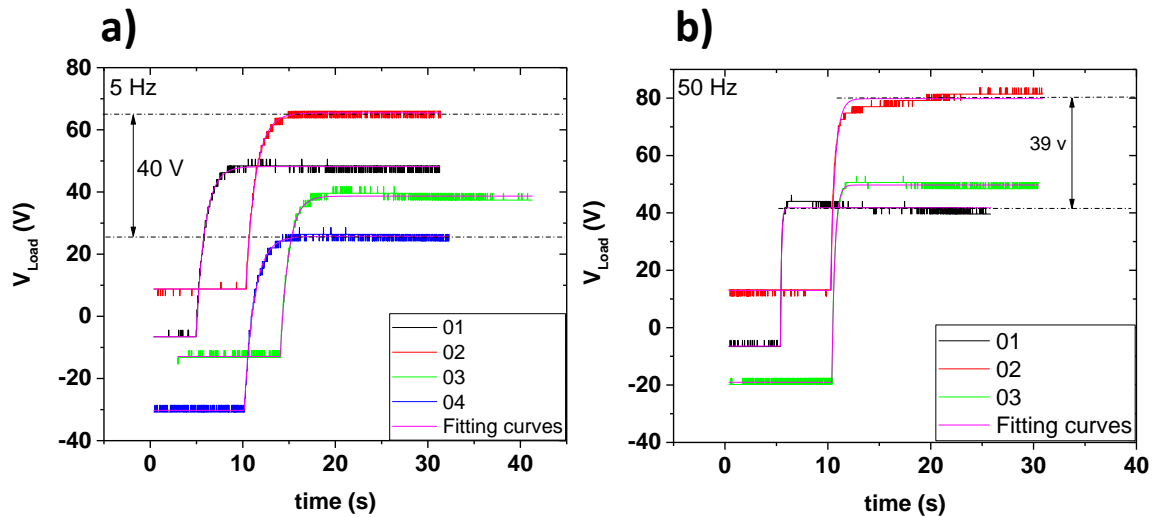
Figure 5.8. *Experimental voltage curves registered using full-wave conditioning circuit (Figure 5.7). The used excitation signal was a) 5 Hz and b) 50 Hz.*

It can be seen how measurement number 2 of the 50 Hz measurements group present a little diversion from its saturation plateau at a certain time. This is due to a sudden increase in the PFA surface charge. The fitting parameters of such curves are presented in Tables 5.4 and 5.5. In this case, a significant dispersion of the fitting parameters is observed at both frequencies. Voltage saturation dispersion is similar to half-wave results. But in contrast with half-wave result in this case lack of reproducibility also affect the characteristics rising time. Poor reproducibility is an important issue to address in further developments. Hereafter, the analysed data for the full-wave circuit are calculated from measurements 01 and 03 of frequencies 5 Hz and 50 Hz series, respectively.

Table 5.4 *Fitting parameters of full-wave voltage curves at 5 Hz in Figure 5.8 a). The provided uncertainties are those associated with the fitting process.*

5 Hz	$\tau(s)$	$V_{sat}(s)$	r^2
01	0.641 ± 0.004	48.1 ± 0.1	0.998
02	1.076 ± 0.006	65.4 ± 0.1	0.9990
03	0.897 ± 0.008	38.6 ± 0.1	0.997
04	1.093 ± 0.004	25.7 ± 0.1	0.998

Table 5.5 *Fitting parameters of full-wave voltage curves at 50 Hz in Figure 5.8 a). The provided uncertainties are those associated with the fitting process.*

50 Hz	$\tau(s)$	$V_{sat}(s)$	r^2
01	0.10 ± 0.004	41.7 ± 0.1	0.995
02	0.44 ± 0.004	79.8 ± 0.1	0.996
03	0.29 ± 0.008	49.7 ± 0.1	0.998

5.3.3 Full-wave output power analysis

Figure 5.9 shows the output power transmitted versus the time in the case of a full-wave conditioning circuit. The qualitative behaviour is very similar to half-wave results. However, full-wave power curves describe two negative peaks that were not present in half-wave results. These negative peaks appear just after the shaker is activated. They are caused by the initial negative voltages stored in the load due to noise action. Initially, the power is spent to restore the zero level. Therefore, the 50 Hz negative peak is only higher than the 5 Hz peak because its initial voltage is lower. Since initial voltages are not affected by the working frequency, this difference between peaks is meaningless. On the other hand, Figure 5.10 shows the output power versus the voltage stored in the capacitor. disregarding the negative peaks, the shape of the curves is similar to half-wave results.
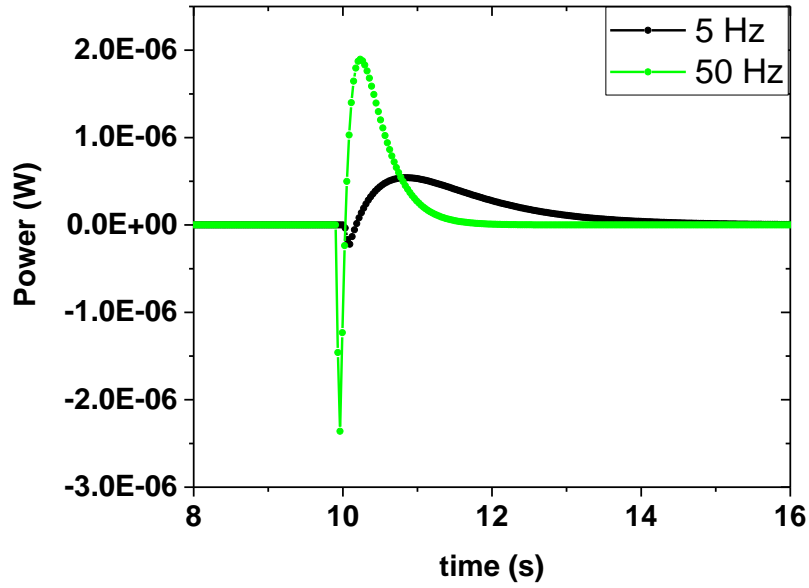
Figure 5.9 *Power transmitted versus time in full-wave conditioning at 5 Hz and 50 Hz.*

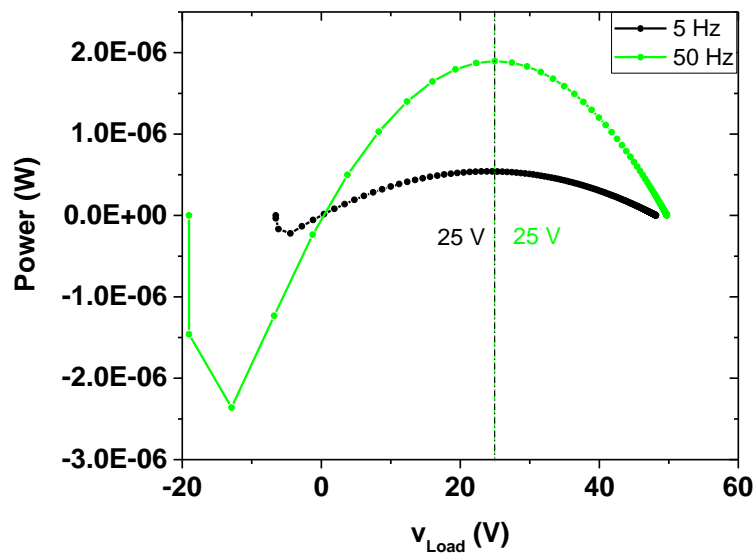**Figure 5.10** *Power transmitted versus time in full-wave conditioning at 5 Hz and 50 Hz.*

To compare full-wave power transmission in terms of frequency, Table 5.6 gathers the characteristic magnitudes of these curves. The table shows the maximum power registered, P_{max}, the optimal voltage operation point, $V_{optimal}$, and the number of cycles required to reach the maximum transmitted power, N_{cycles}.

Table 5.6 *Characteristic magnitudes registered from the experimental half-wave output power transmission study at 5 Hz and 50 Hz.*

Frequency	$P_{max}(\mu W)$	$V_{optimal}$ (V)	N_{cycles}
5 Hz	0.54	25	3
50 Hz	1.89	25	7

For full-wave, due to the presence of the negative peaks, N_{cycles}. Is set to cero when the initial negative voltage is corrected; i.e. the cycles invested in the correction of the negative peaks are not considered. In this table, the factor between maximum output powers is around 3. As reported before for the half-wave the optimal voltage point does not depend on the excitation frequency, being around 25 V for both curves. However, they are not agreeing on the necessary number of cycles needed to reach the maximum. This disparity probably comes from differences in the stored charge on the PFA at the moment the measurements were taken.

5.4 Performance comparison between half-wave and full-wave conditioning

5.4.1 Reproducibility

Reproducibility is hard to achieve in both kinds of circuits, due to unpredictable variations of the PFA surface charge and noise issues that also affect the initial charge of the capacitors. Similar anomalies have also been observed in the literature[5]. This is an important issue to address in further developments.

5.4.2 Voltage and power curves

Table 5.7 and Table 5.8 compares the principal characteristic parameters of the registered voltage and power curves for both circuits. As expected, for both circuits the 50 Hz excitation provides a faster voltage increase than 5 Hz excitation (Table 5.7). In the case of the slow excitation of 5 Hz, it seems that the full-wave circuit injects charge into C_{load} faster than the half-wave option. However, the instantaneous maximum power is similar for both circuits at this excitation frequency (Table 5.8), which is the most representative for an environmental actuation.

Unfortunately, the lack of reproducibility for the fast excitation (50 Hz) data impedes reaching a reliable conclusion about the speed of the charging process and therefore the transferred power. Similarly, no compulsion can be inferred about the saturation level due to the high dispersion of the obtained values.

Table 5.7 *Comparison of the experimental voltage curves characteristic parameters of the RC model used for the fitting.*

Circuit	Frequency	$\tau(s)$	$V_{sat}(s)$
Half-wave	5 Hz	2.43	74.8
	50 Hz	0.244	80.2
Full-wave	5 Hz	0.641	48.1
	50 Hz	0.29	49.7

Table 5.8 *Comparison of the experimental output-power curves characteristic magnitudes.*

Circuit	Frequency	$P_{max}(\mu W)$	$V_{optimal}\ (V)$	N_{cycles}
Half-wave	5 Hz	0.52	38	8
	50 Hz	5.90	41	10
Full-wave	5 Hz	0.54	25	3
	50 Hz	1.89	25	7

6. SIMULATIONS

This chapter aims to show the work done in TENG simulations using MATLAB Simulink. These simulations are used to study how accurate is the TENG electric model shown in Chapter 1. Hence, their main purpose is to assess the correct matching between experimental results and theoretical development. In this way, the objective is to replicate the experimental results using the available lumped model for such TENGs.

At this point, it is worthy of mention that, as indicated in Chapter 2, the simulation tasks described herein were developed simultaneously with the experimental work described in Chapter 4 and Chapter 5. Due to the similarities of the used simulations tools and for sake of clarity, it was decided to gather all the simulations results and the corresponding models in the same chapter. This decision was also supported by the fact that Chapter 3 is mainly devoted to the development, optimization and validation of the experimental characterization platform.

The structure of this chapter consists of three main parts. The first section shows the general method follow in order to design the simulation model on Simulink. Then, a second section discusses the models developed for power transmission to a resistive load simulation, with its results. The last section is dedicated to conditioning circuit simulations.

6.1 Simulation method

In this section, the general aspects of the designed simulation models are discussed. Hence, all the settings and architectures shown in this section are applied for every simulation model. Details about the particular settings required for each model are discussed in further sections.

6.1.1 The Simscape library

Simulink provides a wide range of tools to study electronic systems. It counts with a full library named *Simscape*, equipped with several sub-libraries oriented to the simulation of Multiphysics systems. Therefore, all the used modules in these simulations come from one of such sub-libraries, named *elec_lib*. This library is focused on electric and electronic simulations, perfectly meeting the needs of this study.

6.1.2 General architecture in simulation models
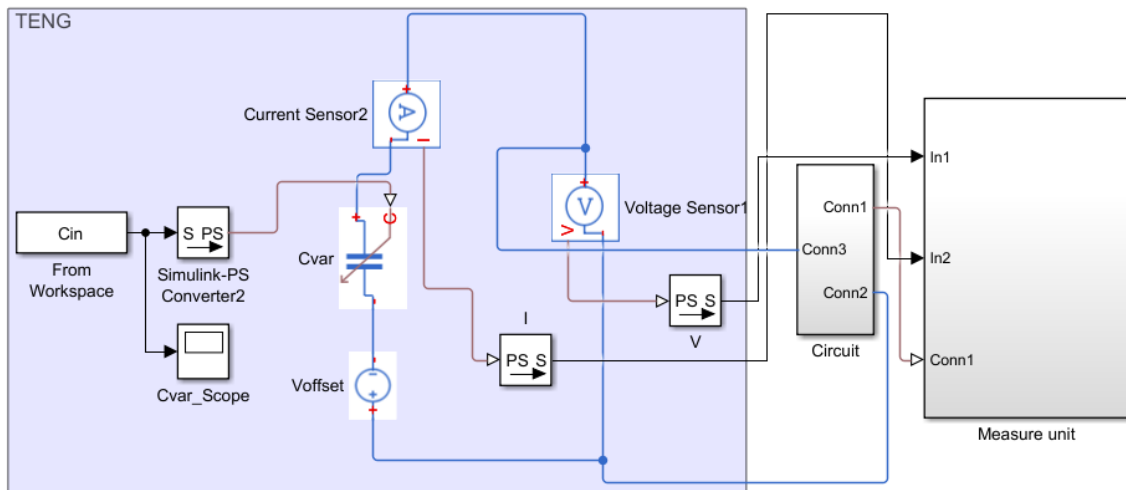
Figure 6.1. *The general architecture used for simulation models. The TENG model subsystem has been expanded to show a more detailed description.*

The general architecture used for simulations is shown in Figure 6.1. Every simulation model is composed of three main subsystems.

- ***The TENG model subsystem,*** which is equal for every simulation.

- ***The circuit subsystem,*** containing a resistance load or a conditioning circuit, depending on the study of interest.

- ***The measuring unit,*** containing the blocks employed for processing, storing and visualizing data. These changes depending on the simulation which is being carried out.

Figure 6.1 also shows the different connections between modules. The colour of each line depends on the type of data transmitted. Black lines carry classical Simulink-type data, working with the standard matrix format of MATLAB. The blue lines work as wires where Kirchhoff laws must be satisfied. At last, magenta-coloured lines carry physical signals ant they are used to establish the translation between electric data and Simulink-type data. All the output data need to be converted into Simulink-type signals to be processed.
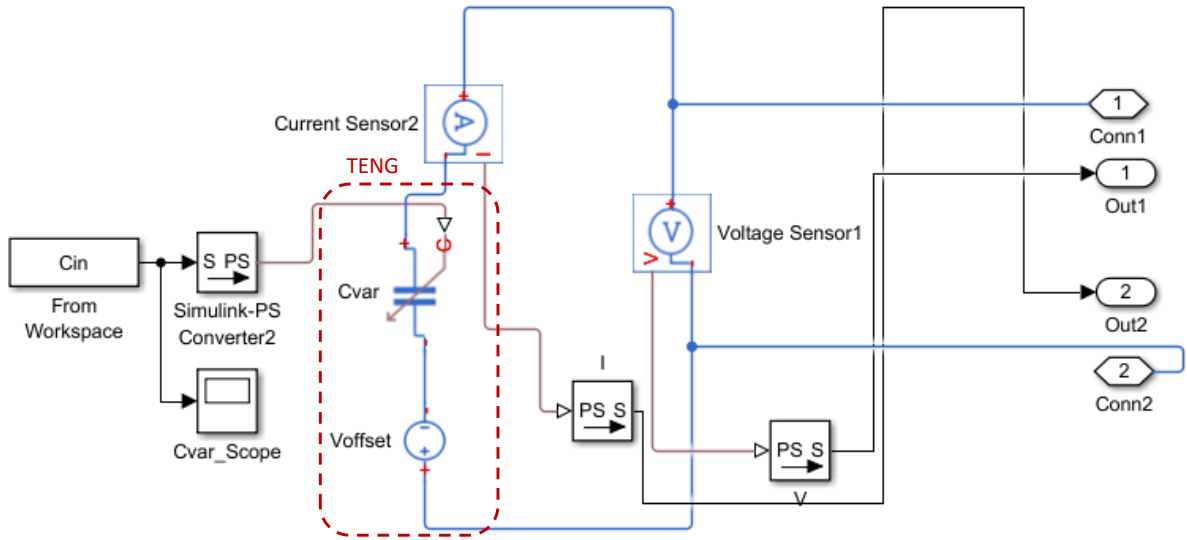
6.1.3 The TENG electric model

***Figure 6.2.** TENG electric model subsystem in Simulink.*

Figure 6.2 shows how the TENG electric model has been implemented. The electric model is placed in the centre of the image. As it was discussed in section 3.3.4, the used TENG lumped model consists of a variable capacitor, C_{var}, and a DC voltage source, V_{offset}. The TENG model is placed into a Simulink subsystem, which makes easier its manipulation. This subsystem carries specific blocks to test TENG model behaviour. Thus, a scope has been placed to watch the shape of the capacitance signals, and a voltmeter and an amperemeter to measure the voltage across the TENG and its output current.

The variable capacitor named C_{var} comes from the folder named *Passive devices* inside *elec_lib*. It uses an external signal as capacitance, applying the following equation:

$$I = \frac{dQ}{dt} = \frac{d(CV)}{dt} = \frac{dV_{var}}{dt}C_{var}(t) + V_{var}\frac{dC_{var}(t)}{dt} \tag{6.1}$$

Where V_{var} is the voltage across the variable capacitor and $C_{var}(t)$ is its capacitance, which is a time-dependent function. This function is defined from the workspace using expressions (3.24) and (3.25).

With these three equations, the electric behaviour of the variable capacitor is fully defined. Furthermore, the block needs some more definitions. It requires an explicit definition of the minimum possible capacitance in order to avoid a null value. Also, the initial charge of the capacitor needs to be defined, which is set to zero. On the other hand, V_{offset} is modelled using a

66

DC source block, which comes from the *sources* section of *elec_lib*. This source only requires the definition of its DC value. Every AC option has been disabled.

In order to adjust simulation results to experimental results, two free parameters are used. These parameters are the value of V_{offset} and the parameter k of expression (3.24). The reason is that there is no consistent way to perform an experimental measurement of the voltage across the bottom aluminium electrode and the PFA layer. The same thing happens to parameter k since it is hard to achieve a reliable read about how much time the device remains at C_{min}.

### 6.1.4 Setting simulation parameters using a control script

All the parameters of the simulation are controlled using a script where all blocks parameters are defined. simulations have been performed using a variable time step to minimize computational effort. The simulation time, *T*, is defined in such script. in it, a variable named *Resolution* contains the smallest time step allowed. Then, the system decides which steps should be used in each moment depending on the achieved convergence regarding a certain error tolerance. The standard used *Resolution* is 10^{-6} s, being the maximum appliable steps of 10^{-4} s when the committed error is low enough. This standard value for *Resolution* is chosen to keep in mind the limitations of the used hardware. To generate the capacitance signal for the variable capacitor, the value in *Resolution* is also used. Using the time simulation, *T* and the *Resolution* parameter, the script calculates the capacitance signal. In this way, there are always $T \cdot 10^{6}$ values for the capacitance signal in every simulation.

6.2 Simulation of TENG voltage curves and power transmission.

The simulations presented in this section aim to study TENG response in the presence of a resistive load. For hence, in this section, the particular settings of such calculations are be presented, while its results are shown afterwards.

6.2.1 Simulation settings
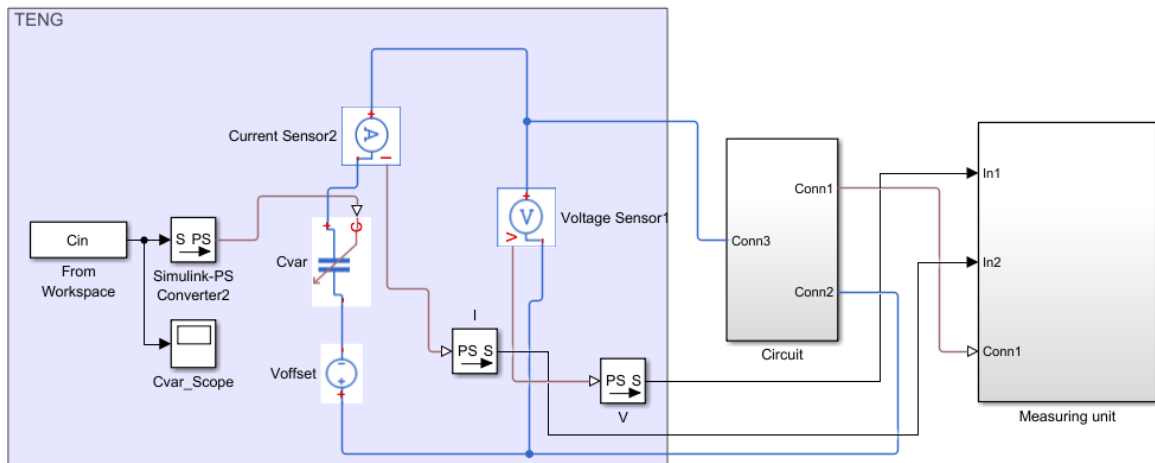
Figure 6.3. *The simulation model employed to measure electric response and power transmission to a resistive load.*

Figure 6.3 shows the used Simulink model. The circuit subsystem is composed of a resistive load, where a voltmeter has been added in order to track its voltage. The load resistance value is controlled by the control script. On the other hand, the designed measure unit allows us to record the voltage values across the load, while it performs an automatic calculation of the instantaneous transmitted power, having real-time visualization of both magnitudes. These instantaneous power transmitted values are integrated and divided by the simulation time to calculate the average power transmitted. Finally, a secondary scope has been added in order to watch the internal behaviour of the TENG model subsystem.

To store the results, a structure is generated in the workspace. This structure contains the corresponding array of the registered voltage values with their timestamps. It also includes the calculated average power transmitted to the load. For this study the simulations start from steady-state, improving convergence and reducing the required computational effort.

6.2.2 Adjusting simulation parameters

To establish the values of V_{offset} and k, an iterative process has been carried out trying to match as better as possible simulations to experimental voltage curves. The used reference has been the voltage curve registered for 550 MΩ, working at 5Hz. Since V_{offset} has a strong influence on voltage waves amplitude, it has been shifted until simulation waves amplitude match the experimental results. The conclusion was that V_{offset} should be around -80 V which is a reasonable value for PFA layers. After some iterations, it was found that the best value for k is 1. Little

68

variations on the *k* parameter do not show a real impact on the results, showing that after a critical value of such parameter, simulation quality cannot be improved.

6.2.3 Output Voltage variations as a function of the load

The experimental study about DUT voltage peaks is reproduced in simulation. Therefore, several voltage waves have been calculated by performing a sweep on the resistance load value. The obtained curves are shown in Figure 6.4. The simulations describe a shape evolution that is very similar to the observed evolution in experimental curves. Thus, this shape variation with the applied load is intrinsic to the behaviour of the TENG, since its electric model can justify such evolution.
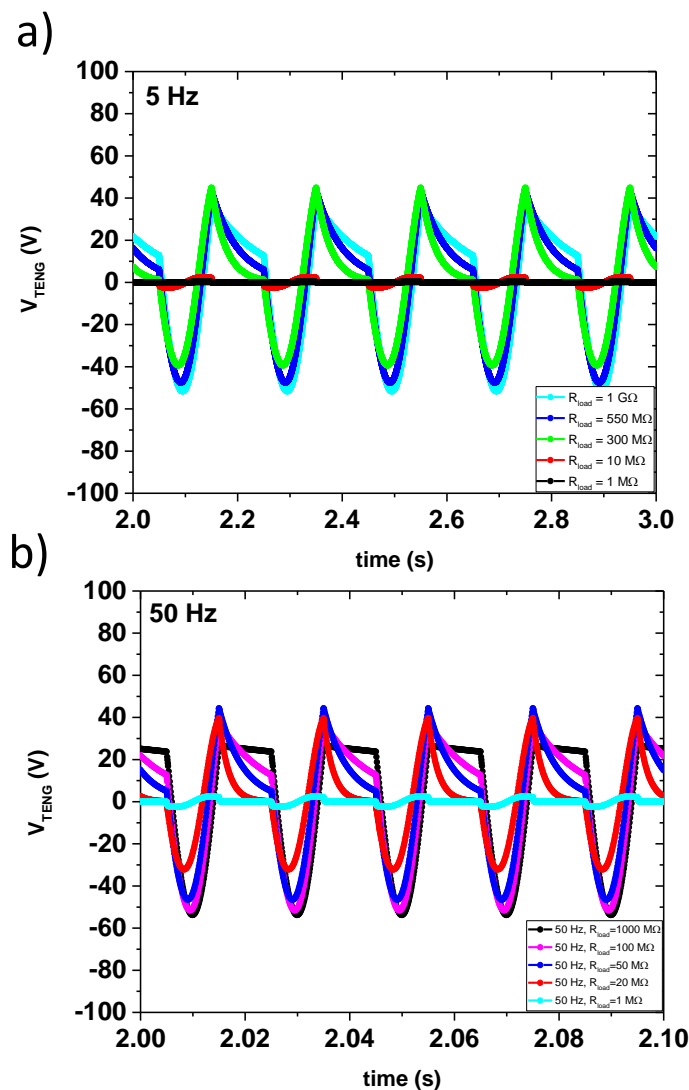
Figure 6.4. Voltage signals are acquired in simulation for different loads, at different work frequencies. a) 5 Hz b) 50 Hz.

In Figure 6.4 that the amplitude of the voltage waves increases faster with an increase of the load when such load is lower than the optimal one. This can be seen in 5 Hz voltage signals, where the amplitude difference between 10 MΩ and 300 MΩ curves are significantly higher than between 300 MΩ and 1 GΩ. To have some reference values for the optimal loads, the experimental ones can be considered, which are 550 MΩ and 50 MΩ at 5 Hz and 50 Hz, respectively.

However, simulations do not find the same optimal loads, as it is shown in further sections. This behaviour agrees with the experimental results, where the shape of the curves seems to be related to the difference between the applied load and the optimal one.

The 50 Hz curves support this trend, showing voltage waves with similar shape evolution, but at lower loads due to its optimal load is also lower. It is remarkable that for both frequencies, the farther the applied resistance is from the optimal one, the more asymmetric voltage waves become.

6.2.4 Comparison between experimental and simulation results

A more detailed comparison between experimental results and simulations is proposed in Figure 6.5. It can be seen that experimental and simulation curves show the same qualitative behaviour. This is especially true for 5 Hz curves, where the matching between results is considerably high. However, there are some quantitative discrepancies between curves. The simulated peaks seem to grow faster than experimental peaks do, showing higher slopes in their rising transitions. Disparities between results are higher in measurements at 50 Hz. The main cause of this is probably dumping, introduced by the mechanical inertia of the electrodes, which a poorer adjustment to experimental results than 5 Hz curves. For both frequencies, at loads higher than 1 GΩ, planar shapes start to arise on the top of the voltage waves calculated in simulations. This has not been observed in experimental curves. However, some studies have reported this type of planar structure [55], which enforces the simulation results.
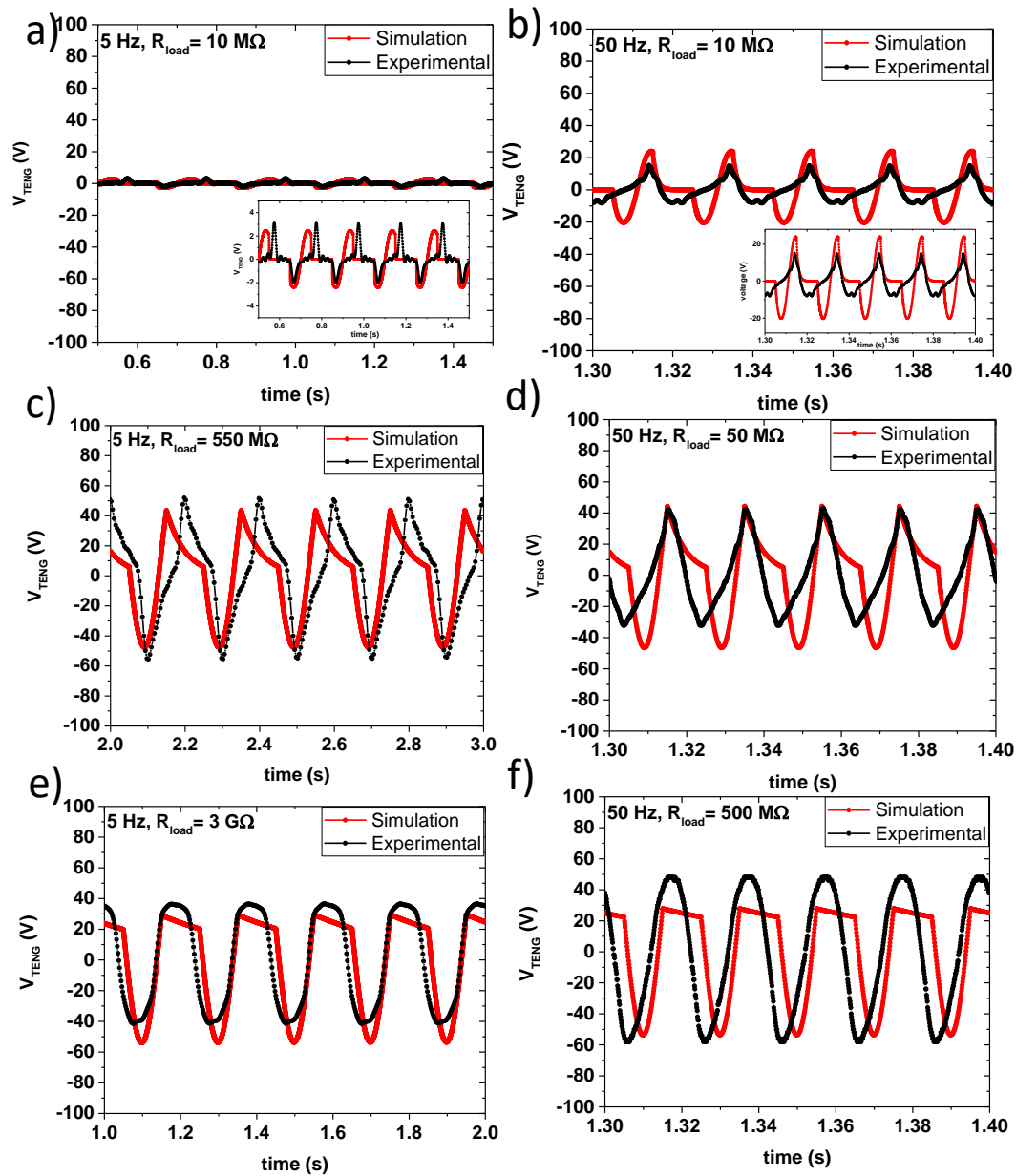
Figure 6.5. *Simulation and experimental voltage curves comparison at 5 Hz and 50 Hz. a), b) loads higher than the optimal c), d) optimal loads, e), f) loads lower to the optimal ones*

A more detailed comparison between experimental results and simulations is proposed in Figure 6.5. It can be seen that experimental and simulation curves show the same qualitative behaviour. This is especially true for 5 Hz curves, where the matching between results is considerably high. However, there are some quantitative discrepancies between curves. The simulated peaks seem to grow faster than experimental peaks do, showing higher slopes in their rising transitions. Disparities between results are higher in measurements at 50 Hz. The main cause of this is probably dumping, introduced by the mechanical inertia of the electrodes, which is not considered in the simulation model. This also explains why 50 Hz simulations results have

a poorer adjustment to experimental results than 5 Hz curves. For both frequencies, at loads higher than 1 GΩ, planar shapes start to arise on the top of the voltage waves calculated in simulations. This has not been observed in experimental curves. However, some studies have reported this type of planar structure [55], which enforces the simulation results.

6.2.5 Average power transmitted versus the applied load in simulations

Figure 6.6 shows a comparison between the experimental and calculated simulation average power transmitted versus the applied load. At a qualitative level, simulations are matching the experimental behaviour. It can be seen how the transmitted power increase as the load gets closer to the internal impedances value of the TENG. Higher loads lead to a decrease in the transmitted power. Also, simulations are correctly showing how if the frequency is increased, the internal load of the DUT decreases. However, simulation results are not exactly matching the experimental ones. First, optimal loads are considerably different. Simulations indicate that the optimal load working at 5 Hz is found at 235 MΩ while experimental results found that it is around 550 MΩ. This difference is also present in the case of 50 Hz, where the simulations found that the optimal load is 22 MΩ where experimental results show it is close to 50 MΩ.

In addition, the simulations overrate the transmitted power. It can be seen that power average discrepancies are stronger at 50 Hz than at 5 Hz. Regarding this difference, It is consistent to think that the dumping effect is playing the main role in these mismatches.
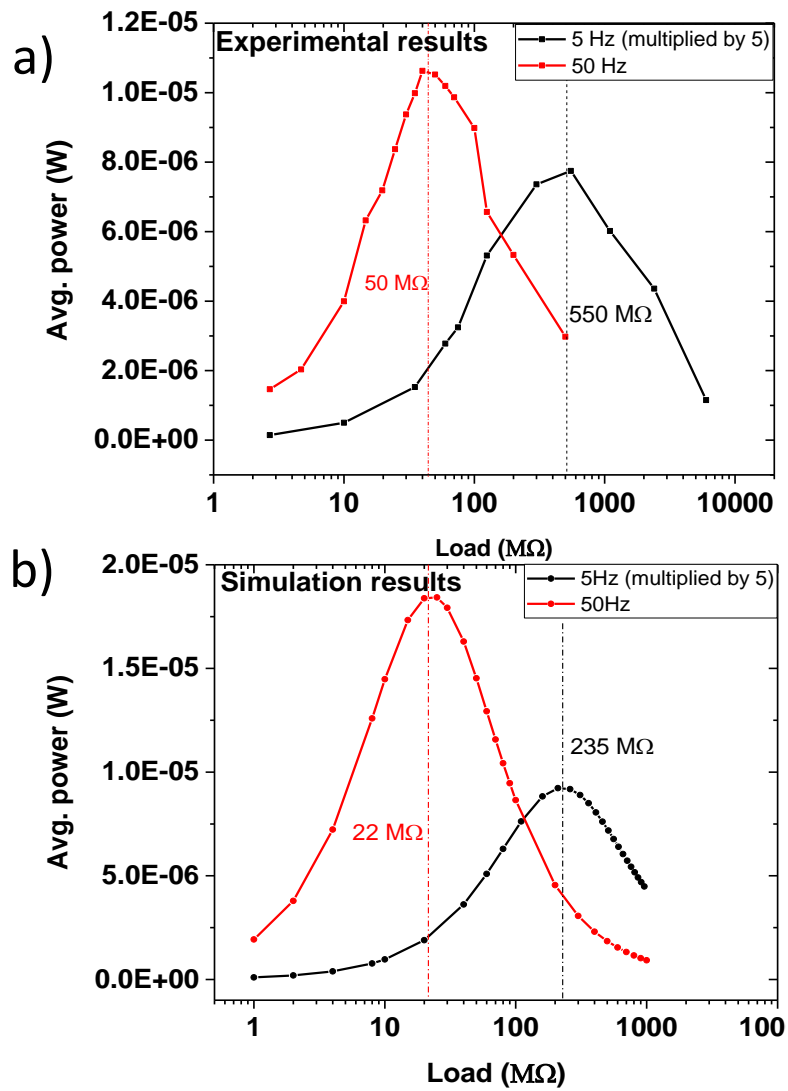
Figure 6.6. *Average power transmitted versus the applied resistive load in experimental results (image a)) and in simulation (image b)) at 5 Hz and 50 Hz. The results have been plotted in a semi-log graph to improve its visualization.*

Table 6.1. *Comparison between characteristic values in average power transmission to a resistive load.*

	Experimental		Simulation	
Frequency	*Optimum R_{load}*	*Maximum P_{avg}*	*Optimum R_{load}*	*Maximum P_{avg}*
5Hz	550 *M*Ω	1.54 μW	235 *M*Ω	1.844 μW
50Hz	50 *M*Ω	10.57μW	22 *M*Ω	18.40 μW

Table 6.2. *Errors between simulations and experimental results in the power transmitted to a resistive load study. The error is calculated using expression (6.2).*

	Relative error (%)	
Frequency	$Optimum\ R_{load}$	$Maximum\ P_{avg}$
$5Hz$	57.27	19.74
$50Hz$	56.11	74.08

In order to improve this comparison between simulations and experimental results, Table 6.1 shows the optimal load and the maximum power transmitted at 5 Hz and 50 Hz. Furthermore, Table 6.2 show the committed errors in such magnitudes. The used error function was the following:

$$\Delta A(\%) = \frac{|A_{experimental} - A_{simulation}|}{A_{experimental}} \cdot 100\ \%$$ (6.2)

where ΔA is the in percentual error, $A_{experimental}$ is the experimental value of the magnitude and $A_{simulation}$ is the value calculated in simulation. Table 6.1 indicates that the internal load of the DUT is overrated by the simulations in a factor of 2 at both frequencies. The cause does not seem to be dumping, since measurements of both frequencies are affected equally. This might be caused by imprecision in the determination of the experimental capacities. Note that the ratio between C_{max}/C_{min} is extremely important in the shape of the power transmission curves, and their values are small, in the pico-faraday order. Thus, reasonable to expect that little errors in their determination can lead to significant differences when determining the optimal load that maximizes the out power, ie. the internal load of the TENG. Besides, imprecisions in V_{offset} may have contributed to such deviations.

On the other hand, the maximum power transmitted predicted in simulation is considerably similar to its experimental value at 5 Hz. With the increase of frequency, this accuracy gets worse due to the higher influence of dumping. Therefore, simulations seem to be meeting correctly experimental results in terms of power transmittance at low frequencies, although their reliability in optimal loads prediction is considerably low.

6.2.6 Main sources of error of the TENG electric model

These similarities and diversions between simulations and experimental results seem to indicate that the TENG electric model used is achieving a correct replication of the bases in actual TENG behaviour, but with clear limitations. Therefore, it should be considered as a first-order model. However, there more critical factors that have been not considered in the model are the following ones:

- *Mechanical dumping* has proved to be the main source of error.
- *The actual evolution of the surface charge on the triboelectric layer*, which has been modelled as a constant voltage in simulation.
- *Border capacities* have not been modelled.
- *imperfections in the planar shape* of PFA and top electrode, producing an inhomogeneous surface charge on the triboelectric layer.
-

6.3 Conditioning circuits simulations.

The following section presents the obtained results in the simulation of conditioning circuits. Following the same structure as the previous section, the simulation model is presented followed by the obtained results.

6.3.1 Implementation of piecewise diodes

The used diodes are from the already mentioned *elec_lib,* being placed in the *semiconductor devices* folder. This block does not use the classic Shockley equation, but a piecewise linear one:

$$\begin{cases} I = \dfrac{V - V_F\left(1 - R_{on}G_{off}\right)}{R_{on}} & if \ V > V_F \\ I = VG_{off} & if \ V < V_F \end{cases} \tag{6.5}$$

Where V is the applied voltage, V_F is the diode voltage forward, R_{on} is the applied resistance in the forward direction, and G_{off} is the conductivity of the diode in its reverse direction. This election aims to reduce computational effort. Since diodes only work as passive switches, an accurate description of their behaviour would overcomplicate simulations without any significant gain. Trying to replicate the characteristics of the diodes used in the experiments, $V_F, R_{on},$ and G_{off} is 0.6 V, 0.3 Ω and $1 \cdot 10^{-10}$ Ω^{-1}, respectively.

6.3.2 Half-wave conditioning model in simulations

Figure 6.7 shows the used simulation model for the implementation of half-wave conditioning circuits. This time, the solver works out of the steady-state since the transient evolution is the main point of interest. The circuit subsystem, named "Half-wave", contains the conditioning circuit, while the measuring unit is just composed of a scope and a storage block. In this case, the simulation results receive the same treatment as the experimental data. Therefore, voltage results are stored in an array with their timestamps. Afterwards, data is exported to Origin Lab to be processed.
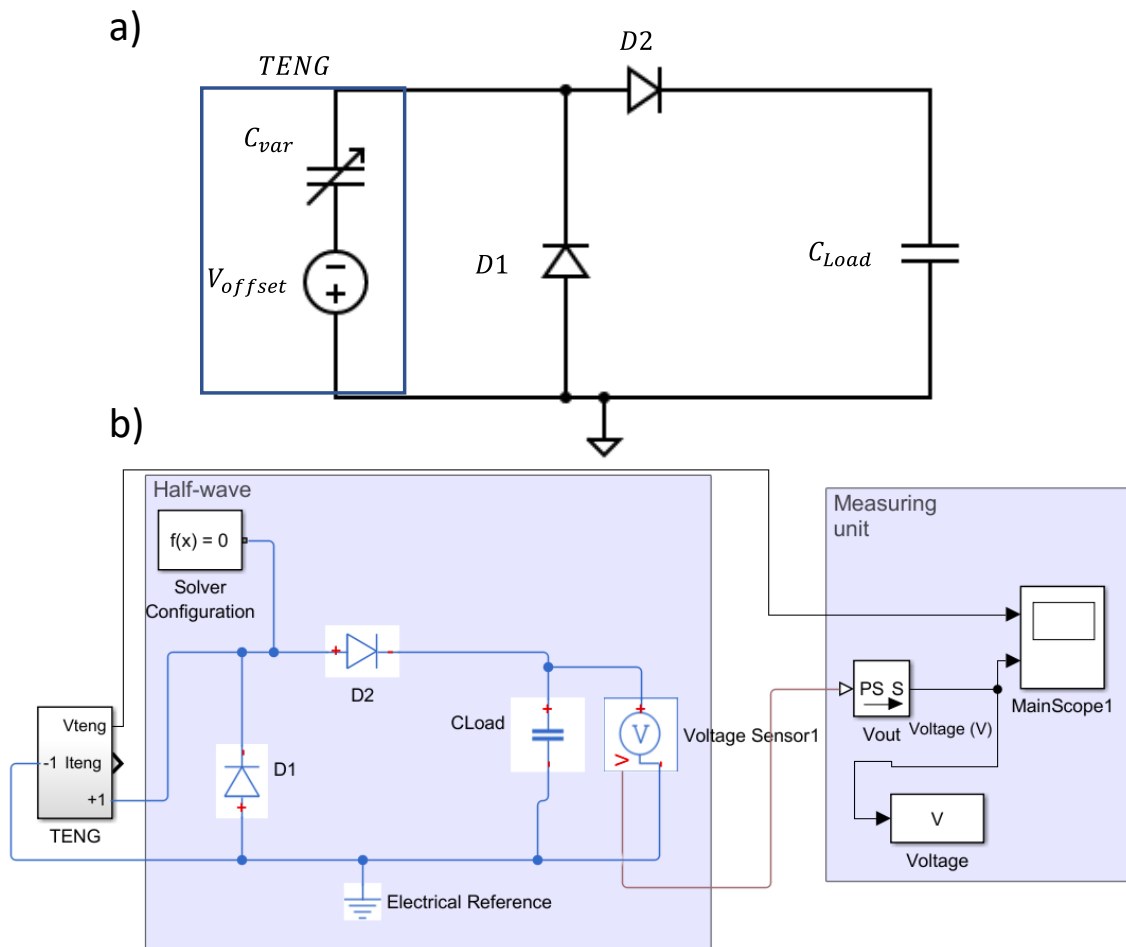
Figure 6.7 *Simulink model for Half-wave conditioning simulation.*

6.3.3 Half-wave conditioning simulation results

The results of the half-wave simulations are shown in this section. The calculated voltage curves are shown on the left plot of Figure 6.8, while the experimental ones are on the plot on the right.
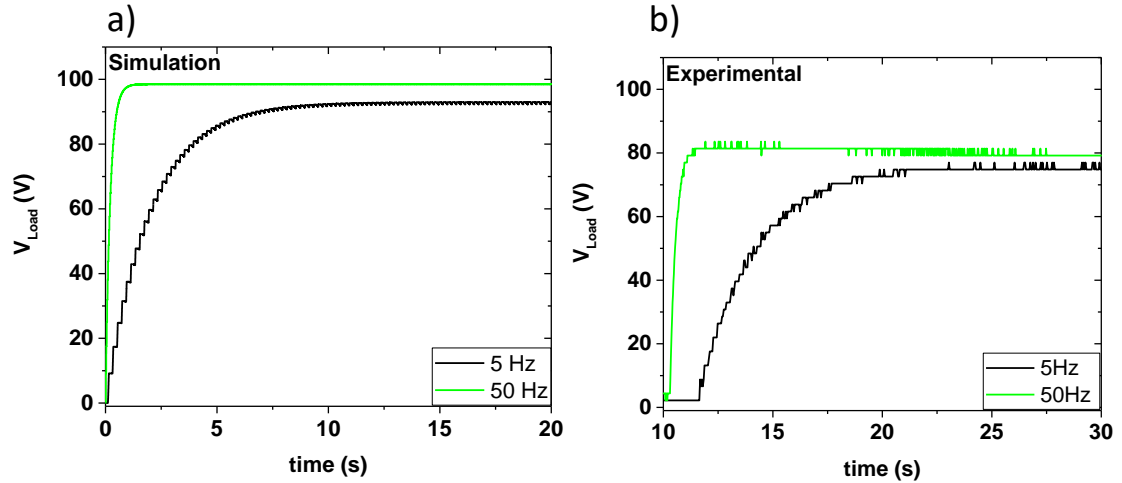
Figure 6.8. *Half-wave voltage curves comparison between simulation results and experimental results at 5 Hz and 50 Hz. a) calculated voltage curves in simulation b) experimental results.*

Figure 6.8 shows how the trends observed in the experimental results are perfectly replicated by the simulations. The only differences are quantitative, being the voltage saturation calculated in simulations higher than in the experimental curves. As it was discussed in the experimental results, variations in voltage saturation values can be considerably high between measurements due to charge surface variation on the PFA, which means these differences between simulation and experimental results are reasonable. Furthermore, the growing rate of both curves is also very similar for both frequencies, being a little bit higher for simulations.

Furthermore, the characteristics parameters of the fitting performed over the simulation curves are shown in Table 6.3. The fitting has been performed using the same RC model (expression 5.2) used with the experimental data. This table shows how the characteristic times and saturation voltages are considerably similar between experimental and simulation results. This good matching is observed at both frequencies. The relative error committed by the simulations in the characteristic constant time is never higher than 20 %. About the saturation voltages, the simulation is committing around a 25 % error. Considering that the reproducibility of the experimental results is low, simulations seem to be meeting the experimental results considerably well.

	Frequency	$\tau(s)$	$V_{sat}(s)$	r^2
Simulation	5 Hz	1.9619 ± 0.0003	92.79 ± 0.04	0.998
	50 Hz	0.20528 ± 0.00002	98.52 ± 0.02	0.9993
Experimental	5 Hz	2.43 ± 0.01	74.8 ± 0.1	0.998
	50 Hz	0.244 ± 0.001	80.2 ± 0.1	0.998
Relative Error	5 Hz	20 %	24 %	
	50 Hz	17%	25 %	

On the other hand, the transmitted power calculated in simulations is shown in Figure 6.9. Again, the qualitative behaviour is the same, but with significant deviations in the absolute values. Simulations results show clear discrepancies in the case of maximum power transmission.

The dependence between the power transmitted and the voltage inside the capacitor is presented in Figure 6.10. The figure shows how experimental results and simulations do find similar values for the optimal voltage operation point. Finally, Table 6.4 quantifies the disparities between experimental and simulated power transmission curves.
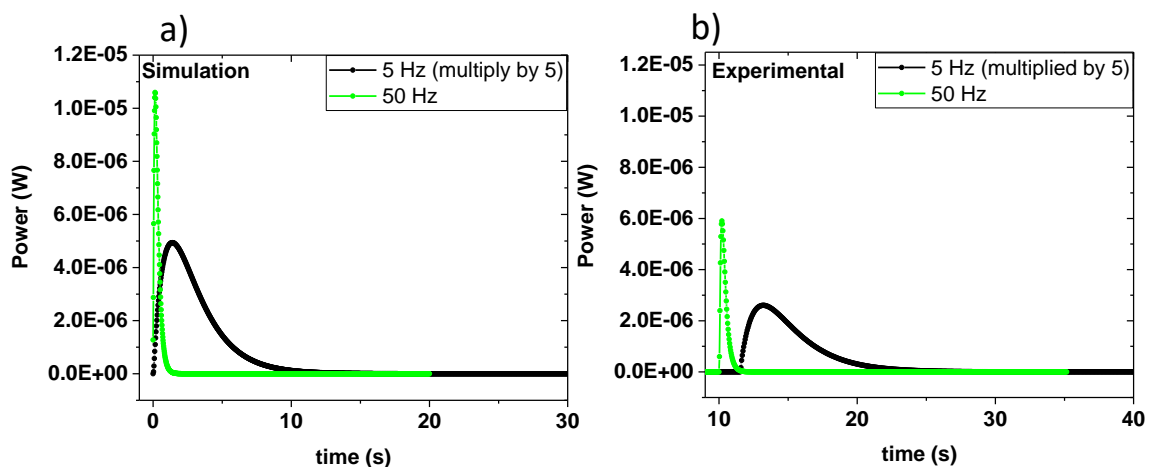
Figure 6.9. *Power transmission vs time calculated in half-wave conditioning simulations at 5 Hz and 50 Hz, in comparison with the experimental results.*
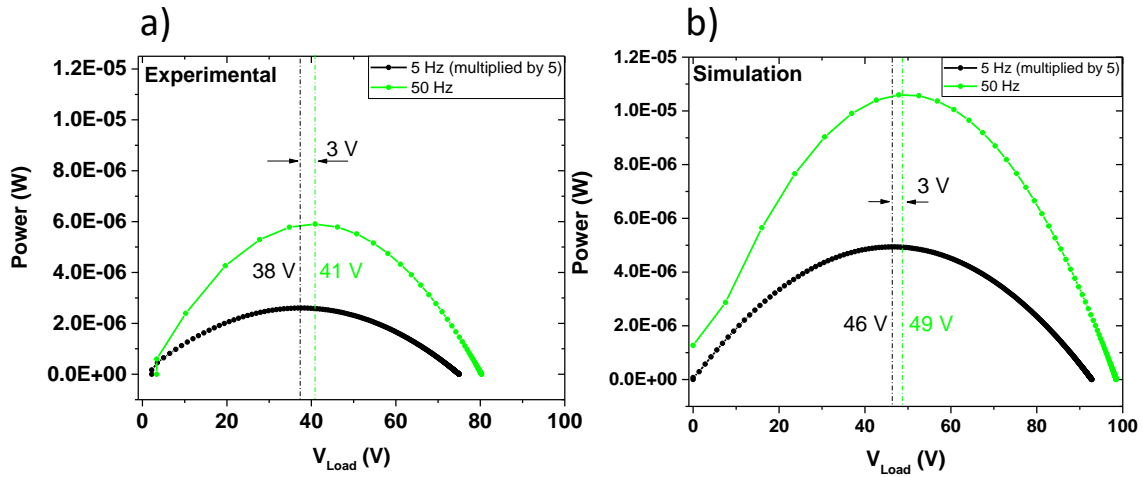
Figure 6.10. Power transmission vs voltage calculated in half-wave conditioning simulations at 5 Hz and 50 Hz, in comparison with the experimental results.

Table 6.4. Quantitative comparison between half-wave conditioning experimental results and simulations. P_{max} is the maximum power transmitted, $V_{optimal}$ is the optimal operating voltage and N_{cycles} is the number of cycles needed to reach the optimal point.

	Frequency	$P_{max}(\mu W)$	$V_{optimal}$ (V)	N_{cycles}
Simulation	5 Hz	0.98	46	7
	50 Hz	10.59	49	7
Experimental	5 Hz	0.52	38	8
	50 Hz	5.90	41	10
Relative Error	5 Hz	88 %	21 %	
	50 Hz	80%	20 %	

In summary, simulations find problems to meet experimental maximum power transmitted. Nevertheless, experimental results and simulations are showing very similar values of the optimal operating voltage. Also, the number of cycles needed to reach the maximum power transmission match as well. Since this number of cycles matches, apparently, that disparities could come from the fact that simulations are overrating the efficiency of a single cycle. This can be

caused by differences between the used value for the V_{offset} parameter and the actual voltage between the PFA layer and the bottom electrode.

In conclusion for this section, half-wave simulations are in general correctly meeting the experimental results. However, the values of transmitted power predicted by the simulations are considerably far from the actual values.

6.3.4 Full-wave conditioning model in simulations

The Simulink model used in the implementation of the full-wave conditioning circuit is analogous to the half-wave model. As it can be seen in Figure 6.11, the circuit is included in the circuit subsystem The measuring unit used is the same as the one used in the case of half-wave.

There is a substantial difference between how both kinds of conditioning circuits have been simulated and it is how the time step has been defined. Full-wave conditioning has presented convergence errors, especially for 50 Hz stimulations. The reason is the high rise rate its voltage curves present. This problem has forced us to work using a fixed time step, which is defined using the *Resolution* parameter, being its usual value at 1 μs. Convergence problems persist if a bigger step is used. As it was done for half-wave conditioning, data were exported to Origin Lab to process simulation results.
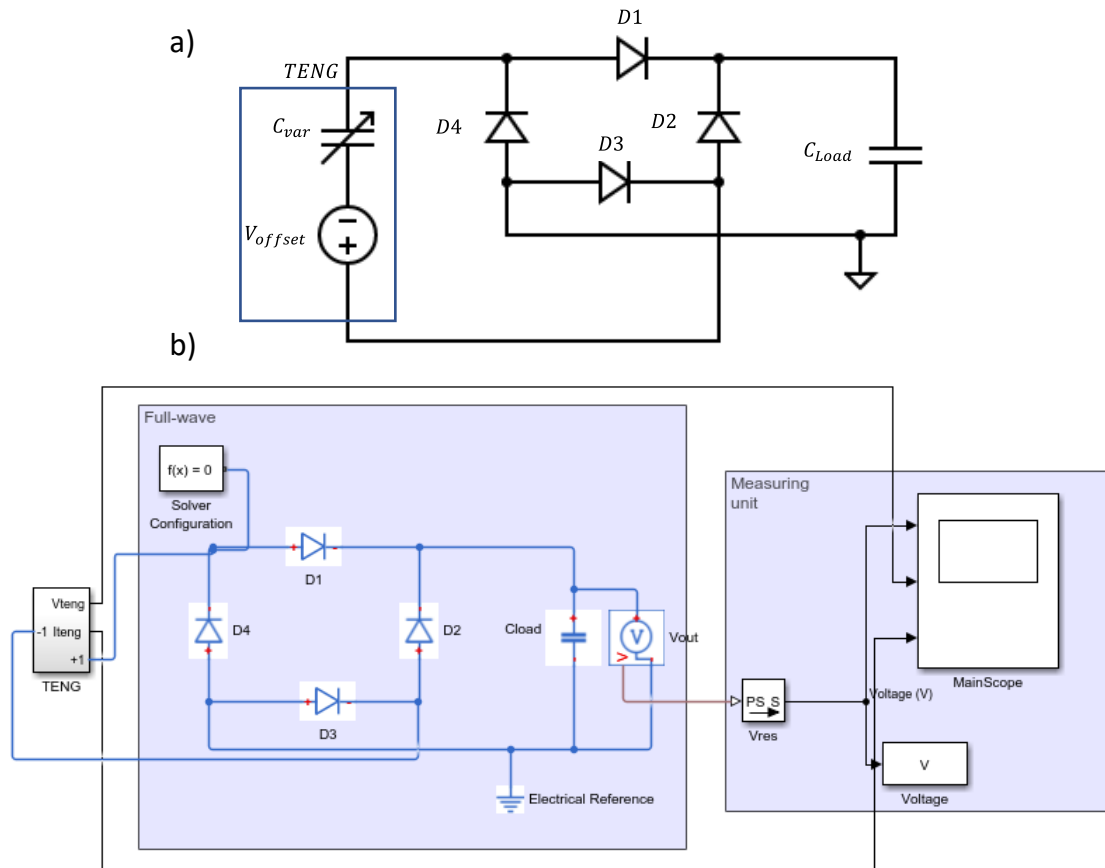
Figure 6.11. *Simulink model for full-wave conditioning simulation. On the top, the diagram circuit is shown, while the simulation model is shown on the bottom.*

6.3.5 Full-wave conditioning simulation results

The voltage curves obtained in simulations are shown in Figure 6.12 with their experimental equivalent. It can be seen that simulation curves describe faster growth rates than experimental results. In fact, this high-rise rate in their voltage curves is very similar for both frequencies in the simulation curves, being overlapped at the beginning. A more detailed comparison between experimental and simulated curves is shown in Table 6.5. As it was said at the half-wave discussion, the fitting has been performed using the RC model of expression (5.2). It can be seen that the fitting quality is considerably low for the simulation curves, due to its fast transition to the saturation value. Regarding the obtained voltage saturation values, the conclusion is that simulations are underrating such values concerning experimental results, but their differences are not significant due to their low relative errors. Therefore, it can be said that simulations give a nice estimation of the real voltage saturation. Furthermore, the characteristic times are underrated in simulations with respect to the experimental results. Simulations predict an unexpected rapid increase in the voltage values. This diversion is stronger in the case of 50 Hz

curves. Since the committed error is twice at 50 Hz than at 5 Hz, dumping seems to be paying an important role.
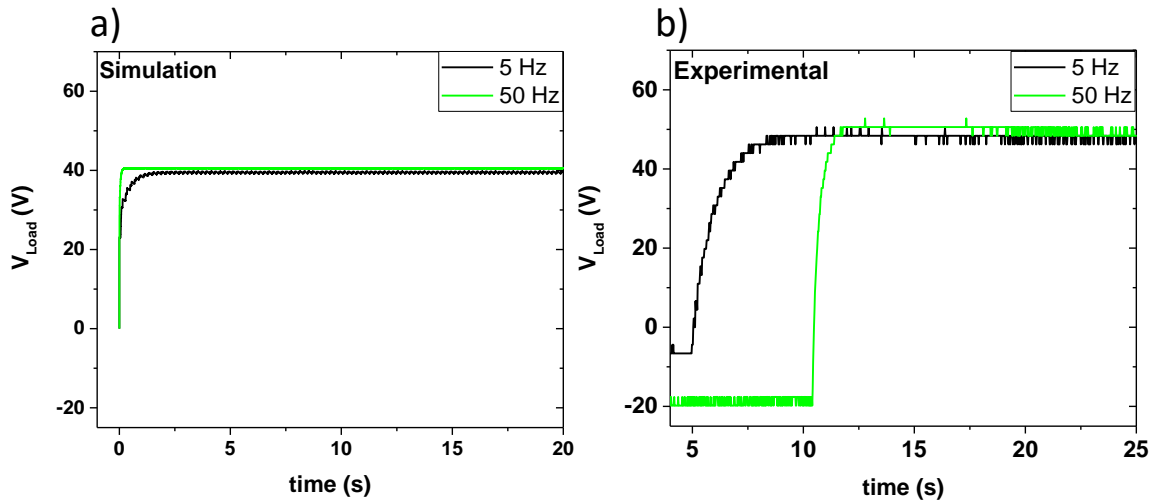
Figure 6.12. *Full-wave voltage curves calculated in simulation and compared with experimental results at 5 Hz and 50 Hz. a) Plots of the simulated results, b) Plots of the experimental results*

Table 6.5 *fitting parameters comparison between simulations and experimental full-wave conditioning voltage curves at 5 Hz and 50 Hz.*

	Frequency	$\tau(s)$	$V_{sat}(s)$	r^2
Simulation	5 Hz	0.377 ± 0.009	44.7 ± 0.1	0.96
	50 Hz	0.037 ± 0.005	47.8 ± 0.1	0.95
Experimental	5 Hz	0.641 ± 0.004	48.1 ± 0.1	0.998
	50 Hz	0.290 ± 0.008	49.7 ± 0.1	0.998
Relative Error	5 Hz	41 %	7 %	
	50 Hz	87 %	4 %	

Figure 6.13 shows the power transmitted figures found in simulation, in comparison with the experimental results. The negative peak shown in experimental results due to noise charge is not presented in simulations since it has not been modelled. There are strong discrepancies between experimental results and simulations. Simulations found too high maximum power

transmitted values, describing a stronger growth rate as well. On the other hand, the results obtained in terms of power transmitted versus the voltage value of the load capacitor are shown in Figure 6.14. Simulations found that the optimal voltage operation point is lower than what the experimental results point out. These discrepancies are not high though, especially comparing with the mismatch between maximum power transmissions between simulations and experimental results. Finally, Table 6.6 shows a complete comparison between simulations and experimental results.
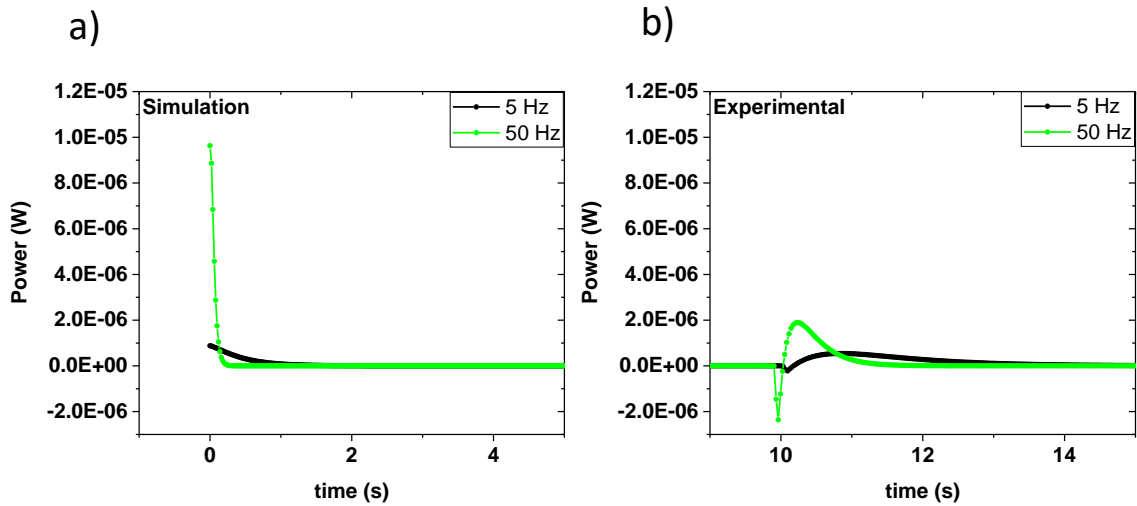
Figure 6.13. *Power transmission vs time calculated in full-wave conditioning simulations at 5 Hz and 50 Hz, in comparison with the experimental results. a) Simulation results, b) experimental results.*
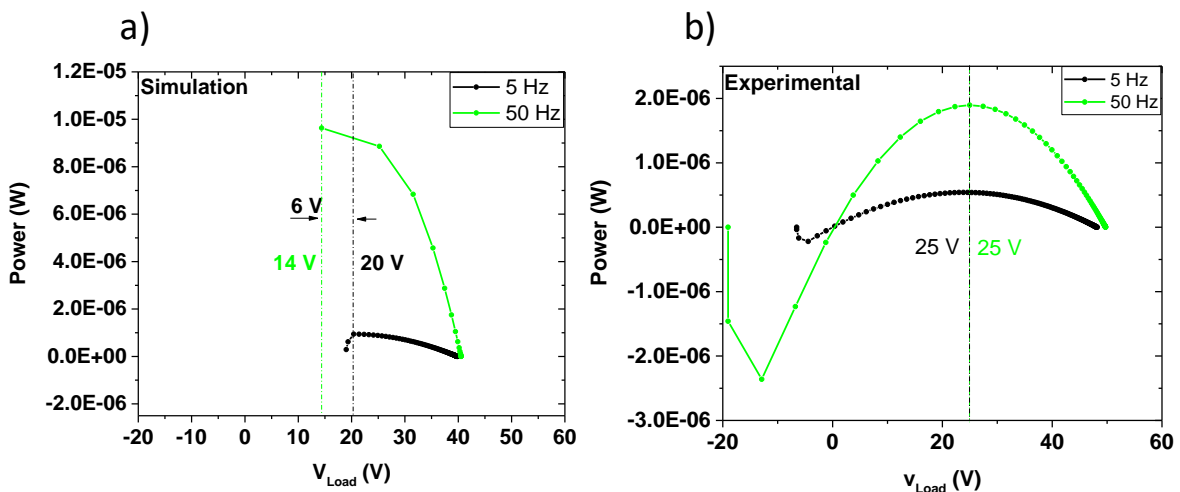
Figure 6.14. *Power transmission vs voltage calculated in full-wave conditioning simulations at 5 Hz and 50 Hz, in comparison with the experimental results. a) Simulation results, b) experimental results.*

Table 6.6. *Quantitative comparison between full-wave conditioning experimental results and simulations. P_{max} is the maximum power transmitted, $V_{optimal}$ is the optimal operating voltage and N_{cycles} is the number of cycles needed to reach the optimal point.*

	Frequency	$P_{max}(\mu W)$	$V_{optimal}$ (V)	N_{cycles}
Simulation	5 Hz	0.88	20.39	1
	50 Hz	9.63	14.38	1
Experimental	5 Hz	0.54	25	3
	50 Hz	1.89	25	7
Relative Error	5 Hz	62 %	18 %	
	50 Hz	400 %	42 %	

Regarding the maximum power transmitted results, simulations are considerably far from the real values. This problem is increased in the 50 Hz case, where the calculated output power is almost 10 times higher than the experimental value. However, this difference is much lower at 5 Hz. This is probably caused by parasitic effects present in the experimental situation, which are not being considered in simulations.

However, simulations are finding considerably good values for the optimal voltage operation point. The error committed in the 50 Hz simulations is considerably higher than in the 5 Hz case, probably due to dumping.

There are also diversions in the number of cycles needed to reach the maximum output power. In simulations, the first cycle is the best in terms of power transmittance, while in the experimental results it is cycle number 3 in the case of 5 Hz and cycle number 7 for 50 Hz. Once again, simulations are overrating the amount of energy pumped by each iteration.

In conclusion for this section, simulations find important difficulties meeting the experimental results, especially at high frequency. The reason could be some rapid increment in voltage values at the first stages of the simulation. This would lead to convergence problems, especially at high frequencies. This entails poor result convergence with the experimental results. Therefore, it would indicate that unmodelled parasitic phenomena are truly influencing half-wave experimental behaviour since it is hard to meet experimental values using an ideal model.

6.3.6 Influence on the diodes reverse current

To illustrate the importance of reverse current in the behaviour of half-wave and full-wave conditioning, Figure 6.15 offers a comparison between half-wave and full-wave voltage curves for different values of diodes reverse conductivities, at a working frequency of 5 Hz. It can be seen how the reverse currents of the diodes have a strong influence on circuits behaviour, especially for the half-wave conditioning case. This is reasonable, since full-wave have two diodes in series in every discharge path, increasing the actual off-resistance. In addition, reverse currents explain why the values predicted for saturation voltages in the theoretical development of Chapter 1 are not reached in simulations and experimental results. The equilibrium is not reached due to an electrostatic equilibrium between the voltage in the TENG and the voltage in the load capacitor, this only happens in the ideal case. In the actual case, voltage saturation is reached when the charge introduced in the load capacitor in a cycle is discharged by the diodes before the next cycle arrives. This fact also explains why saturation voltages, in simulations results, depends on the working frequency.
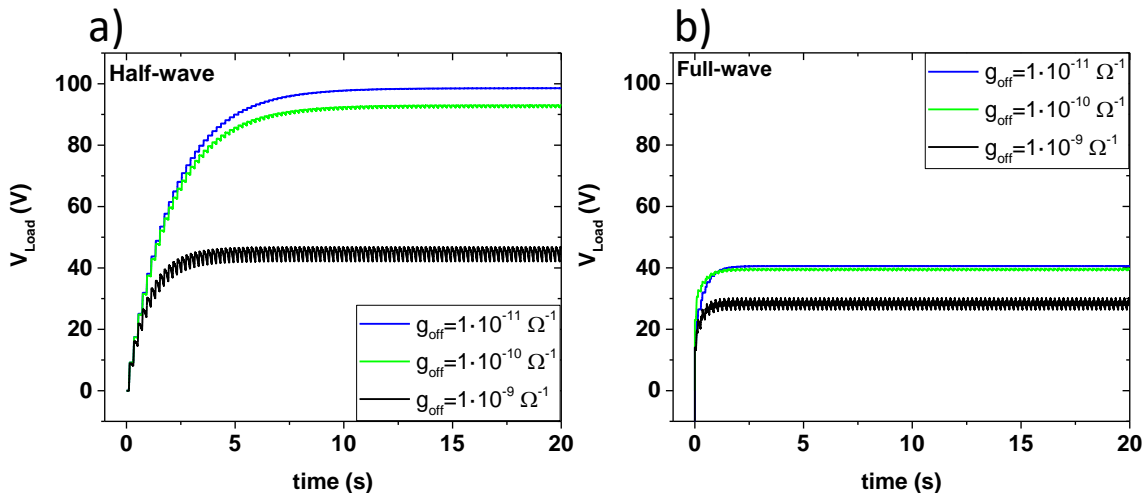
Figure 6.15. *Comparisons between the influence of reverse current on half-wave and full-wave conditioning at 5 Hz. a) Half-wave results, b) full-wave results.*

6.3.7 Performance comparison between half-wave and full-wave conditioning simulations

In conclusion, an evaluation of the performance of the conditioning simulations has been carried out. Table 6.7 shows the relative errors calculated in the characteristic parameters for each kind of circuit. Regarding half-wave conditioning simulations, their results are more accurate than full-wave simulations. Half-wave conditioning simulations show high relative errors in the maximum output power. In the rest of the characteristic parameters, their errors are always below 22 %. This means that the electric model is performing a considerably good job despite its

simplicity. Dumping is not a big issue in this kind of circuit, since 5 Hz and 50 Hz relative errors for half-wave parameters are considerably similar.

In the case of full-wave conditioning, simulations are finding clear problems meeting the experimental characteristic constant times and maximum output powers. Dumping seems to be a crucial factor in full-waves behaviour seems 5 Hz relative errors are considerably smaller than 50 Hz errors. Therefore, high-frequency simulations seem to be considerably far from the experimental behaviour. This points out that full-wave conditioning is more influenced by parasitic effects than half-wave since the used electric model is not providing the same good results in such a circuit.

Table 6.7. *Comparison between calculated relative error between simulations and experimental results for half-wave and full-wave conditioning, at 5 Hz and 50 Hz.*

	Frequency	τ	V_{sat}	P_{max}	$V_{optimal}$
Half-wave	5 Hz	20 %	24 %	88 %	21 %
	50 Hz	17%	25 %	80%	20 %
Full wave	5 Hz	41.18 %	7.06 %	62 %	18 %
	50 Hz	87.24 %	3.82 %	400 %	42 %

7. CONCLUSIONS

The present chapter includes the conclusions and fulfilled objectives of the Master Thesis project, which are listed as follows:

- A **modular characterization platform** to assess the performance of the **triboelectric nanogenerators** has been developed and assembled and verified. This first version makes use of a SMU Keithley instrument (Objective 1).

- An **optimized platform has been developed** by replacing the SMU unit with an inexpensive oscilloscope. (Objective 1).

- The optimized version of the characterization set-up **includes several improvements** and advantages in terms of **cost-efficiency**, **real-time monitoring**, **simultaneous acquisition of force and nanogenerator signal** and **configuration** (Objective 1).

- The oscilloscope-based set-up was adapted to **the characterization of high voltage and high impedance nanogenerators** thanks to an *ad-hoc* signal conditioning unit (voltage divider and impedance decoupling) (Objective 2).

- The optimized oscilloscope-based set-up has been used for the characterization of the output voltage signal, the transmitted power and the optimal load of a homemade nanogenerator. The acquired data and observed trends showed a **good agreement with the behaviour reported in the literature** for other triboelectric nanogenerators (Objective 2).

- A **half-wave conditioning** circuit has been implemented to optimize the power transfer process to power management units (Objective 3).

- A **full-wave conditioning** circuit has been implemented to optimize the power transfer process to power management units (Objective 3).

- A specific **data treatment process** has been conceived and systematized to calculate the main figures of merits (Objective 1).

- The used data treatment process fits V_{load} (t) curves by considering an RC charging model. This model provides a **reliable fitting of the experimental data**. (Objective 1).

- The performance of the conditioning circuits has been experimentally analysed (V(t) and power (t) curves) and the **main figure of merits** (saturation voltage, maximum instantaneous power, and optimal operational voltage) has been calculated for different excitation frequencies (Objective 3).

- A MATLAB-based simulation approach has been implemented **to model the behaviour of TENG devices**. This is based on the TENG lumped model reported in the literature (Objective 4).

- In order to validate the simulation methodology, the evolution of V_{TENG} (t) has been simulated for different excitation frequencies and external loads. The observed evolution on the **V_{TENG} profiles reasonably agrees with the trend experimentally observed and reported in the literature** (Objective 4).

- A **qualitative agreement between simulation and experimental** results is reached in the case of the output power transferred to an external load without conditioning circuits. (Objective 4).

- A MATLAB-based **simulation** approach has also been implemented to theoretically analyse the performance of both **full-wave** and **half-wave conditioning circuits**. (Objective 4).

- For the half-wave circuits, **simulations were able to reproduce the qualitative trends** observed experimentally and **some of the figures of merits showed a good agreement with experimental results** (Objective 4).

- In the case of the full-wave circuits, the used simulations method finds important difficulties to meets the experimental results, especially at high frequency (Objective 4).

8. REFERENCES

[1] A. N. Filippin *et al.*, "Nano Energy 3D core-multishell piezoelectric nanogenerators," *Nano Energy*, vol. 58, no. January, pp. 476–483, 2019, doi: 10.1016/j.nanoen.2019.01.047.

[2] A. Ghaffarinejad and J. Y. Hasani, "Modeling of triboelectric charge accumulation dynamics at the metal – insulator interface for variable capacitive structures : application to triboelectric nanogenerators," *Appl. Phys. A*, vol. 0, no. 0, p. 0, 2019, doi: 10.1007/s00339-019-2495-y.

[3] C. Fang *et al.*, "Overview of Power Management for Triboelectric Nanogenerators," *Adv. Intell. Syst.*, vol. 2, no. 2, p. 1900129, 2020, doi: 10.1002/aisy.201900129.

[4] S. Lu *et al.*, "Regulating the high-voltage and high-impedance characteristics of triboelectric nanogenerator toward practical self-powered sensors," *Nano Energy*, vol. 87, no. May, p. 106137, 2021, doi: 10.1016/j.nanoen.2021.106137.

[5] Z. Wang *et al.*, "Two voltages in contact-separation triboelectric nanogenerator: From asymmetry to symmetry for maximum output," *Nano Energy*, vol. 69, no. January, p. 104452, Mar. 2020, doi: 10.1016/j.nanoen.2020.104452.

[6] A. Ghaffarinejad, J. Yavand, D. Galayko, and P. Basset, "Nano Energy Superior performance of half-wave to full-wave rectifier as a power conditioning circuit for triboelectric nanogenerators : Application to contact-separation and sliding mode TENG," *Nano Energy*, vol. 66, no. September, p. 104137, 2019, doi: 10.1016/j.nanoen.2019.104137.

[7] H. Zhang, D. Galayko, and P. Basset, "A self-sustained energy storage system with an electrostatic automatic switch and a buck converter for triboelectric nanogenerators," *J. Phys. Conf. Ser.*, vol. 1407, no. 1, pp. 8–12, 2019, doi: 10.1088/1742-6596/1407/1/012016.

[8] A. Gha *et al.*, "Nano Energy Full paper A conditioning circuit with exponential enhancement of output energy for triboelectric nanogenerator," vol. 51, no. May, pp. 173–184, 2018, doi: 10.1016/j.nanoen.2018.06.034.

[9] D. A. Barkas, C. S. Psomopoulos, P. Papageorgas, K. Kalkanis, D. Piromalis, and A. Mouratidis, "Sustainable energy harvesting through triboelectric nano – Generators: A review of current status and applications," *Energy Procedia*, vol. 157, pp. 999–1010, 2019, doi: 10.1016/j.egypro.2018.11.267.

[10] A. Kinage, S. Sahoo, and S. Chaudhuri, "Effects of different electrical arrangements and

Thomson effect on the system performance as well as the optimum allocation of thermocouples in a self-driven two-stage TEC & TEG," *Therm. Sci. Eng. Prog.*, vol. 25, no. August, p. 101035, 2021, doi: 10.1016/j.tsep.2021.101035.

[11]   E. O'Riordan, D. Galayko, P. Basset, and E. Blokhina, "Complete electromechanical analysis of electrostatic kinetic energy harvesters biased with a continuous conditioning circuit," *Sensors Actuators, A Phys.*, vol. 247, pp. 379–388, 2016, doi: 10.1016/j.sna.2016.06.018.

[12]   C. Shekhar and S. Varma, "An Optimized 2.4 GHz RF Energy Harvester for Energizing Low-Power Wireless Sensor Platforms," *J. Circuits, Syst. Comput.*, vol. 28, no. 6, Jun. 2019, doi: 10.1142/S0218126619501044.

[13]   Z. Li, G. Zhu, R. Yang, A. C. Wang, and Z. L. Wang, "Muscle-driven in vivo nanogenerator," *Adv. Mater.*, vol. 22, no. 23, pp. 2534–2537, 2010, doi: 10.1002/adma.200904355.

[14]   S. Niu, X. Wang, F. Yi, Y. S. Zhou, and Z. L. Wang, "A universal self-charging system driven by random biomechanical energy for sustainable operation of mobile electronics," *Nat. Commun.*, vol. 6, 2015, doi: 10.1038/ncomms9975.

[15]   S. Ali *et al.*, "Nano Energy Piezo-tribo dual effect hybrid nanogenerators for health monitoring," *Nano Energy*, vol. 82, no. December 2020, p. 105691, 2021, doi: 10.1016/j.nanoen.2020.105691.

[16]   A. Yang *et al.*, "Hybrid piezo/triboelectric nanogenerator for stray magnetic energy harvesting and self-powered sensing applications," *High Volt.*, no. December 2020, pp. 1–8, 2021, doi: 10.1049/hve2.12096.

[17]   Y. Dai, T. Li, B. Liu, M. Song, and H. Chen, "Exploiting dynamic thermal energy harvesting for reusing in smartphone with mobile applications," in *ACM SIGPLAN Notices*, Mar. 2018, vol. 53, no. 2, pp. 243–256, doi: 10.1145/3173162.3173188.

[18]   Z. L. Wang and W. Wu, "Nanotechnology-enabled energy harvesting for self-powered micro-/nanosystems," *Angew. Chemie - Int. Ed.*, vol. 51, no. 47, pp. 11700–11721, 2012, doi: 10.1002/anie.201201656.

[19]   N. P. Klochko *et al.*, "Development of semi-transparent ZnO/FTO solar thermoelectric nanogenerator for energy efficient glazing," *Sol. Energy*, vol. 184, no. April, pp. 230–239, 2019, doi: 10.1016/j.solener.2019.04.002.

[20]   H. Jouhara *et al.*, "Thermoelectric generator (TEG) technologies and applications," *Int. J. Thermofluids*, vol. 9, 2021, doi: 10.1016/j.ijft.2021.100063.

[21]   Q. Li, S. Li, D. Pisignano, L. Persano, Y. Yang, and Y. Su, "On the evaluation of output voltages for quantifying the performance of pyroelectric energy harvesters," *Nano Energy*, vol. 86, no. February, p. 106045, 2021, doi: 10.1016/j.nanoen.2021.106045.

[22]   A. Wazeer, K. S. Srikanth, P. Mathiyalagan, and S. Vidya, "Pyroelectric energy harvesting using automobile exhaust emission," *Mater. Today Proc.*, no. xxxx, pp. 1–5, 2021, doi: 10.1016/j.matpr.2021.01.844.

[23]   G. Sebald, E. Lefeuvre, and D. Guyomar, "Pyroelectric energy conversion: Optimization principles," *IEEE Trans. Ultrason. Ferroelectr. Freq. Control*, vol. 55, no. 3, pp. 538–551, 2008, doi: 10.1109/TUFFC.2008.680.

[24]   G. Charalampidis, A. Papadakis, and M. Samarakou, "Power estimation of RF energy harvesters," *Energy Procedia*, vol. 157, no. 2018, pp. 892–900, 2019, doi: 10.1016/j.egypro.2018.11.255.

[25]   Z. Leonowicz, Institute of Electrical and Electronics Engineers, IEEE Electromagnetic Compatibility Society, IEEE Power & Energy Society, IEEE Industry Applications Society, and IEEE Industrial and Commercial Power Systems Europe 4. 2020 Online, *Conference proceedings 2020 IEEE International Conference on Environment and Electrical Engineering and 2020 IEEE Industrial and Commercial Power Systems Europe (EEEIC/I & CPS Europe) 9-12 June, 2020, Madrid, Spain : the 2020 edition will be held on scheduled days from 09th to 12th June 2020 in web streaming.* .

[26]   S. Chakrabarti *et al.*, *2019 IEEE 10th Annual Ubiquitous Computing, Electronics & Mobile Communication Conference (UEMCON) : 10th-12th October, 2019, Columbia University, New York, USA.* .

[27]   K. Wang *et al.*, "Coupling electrostatic induction and global electron circulation for constant-current triboelectric nanogenerators," *Nano Energy*, vol. 85, no. February, p. 105929, 2021, doi: 10.1016/j.nanoen.2021.105929.

[28]   A. A. Mathew, A. Chandrasekhar, and S. Vivekanandan, "A review on real-time implantable and wearable health monitoring sensors based on triboelectric nanogenerator approach," *Nano Energy*, vol. 80, no. September 2020, p. 105566, 2021, doi: 10.1016/j.nanoen.2020.105566.

[29]   Y. Sun, Y. Zheng, R. Wang, J. Fan, and Y. Liu, "Direct-current piezoelectric nanogenerator based on two-layer zinc oxide nanorod arrays with equal c-axis orientation for energy harvesting," *Chem. Eng. J.*, vol. 426, no. July, p. 131262, 2021, doi: 10.1016/j.cej.2021.131262.

[30]   P. Jiao, "Emerging artificial intelligence in piezoelectric and triboelectric

nanogenerators," *Nano Energy*, vol. 88, p. 106227, 2021, doi: 10.1016/j.nanoen.2021.106227.

[31]   R. S. Dahiya and M. Valle, *Robotic tactile sensing: Technologies and system*, vol. 9789400705. 2014.

[32]   R. Yang, Y. Qin, C. Li, G. Zhu, and Z. L. Wang, "Converting Biomechanical Energy into Electricity by a Muscle-Movement-Driven Nanogenerator Rusen," 2009.

[33]   S. M. A. Z. Shawon *et al.*, "Piezo-Tribo Dual Effect Hybrid Nanogenerators for Health Monitoring," *Nano Energy*, vol. 82, no. December 2020, p. 105691, 2020, doi: 10.1016/j.nanoen.2020.105691.

[34]   P. Maharjan *et al.*, "Nano Energy High-performance keyboard typing motion driven hybrid nanogenerator," *Nano Energy*, vol. 88, no. June, p. 106232, 2021, doi: 10.1016/j.nanoen.2021.106232.

[35]   H. Zou *et al.*, "Quantifying the triboelectric series," *Nat. Commun.*, vol. 10, no. 1, pp. 1–9, 2019, doi: 10.1038/s41467-019-09461-x.

[36]   R. Zhang and H. Olin, "Material choices for triboelectric nanogenerators: A critical review," *EcoMat*, vol. 2, no. 4, pp. 1–13, 2020, doi: 10.1002/eom2.12062.

[37]   D. Godwinraj and S. C. George, "Recent advancement in TENG polymer structures and energy efficient charge control circuits," *Adv. Ind. Eng. Polym. Res.*, vol. 4, no. 1, pp. 1–8, 2021, doi: 10.1016/j.aiepr.2020.12.003.

[38]   S. Korkmaz and A. Kariper, "Production and applications of flexible/wearable triboelectric nanogenerator (TENGS)," *Synth. Met.*, vol. 273, no. November 2020, 2021, doi: 10.1016/j.synthmet.2020.116692.

[39]   R. Kumar, L. Chau, and K. Kwan, "Nano Energy Double characteristic BNO-SPI-TENGs for robust contact electri fi cation by vertical contact separation mode through ion and electron charge transfer," *Nano Energy*, vol. 44, no. November 2017, pp. 430–437, 2018, doi: 10.1016/j.nanoen.2017.12.019.

[40]   Y. Chu *et al.*, "Theoretical Study on the Output of Contact-Separation Triboelectric Nanogenerators with Arbitrary Charging and Grounding Conditions," *Nano Energy*, vol. 89, no. PA, p. 106383, 2021, doi: 10.1016/j.nanoen.2021.106383.

[41]   J. Jiang *et al.*, "Nano Energy Full paper A self-powered hydrogen leakage sensor based on impedance adjustable windmill-like triboelectric nanogenerator," *Nano Energy*, vol. 89, no. PB, p. 106453, 2021, doi: 10.1016/j.nanoen.2021.106453.

[42]   W. Sun *et al.*, "TENG-Bot: Triboelectric nanogenerator powered soft robot made of uni-

directional dielectric elastomer," *Nano Energy*, vol. 85, no. January, 2021, doi: 10.1016/j.nanoen.2021.106012.

[43]   W. Zhang *et al.*, "A general charge compensation strategy for calibrating the voltage of a triboelectric nanogenerator measured by a capacitive circuit," *Nano Energy*, vol. 86, no. February, p. 106056, 2021, doi: 10.1016/j.nanoen.2021.106056.

[44]   J. H. Lee, Y. S. Park, S. Cho, I. S. Kang, J. K. Kim, and U. Jeong, "Output voltage modulation in triboelectric nanogenerator by printed ion gel capacitors," *Nano Energy*, vol. 54, no. August, pp. 367–374, 2018, doi: 10.1016/j.nanoen.2018.10.016.

[45]   J. Shao, M. Willatzen, and Z. L. Wang, "Theoretical modeling of triboelectric nanogenerators (TENGs)," *J. Appl. Phys.*, vol. 128, no. 11, 2020, doi: 10.1063/5.0020961.

[46]   Y. Hu *et al.*, "An adaptable interface conditioning circuit based on Triboelectric Nanogenerators for self-powered sensors," *Micromachines*, vol. 9, no. 3, Mar. 2018, doi: 10.3390/mi9030105.

[47]   S. Niu, X. Wang, F. Yi, Y. S. Zhou, and Z. L. Wang, "A universal self-charging system driven by random biomechanical energy for sustainable operation of mobile electronics," *Nat. Commun.*, vol. 6, pp. 1–8, 2015, doi: 10.1038/ncomms9975.

[48]   D. Galayko *et al.*, "Capacitive Energy Conversion With Circuits Implementing a Rectangular Charge-Voltage Cycle-Part 1 : Analysis of the Electrical Domain To cite this version :," 2015.

[49]   P. Basset, E. Blokhina, and D. Galayko, *Electrostatic Kinetic Energy Harvester*, 2016th ed. London: Wiley.

[50]   K. Xia, D. Wu, J. Fu, and Z. Xu, "A pulse controllable voltage source based on triboelectric nanogenerator," *Nano Energy*, vol. 77, no. January, 2020, doi: 10.1016/j.nanoen.2020.105112.

[51]   S. Phillips Thompson, *Dynamo-Electric Machinery*, Second edi. London, 1886.

[52]   S. Zargari, Z. Daie Koozehkanani, H. Veladi, J. Sobhi, and A. Rezania, "A new Mylar-based triboelectric energy harvester with an innovative design for mechanical energy harvesting applications," *Energy Convers. Manag.*, vol. 244, p. 114489, 2021, doi: 10.1016/j.enconman.2021.114489.

[53]   F. Michel and M. Steyaert, "Comparison of high impedance input topologies with low EMI susceptibility," *Analog Integr. Circuits Signal Process.*, vol. 65, no. 2, pp. 299–309, Nov. 2010, doi: 10.1007/s10470-010-9474-8.

[54]   E. S. Kappenman and S. J. Luck, "The effects of electrode impedance on data quality and

statistical significance in ERP recordings," vol. 47, pp. 888–904, 2010, doi: 10.1111/j.1469-8986.2010.01009.x.

[55] S. Wang, L. Lin, and Z. Lin, "Triboelectric nanogenerators as self-powered active sensors," *Nano Energy*, vol. 11, pp. 436–462, 2015, doi: 10.1016/j.nanoen.2014.10.034.